DENSITY FUNCTIONAL THEORY INVESTIGATION OF NOBLE METAL REDUCTION AGENTS ON γ-AL_2O_3 IN NO_X STORAGE/REDUCTION CATALYSTS

A THESIS SUBMITTED TO
THE GRADUATE SCHOOL OF NATURAL AND APPLIED SCIENCES
OF
MIDDLE EAST TECHNICAL UNIVERSITY

BY

ZÜLEYHA ARTUÇ

IN PARTIAL FULFILLMENT OF THE REQUIREMENTS
FOR
THE DEGREE OF MASTER OF SCIENCE
IN
MICRO AND NANO TECHNOLOGY

AUGUST 2011

Approval of the thesis:

DENSITY FUNCTIONAL THEORY INVESTIGATION OF NOBLE METAL REDUCTION AGENTS ON γ-AL_2O_3 IN NO_X STORAGE/REDUCTION CATALYSTS

submitted by **ZÜLEYHA ARTUÇ** in partial fulfillment of the requirements for the degree of **Master of Science in Micro and Nano Technology Department, Middle East Technical University** by,

Prof. Dr. Canan Özgen
Dean, Graduate School of **Natural and Applied Sciences** _____

Prof. Dr. Mürvet Volkan
Head of Department, **Micro and Nano Technology** _____

Assist. Prof. Dr. Daniele Toffoli
Supervisor, **Chemistry, METU** _____

Assist. Prof. Dr. Hande Toffoli
Co-supervisor, **Physics, METU** _____

Examining Committee Members:

Prof. Dr. Ceyhan Kayran
Chemistry, METU _____

Assist. Prof. Dr. Daniele Toffoli
Chemistry, METU _____

Assoc. Prof. Dr. Ayşen Yılmaz
Chemistry, METU _____

Assist. Prof. Dr. İrem Erel
Chemistry, METU _____

Assist. Prof. Dr. Emrah Özensoy
Chemistry, Bilkent _____

Date: _____

I hereby declare that all information in this document has been obtained and presented in accordance with academic rules and ethical conduct. I also declare that, as required by these rules and conduct, I have fully cited and referenced all material and results that are not original to this work.

Name, Last Name: ZÜLEYHA ARTUÇ

Signature :

ABSTRACT

DENSITY FUNCTIONAL THEORY INVESTIGATION OF NOBLE METAL REDUCTION AGENTS ON γ-AL_2O_3 IN NO_X STORAGE/REDUCTION CATALYSTS

Artuç, Züleyha

M.Sc., Department of Micro and Nano Technology

Supervisor : Assist. Prof. Dr. Daniele Toffoli

Co-Supervisor : Assist. Prof. Dr. Hande Toffoli

August 2011, 121 pages

Pollution from automobile exhaust is one of the most major environmental problems because of increasing usage of engine technologies. Diesel and lean burn gasoline engines operate under oxygen rich (lean) conditions and they emit harmfull gases to the atmosphere (CO, CO_2, NO, NO_2). The control of NO_x emission from exhaust has become a challenging issue in engine industry because of the worldwide environmental regulations. Therefore lean-burn NO_x emission control technologies have been developed to reduce emission of harmfull gases from exhausts, and the NO_x storage/reduction (NSR) catalysts is one of the most promising candidates to reduce the pollution caused by lean-burn engines. In NSR systems, NO from the emission is first oxidized to NO_2 over noble metal sites (Pt, Rh, Pd) during lean-burn engine operation. After that NO_2 is stored as nitrites and nitrates in alkali earth oxides (BaO, MgO, CaO) particles or monolayer which is well dispersed on a substrate (γ-Al_2O_3, TiO2, SiO2). Finally, stored NO_x compound are broken into N_2 and O_2 on noble metal sites. The Pt/BaO/γ-Al_2O_3 system is one of the most popular subjects in literature both experimentally and theoretically since this system is known to be catalytically more active and effcient in NO_x reduction/storage process. However, although the early results provided some insight regarding the NOx formation on Pt/BaO/γ-Al_2O_3 system, certain aspects of NO_x uptake and

interactions between NO_x and Pt-BaO components are still not clearly explained. For this reason, in this thesis, the interaction between catalytic redox components, Pt and Rh, and the support material γ-Al_2O_3 and the effects of Pt and Rh in atomic and diatomic clusters forms on the adsorption of the NO_2 molecule on the γ-Al_2O_3(100) surface have been investigated by using density functional theory (DFT).

Keywords: Density Functional Theory (DFT), NO_x Storage/Reduction (NSR), Catalysts, γ-Al_2O_3, Noble metals

ÖZ

NO_X İNDİRGEME/DEPOLAMA KATALİZÖRLERİNDE ASAL METALLERİN İNDİRGEME AJANI OLARAK γ-AL_2O_3 ÜZERİNDE YÜK YOĞUNLUĞU TEORİSİ İLE İNCELENMESİ

Artuç, Züleyha

Yüksek Lisans, Mikro ve Nano Teknoloji Bölümü

Tez Yöneticisi : Yrd. Doç. Dr. Daniele Toffoli

Ortak Tez Yöneticisi : Yrd. Doç. Dr. Hande Toffoli

Ağustos 2011, 121 sayfa

Motor teknolojilerinin kullanımındaki artışla beraber, motorlu araçların egzozlarından kaynaklanan kirlilik günümüzde çevre kirliliğinin problemlerinden biri haline gelmiştir. İçten yanmalı dizel ve benzinli motorlar oksijen kullanarak çalışırken, atmosfere zararlı gazlar salmaktadır (CO, CO_2, NO, NO_2). Dünya çapındaki çevre kirliliğine dair düzenlemelerden dolayı, egzozlardan salınan NO_x gazlarının kontrolü motor endüstrisinde çözülmesi gereken bir sorun haline gelmiştir. Buna bağlı olarak içten yanmalı motorların egzozlarından salınan zararlı gazların azaltılması için NO_x salınımını kontrol eden teknolojiler geliştirilmiş ve NO_x indirgeme/depolama katalizörleri (NSR) en umut vadeden kontrol sistemlerinden biri olmuştur. NSR sisteminde, içten yanmalı motorların çalışma esnasında, ilk olarak NO soy metal kümelerinde (Pt,Rh,Pd) oksitlendirilerek NO_2 ye çevrilmektedir. Ardından, NO_2 partikül kümelenmesi şeklinde ya da tek katmanlı tabaka olarak, destek malzemesinin (γ-Al_2O_3, TiO_2, SiO_2) üzerine yayılmış olan alkali oksitlerde (BaO, MgO, CaO) nitrit ve nitrat olarak depolanmaktadır. Son olarak, depolanmış NO_x bileşenleri, asal metallerin üzerinde indirgenerek N_2 ve O_2 ayrıştırılmaktadır. Pt/BaO/γ-Al_2O_3 sistemi, NO_x indirgeme/depolama işleminde katalitik olarak daha aktif ve etkili olduğu bilindiği için, literatürde hem teorik hem de deneysel

olarak en popüler konularından birisi haline gelmiştir. Her ne kadar çalışmaların ilk sonuçları, Pt/BaO/γ-Al_2O_3 sistemindeki NO_x oluşumunu kavramayı sağlamış olsa da, NO_x alınımı ve NO_x ile Pt-BaO bileşenleri arasındaki etkileşim hala tam olarak açıklanamamıştır. Bu nedenden dolayı, bu tezde, katalitik indirgeme öğeleri olarak Platin (Pt) ve Rodyum (Rh) ile destek malzemesi γ-Al_2O_3 arasındaki etkileşim ve Pt ve Rh hem tek atom hem ikili atom halinde NO_2 molekülünün γ-Al_2O_3(100) yüzeyine tutunması üzerindeki etkileri yoğunluk fonksiyoneli teorisi (YFT) kullanılarak incelenmiştir.

Anahtar Kelimeler: Yoğunluk Fonksiyoneli Teorisi, NO_x Depolama/İndirgeme, Katalizör, Gama-Alüminyumoksit, asal metal

To my father

ACKNOWLEDGMENTS

I would like to express my thanks to my supervisor Daniele Toffoli for his guidance, encouragement and support during the my master's period. I also would like to express my thanks and gratitude to my co-supervisor Hande Toffoli for her advices, moral support, patience and willing to help me all the time thoughout my master's period. Without their guidance and support I would not have been able to complete this thesis.

I am also grateful to my family, especially my brother, for their endless moral support and patience during my master's period.

I would like to express my gratitude to my dear friends Ertürk, Ezgi, Mustafa, Eda, Ayça, Erhan, Tunahan, Yakup, and my collegues Türkan, Ruslan and Rukan for their help, support and valuable friendships. Especially, I would like to express my gratitude to my dear friend Seckin to help me during my undergraduate and master's period, without his help I would not have been able to complete my studies.

This work is financially supported by TÜBİTAK (The Science and Technological Research Council of Turkey). (Grant no:108T706).

TABLE OF CONTENTS

LIST OF TABLES

TABLES

LIST OF FIGURES

FIGURES

CHAPTER 1

INTRODUCTION

Emissions produced by the internal combustion engines cause serious health and enviromental damages such as acid rain, smog, carbon monoxide (CO), carbon dioxide (CO_2), partially burn or unburt hydrocarbons (HCs) and NO_x. Due to the environmental problems associated with the internal combustion engines, the reduction of the harmfull emission compounds has been studied impressively for over fifty years. Developing technology in years has provided better conditions for the internal combustion engines. Improvements of the diesel and lean-burn engine technologies offer a better fuel efficiency and lower emission than the traditional gasoline engines since they operate with 20-30 % higher air to fuel stoichiometric ratios[1]. Therefore lean burn and diesel engines have become a part of daily life, however, harmfull pollutants emission is still an environmental problem due to complexity of the reduction of the NO_x. Vehicle emissions control is one of the important issues of the goverments and they have enforced applications to reduce the emitted pollutants. Especially, the NO_x emission from the diesel engines has been regulated by the goverments, via EURO IV and EURO V standards [2] since diesel engines are the predominant emission sources rather than gasoline or lean-burn vehicles.

The major part of the challenge to reduce harmfull pollutants emitted by diesel and lean-burn engines is the reduction of NO_x emission because other pollutants (CO and HCs) can be oxidized easily by the three-way catalysts (TWC) and selective catalytic reduction (SCR). The TWC can not reduce NO_x to N_2 effectively because of the high oxygen concentration during the oxygen excess [3] and they can not selectively reduce NO_x with the other reductants such as CO, H_2 or unburned hydrocarbons in the presence of the oxygen [4]. This is expected because TWC are designed to operate with no or little oxygen presence in the exhaust [5]. The

SCR catalysts are based on the reduction of NO_x to N_2 using ammonia (NH_3) which is generated from the urea solution [6] and NH_3 is known due to its good selectivity to reduce NO and NO_2 [7]. The SCR catalysts operate well, however, they have remarkable disadvantages. The cost of the SCR process is high and it is limited to the stationary emission sources because the size of the installation is large. In addition, secondary pollutants (such as ammonia, cyanates or organic isocyanates) which cause a decrease in the efficiency of the catalyst are formed during the SCR process [8].

Since the TWC and the SCR do not provide effective NO_x reduction, researchers developed another catalyst system named NO_x storage-reduction catalyst (NSR). The NSR systems are more succesfull to reduce NO_x to N_2 than the TWC and SCR systems. The NSR catalysts can store nitrogen oxides under lean conditions and then nitrogen oxides are released and reduced under fuel rich conditions. The NSR catalysts consist of an alkaline earth oxide (AEO) part for NO_x storage, a precious metal as the catalytic redox component and a support material which has higher surface area.

This thesis is divided into five chapters. In the second chapter, the theoretical background of studied systems are explained. In the third chapter, NSR catalyst are explained in details. In the fourth chapter, the bulk γ-Al_2O_3 and the γ-$Al_2O_3(100)$ surface studies, and performed calculations of the adsorptions of a single noble metal, diatomic clusters and the NO_2 molecule on the γ-$Al_2O_3(100)$ surface and results of the calculations are presented. In the last chapter, a brief summary of the thesis is given.

CHAPTER 2

DENSITY FUNCTIONAL THEORY

Density Functional Theory (DFT) is one of the most successful approaches of quantum chemistry and physics to describe the ground state properties of many-body systems; in particular atoms, molecules, and condensed phases. DFT takes as the basic variable the electronic density instead of the electronic wavefunction. DFT describes the energy as a functional of the electron density therefore it reduces the number of variables in many-body problems. In this way, the ground state energy of the system can be calculated with suitable accuracy and lower computational expense.

2.1 Many-Body Hamiltonian

To calculate the electronic structures of atoms, molecules or bulk materials and investigate the properties of these systems, the electronic wavefunctions must be found. The wavefunction of a single-particle system under an external potential can be calculated by solving the single-particle Schrödinger equation

$$\hat{H}\psi(\vec{r}) = E\psi(\vec{r}) \tag{2.1}$$

Here ψ is the single-particle wavefunction and $\hat{H}$ is the single-particle Hamiltonian with the kinetic energy and a single-particle potential $V(\vec{r})$:

$$\hat{H} = -\frac{\hbar^2}{2m}\nabla^2 + V(\vec{r}) \tag{2.2}$$

When considering many-body systems, the Hamiltonian of Eq.2.2 is replaced with the many-body Hamiltonian which includes nuclei-nuclei, nuclei-electron and electron-electron interactions.

$$\hat{H} = \hat{T}_e + \hat{T}_n + \hat{V}_{nn} + \hat{V}_{ne} + \hat{V}_{ee} \tag{2.3}$$

Here, $\hat{T}_e$ and $\hat{T}_n$ are the kinetic energies of electrons and nuclei respectively, $\hat{V}_{nn}$ is the nuclei-nuclei interaction, $\hat{V}_{ne}$ is the electron-nuclei interaction and the last term $\hat{V}_{ee}$ is the Coulombic potential of the electron-electron interaction.

Since nuclei are considerably heavier than electrons, their contribution to the kinetic energy term can be neglected. This approach is known as the Born-Oppenheimer Approximation [10] and assumes that electrons adjust to changes in nuclear positions instantaneously. Thus, the kinetic energy term of the nuclei can be eliminated from the many-body Hamiltonian. In addition, the Coulombic potential due to nuclei-nuclei interaction has a constant value because the nuclear positions are taken to be fixed in the system.

The many-body system Hamiltonian can be written in SI units as

$$\hat{H} = -\frac{\hbar^2}{2m_e}\sum_{i=1}^{N}\nabla_i^2 - \frac{e^2}{4\pi\epsilon_0}\sum_{I=1}^{N_n}\sum_{i=1}^{N_e}\frac{Z_I}{|\vec{r_i} - \vec{R_I}|} + \frac{1}{2}\frac{e^2}{4\pi\epsilon_0}\sum_{i}^{N_e}\sum_{j\neq i}^{N_e}\frac{1}{|\vec{r_i} - \vec{r_j}|} + \frac{1}{2}\frac{e^2}{4\pi\epsilon_0}\sum_{I}^{N_n}\sum_{J\neq I}^{N_n}\frac{Z_I Z_J}{|\vec{R_I} - \vec{R_J}|} \tag{2.4}$$

where (I=1,2,...N_n) are a set of N_n nuclear coordinates, (i=1,2,...,N_e) are a set of N_e electronic coordinates and Z_I and Z_J are the charges of the nuclei. In atomic units $\hbar$, m_e, e and $\frac{1}{4\pi\epsilon_0}$ are equal to 1, so that the unit of energy is the Hartree and the unit of length is the Bohr. The factor $\frac{1}{2}$ in the electron-electron and the nuclei-nuclei interaction terms is included to prevent double counting of the terms. The many-body Hamiltonian is written in atomic units as

$$\hat{H} = -\frac{1}{2}\sum_{i=1}^{N}\nabla_i^2 - \sum_{I=1}^{N_n}\sum_{i=1}^{N_e}\frac{Z_I}{|\vec{r_i}-\vec{R_I}|} + \frac{1}{2}\sum_{i}^{N_e}\sum_{j\neq i}^{N_e}\frac{1}{|\vec{r_i}-\vec{r_j}|} + \frac{1}{2}\sum_{I}^{N_n}\sum_{J\neq I}^{N_n}\frac{Z_I Z_J}{|\vec{R_I}-\vec{R_J}|} \quad (2.5)$$

The many-body wave function is a complicated function since the system has N_e electrons, which bring $3N_e$ degrees of freedom to the system. Hence, it is not possible to solve the many-body Schrödinger equation for a large system. Approximate methods of solution can be classified into two clases: wavefunction based methods such as Hartree-Fock [10] and density based methods such as the Thomas- Fermi approximation [11]. Density Functional Theory is one of the density based approaches. It proposes that the wavefunction dependence is eliminated by writing all energy terms as functionals of the electron density.

2.2 Electronic Density and Total Energy in terms of Density

2.2.1 Electronic Density

The electronic density $n(\vec{r})$ is one of the basic observable quantities and it can be calculated by employing the single-particle density operator $\hat{n}(\vec{r})$ written as

$$\hat{n}(\vec{r}) = \sum_{i}^{N}\delta(\vec{r}-\vec{r_i}) \quad (2.6)$$

The expectation value of the density operator for the many-body system gives the density of the system

$$n(\vec{r}) = \langle\psi|\hat{n}(\vec{r})|\psi\rangle = \sum_{i=1}^{N}\int\delta(\vec{r}-\vec{r_i})|\psi(\vec{r_1},\ldots,\vec{r_N})|^2 d\vec{r}_1 ... d\vec{r}_N \quad (2.7)$$

Expanding the sum and using the property of the Dirac delta function

$$n(\vec{r}) = \int|\psi(\vec{r},\vec{r}_2\ldots,\vec{r}_N)|^2 d\vec{r}_2 d\vec{r}_3 ... d\vec{r}_N + \int|\psi(\vec{r}_1,\vec{r}\ldots,\vec{r}_N)|^2 d\vec{r}_1 d\vec{r}_3 ... d\vec{r}_N + \ldots \quad (2.8)$$

In this equation, each integral has the same value and the density can therefore be written as

$$n(\vec{r}) = N \int |\psi(\vec{r}, \vec{r}_2 \ldots, \vec{r}_N)|^2 d\vec{r}_2 d\vec{r}_3 ... d\vec{r}_{Ne} \tag{2.9}$$

Since ψ is normalized

$$\int d\vec{r} n(\vec{r}) = N_e \tag{2.10}$$

2.2.2 Total Energy in terms of Density

In quantum mechanics, the observable of any system that corresponds to a given operator can be determined by calculating the expectation value of the operator. Therefore, to calculate the energy of the system, the expectation value of the electronic Hamiltonian should be calculated. Given the electronic Hamiltonian of the many-body system

$$\hat{H}_e = \hat{T}_e + \hat{V}_{en} + \hat{V}_{ee} \tag{2.11}$$

$$\hat{H}_e = -\frac{1}{2} \sum_{i=1}^{N} \nabla_i^2 - \sum_{i=1}^{N_e} \sum_{I=1}^{N_n} \frac{Z_I}{|\vec{r_i} - \vec{R_I}|} + \frac{1}{2} \sum_{i}^{N_e} \sum_{j \neq i}^{N_e} \frac{1}{|\vec{r_i} - \vec{r_j}|} \tag{2.12}$$

the expectation value of electronic Hamiltonian operator reads

$$\langle \psi(\vec{r}_1, \vec{r}_2 \ldots, \vec{r}_N) | \hat{H}_e | \psi(\vec{r}_1, \vec{r}_2 \ldots, \vec{r}_N) \rangle = \\ \langle \psi(\vec{r}_1, \vec{r}_2 \ldots, \vec{r}_N) | \hat{T}_e + \hat{V}_{en} + \hat{V}_{ee} | \psi(\vec{r}_1, \vec{r}_2 \ldots, \vec{r}_N) \rangle \tag{2.13}$$

The expectation value of each operator can be calculated to find the corresponding energies. In the following we will consider each term separately.

2.2.2.1 Kinetic Energy

The kinetic energy operator of a many-body particle system

$$\hat{T}_e = -\frac{1}{2} \sum_{i=1}^{N} \nabla_i^2 \tag{2.14}$$

which yields the expectation value

$$T = \langle \psi(\vec{r}_1, \vec{r}_2 \ldots, \vec{r}_N) | \hat{T}_e | \psi(\vec{r}_1, \vec{r}_2 \ldots, \vec{r}_N) \rangle = \\ -\frac{1}{2} \int d\vec{r} \psi^*(\vec{r}_1, \vec{r}_2 \ldots, \vec{r}_N) \nabla^2 \psi(\vec{r}_1, \vec{r}_2 \ldots, \vec{r}_N) \quad (2.15)$$

The kinetic energy operator contains the second-order derivative term and this eliminates the possibility of writing the kinetic energy operator in terms of the density. Since it is impossible to collect the wavefunction and its conjugate as a single norm square, a different approach should be deviced to enable this. This assumption states that we can find an auxiliary system with the same density $n(\vec{r})$ as our real system where the density may be written in terms of single-particle orbitals known as the Kohn-Sham Orbitals (KSO) [12].

$$n(\vec{r}) = \sum_{n}^{N_e} |\phi_n(\vec{r})|^2 \quad (2.16)$$

The kinetic energy of this auxiliary system can be written as the sum of the kinetic energies of the Kohn-Sham orbitals, although the result is not the same as the kinetic energy of the real many-body system. Therefore a correction term should be added to express the full kinetic energy

$$T = \sum_{i} \int \phi_i^*(\vec{r}) \nabla^2 \phi_i(\vec{r}) + \Delta T \quad (2.17)$$

2.2.2.2 Electron-Nuclei Potential Energy

The electron-nuclei potential energy operator is

$$\hat{V}_{ne} = -\sum_{I=1}^{N_n} \sum_{i=1}^{N_e} \frac{Z_I}{|\vec{r_i} - \vec{R_I}|} \quad (2.18)$$

The expectation value of the operator is

$$E_{ne} = \langle \psi(\vec{r}_1, \vec{r}_2 \ldots, \vec{r}_N) | \hat{V}_{ne} | \psi(\vec{r}_1, \vec{r}_2 \ldots, \vec{r}_N) \rangle \quad (2.19)$$

which can be written in integral form as

$$E_{ne} = -\sum_{I=1}^{N_n}\sum_{i=1}^{N_e}\int \psi^*(\vec{r}_1,\vec{r}_2\ldots,\vec{r}_N)\frac{Z_I}{|\vec{r_i}-\vec{R_I}|}\psi(\vec{r}_1,\vec{r}_2\ldots,\vec{r}_N)d\vec{r}_1 d\vec{r}_2 ... d\vec{r}_N \tag{2.20}$$

There is no derivative term in the operator, thus the wavefunction and its conjugate can be collected in a single norm square

$$E_{ne} = -\sum_{I=1}^{N_n}\sum_{i=1}^{N_e}\int |\psi(\vec{r}_1,\vec{r}_2\ldots,\vec{r}_N)|^2\frac{Z_I}{|\vec{r_i}-\vec{R_I}|}d\vec{r}_1 d\vec{r}_2 ... d\vec{r}_N \tag{2.21}$$

If the sum in Eq. 2.21 is expanded over electron index and all $\vec{r_i}$ index are collected under one index, which can then be written in terms of the density as

$$E_{ne} = -\sum_{I=1}^{N_n}\int \frac{Z_I}{|\vec{r}-\vec{R_I}|}dn(\vec{r})d\vec{r} = \int n(\vec{r})V_{ne}(\vec{r})d\vec{r} \tag{2.22}$$

without the need for any approximations.

2.2.2.3 Electron-Electron Potential Energy

The electron-electron potential energy operator is

$$\hat{V}_{ee} = \frac{1}{2}\sum_{i}^{N_e}\sum_{j\neq i}^{N_e}\frac{1}{|\vec{r_i}-\vec{r_j}|} \tag{2.23}$$

The expectation value of the operator

$$E_{ee} = \langle\psi(\vec{r}_1,\vec{r}_2\ldots,\vec{r}_N)|\hat{V}_{ee}|\psi(\vec{r}_1,\vec{r}_2\ldots,\vec{r}_N)\rangle \tag{2.24}$$

$$E_{ee} = \frac{1}{2}\sum_{i}^{N_e}\sum_{j\neq i}^{N_e}\int \psi^*(\vec{r}_1,\vec{r}_2\ldots,\vec{r}_N)\frac{1}{|\vec{r_i}-\vec{r_j}|}\psi(\vec{r}_1,\vec{r}_2\ldots,\vec{r}_N)d\vec{r}_1 d\vec{r}_2 ... d\vec{r}_N \tag{2.25}$$

Like electron-nuclei potential energy operator, electron-electron potential operator does not contain any derivative term, thus the wavefunction and its conjugate can be collected in a single norm square

$$E_{ee} = \frac{1}{2}\sum_{i}^{N_e}\sum_{j\neq i}^{N_e}\int \frac{1}{|\vec{r_i} - \vec{r_j}|}|\psi(\vec{r}_1, \vec{r}_2 \ldots, \vec{r}_N)|^2 d\vec{r}_1 d\vec{r}_2 ... d\vec{r}_N \tag{2.26}$$

If the integral is expanded over electron index and all $\vec{r_i}$ index are collected under one index

$$E_{ee} = \frac{1}{2}[\iint \frac{n(\vec{r}, \vec{r}')}{|\vec{r} - \vec{r}'|} d\vec{r} d\vec{r}' \tag{2.27}$$

where $n(\vec{r}, \vec{r}')$ term is the two-electron density. The two-particle density cannot be dealt within the Kohn-Sham framework but is written in terms of the uncorrelated two particle density and a correction,

$$n(\vec{r}, \vec{r}') = n(\vec{r})n(\vec{r}') + \Delta n(\vec{r}, \vec{r}') \tag{2.28}$$

Finally electron-electron potential energy becomes

$$E_{ee} = \iint \frac{n(\vec{r})n(\vec{r}')}{|\vec{r} - \vec{r}'|} d\vec{r} d\vec{r}' + \Delta E_{ee} \tag{2.29}$$

The ground state total electronic energy can be written by putting together all energies as

$$\begin{aligned} E_e = -\frac{1}{2}\int d\vec{r}\psi^*(\vec{r}_1, \vec{r}_2 \ldots, \vec{r}_N)\nabla^2\psi(\vec{r}_1, \vec{r}_2 \ldots, \vec{r}_N) \\ + \int n(\vec{r})V_{ne}(\vec{r})d\vec{r} + \frac{1}{2}\iint \frac{n(\vec{r})n(\vec{r}')}{|\vec{r} - \vec{r}'|} d\vec{r} d\vec{r}' + \Delta E_{ee} + \Delta T \end{aligned} \tag{2.30}$$

where $\Delta E_{ee} + \Delta T$ term is known as exchange-correlation energy [12]term. The exchange-correlation energy is expressed in an appropriate approximation.

2.3 The Theorems of Hohenberg and Kohn

In 1964, P.Hohenberg and W.Kohn presented two theorems which form the basis of modern DFT [13]. The first Hohenberg-Kohn Theorem states that there cannot be two different external potentials that give rise to the same ground state density. All properties of the system are

determined by its ground state density because the external potential describes the many-body system Hamiltonian and so the many-body wavefunction.

The proof of this statement of P. Hohenberg and W. Kohn begins with the assumption that the external potential is not uniquely determined by the electronic density and beyond that there are two external potentials $V_{ext}(\vec{r})$ and $V'_{ext}(\vec{r})$ having the same ground state density $n(\vec{r})$. Therefore, there are two different Hamiltonian operators $\hat{H}$ and $\hat{H}^{'}$ giving rise to two different wavefunctions ψ and $\psi^{'}$. Considering the variational principle

$$E_0 < \langle \psi' | \hat{H} | \psi' \rangle = \langle \psi' | \hat{H}' | \psi' \rangle + \langle \psi' | \hat{H} - \hat{H}' | \psi' \rangle = E'_0 + \int n(\vec{r})[V_{ext}(\vec{r}) - V_{ext}(r')\vec{]}d\vec{r} \quad (2.31)$$

$$E'_0 < \langle \psi | \hat{H}' | \psi \rangle = \langle \psi | \hat{H} | \psi \rangle + \langle \psi | \hat{H}' - \hat{H} | \psi \rangle = \quad (2.32)$$

$$E_0 - \int n(\vec{r})[V_{ext}(\vec{r}) - V_{ext}(r')\vec{]}d\vec{r} \quad (2.33)$$

Adding the two inequalities, we obtain

$$E_0 + E'_0 < E'_0 + E_0 \quad (2.34)$$

This result implies that there cannot be two different external potentials corresponding to the same electronic density for the ground state of a given system. In other words, the external potential is uniquely determined by the ground state electronic density, except for a trivial additive constant.

The second statement of the Hohenberg-Kohn Theorems claims that the treatment of the internal potential energy and the kinetic energy is the same for all physical systems. Based on the variational principle and the previous theorem, electronic energy can be expressed as

$$E_e[n] = F[n] + \int V_{ext}(\vec{r})n(\vec{r}) \quad (2.35)$$

where $F[n] = T[n] + E_{int}[n]$ is a universal functional.

Let the unique ground state density $n^0(\vec{r})$ determine the ground state energy E_0 and another density $n^1(\vec{r})$ correspond to the energy E_1. Considering the variational principle

$$E_0 = E[n^0(\vec{r})] = \langle\psi|\hat{H}|\psi\rangle < E_1 = E[n^1(\vec{r})] = \langle\psi^{'}|\hat{H}|\psi^{'}\rangle \tag{2.36}$$

Obviously the last equation shows that the total energy of the system which is expressed as the functional of the density can be minimized with respect to density and the density that minimize the total energy of the system is the ground state density.

2.4 Kohn-Sham Equations

W. Kohn and L. J. Sham introduced a practical method to apply the Hohenberg and Kohn theorem to real systems in 1965 [12]. They stated that the ground state energy as a functional of the electron density can be calculated by solving a set of single particle Schrödinger equations by introducing an auxiliary system of non-interacting electrons moving in an effective potential that is chosen such that its ground state electron density is the same as that of the real system.

Assuming that the density is well-behaved the ground state density, the functional E_e[n] can be minimized by varying the energy over all densities containing N electrons

$$\delta[E_e[n(\vec{r})] - \sum_{i,j} \lambda_{ij}(\langle\phi_i|\phi_j\rangle) - \delta_{ij}] = 0 \tag{2.37}$$

Here λ_{ij} are the Lagrange multipliers that ensure orthonormality of $\{|\phi_i>\}$.

The total energy is minimized with respect to the orbitals instead of density because the kinetic energy term can not be expressed in terms of density. The total energy can be minimized with respect to either orbitals or the complex conjugate of orbitals which yield equations that are complex conjugates of each other,

$$\frac{\delta}{\delta\phi_i^*(\vec{r})}\Big[E_e[n(\vec{r})] - \sum_{i,j} \lambda_{i,j}(\langle\phi_i|\phi_j\rangle) - \delta_{ij}\Big] = 0 \tag{2.38}$$

Substituting Eq. 2.36 into Eq. 2.37 yields

$$\frac{\delta}{\delta\phi_i^*(\vec{r})}\Big[-\frac{1}{2}\sum_n^{N_e}\int \phi_n^*(\vec{r})\nabla^2\phi_n(\vec{r})d\vec{r}\Big] + \frac{\delta}{\delta n(\vec{r})}\Big[\int n(\vec{r})V_{ext}(\vec{r})d\vec{r} + \frac{1}{2}\int\int \frac{n(\vec{r})n(\vec{r'})}{|\vec{r}-\vec{r'}|}d\vec{r}d\vec{r'} + \int n(\vec{r})\epsilon_{xc}[n(\vec{r})]d\vec{r}\Big]\frac{\delta n(\vec{r})}{\delta\phi_i^*} = \varepsilon_i\phi_i(\vec{r}), \quad (2.39)$$

where ϵ_{xc} is exchange-correlation energy and it is also a functional of $n(\vec{r})$. Using functional derivative properties and rearranging Eq.2.39, we obtain

$$\frac{-1}{2}\nabla^2\phi_i(\vec{r}) + \Big[V_{ext}(\vec{r}) + \frac{1}{2}\int \frac{n(\vec{r'})}{|\vec{r}-\vec{r'}|}d\vec{r'} + \epsilon_{xc}[n] + n(\vec{r})\frac{\delta\epsilon_{xc}[n]}{\delta n(\vec{r})}\Big]\phi_i(\vec{r}) = \varepsilon_i\phi_i(\vec{r}) \quad (2.40)$$

which can be written in short form as

$$-\frac{1}{2}\nabla^2\phi_i(\vec{r}) + [V_{ext}(\vec{r}) + V_{Hartree} + V_{xc}]\phi_i(\vec{r}) = \varepsilon_i\phi_i(\vec{r}) \quad (2.41)$$

where the sum of the terms in parentheses can be refered to as an effective potential, V_{eff}, and Eq.2.41 can be expressed in a form similar to a single-particle Schrödinger equation

$$[\hat{T} + V_{eff}]\phi_i(\vec{r}) = \varepsilon_i\phi_i(\vec{r}) \quad (2.42)$$

Eq. 2.41 describes a system of N equations called Kohn-Sham equations to be solved simultaneously. Furthermore, V_{eff} depends on the density directly and orbitals indirectly. Hence any change in the orbitals causes a change in the effective potential and Kohn-Sham equations should be solved self-consistently.

2.5 Exchange and Correlation Energy Functionals

The method to solve the many-body electronic problem introduced previously is based on dividing the total energy of the system into different contributions

$$E[n] = T + V_{ext} + E_{Hartree} + E_{xc} \tag{2.43}$$

First three terms are solved explicitly by considering an auxiliary system with the same electron density $n(\vec{r})$ as the real system but the last term is not tractable. Therefore, making this system easier to solve, there should be convenient approximations for the exchange-correlation energy term. There are several methods to approximate E_{xc}. The most widely used are the Local Density Approximation(LDA) and the Generalized Gradient Approximation(GGA)[16].

2.5.1 The Local Density Approximation (LDA)

The basic idea of the LDA is that the exchange-correlation energy per electron at a point $\vec{r}$ in a homogeous electron system, $\epsilon_{xc}^{LDA}(n(\vec{r}))$, having the same electron density with an inhomogenous electronic system, is equal to the exchange-correlation energy per electron at a point $\vec{r}$ in an inhomogeous electron system. The integration of the local energy terms over all the volume of the system gives the exchange-correlation energy functional

$$E_{xc}^{LDA}(n(\vec{r})) = \int n(\vec{r})\epsilon_{xc}^{hom}(n(\vec{r}))d\vec{r} \tag{2.44}$$

In Eq.2.44 the $\epsilon_{xc}^{hom}(n(\vec{r}))$ term is the sum of the exchange and correlation part seperately. The exchange part can be calculated exactly by the Hartree-Fock approach, however, correlation cannot be calculated analytically and approximations to correlation must be made. Although LDA gives generally underestimated results for the correlation part and overestimated result for the exchange part, the errors of both parts partially cancel each other.

Spin-polarized LDA is refered to as the local spin density approximation (LSDA) [11] and it is constructed by the spin-polarized expression. The exchange-correlation energy for spin-polarized systems is given by

$$E_{xc}^{LDA}(n^{\uparrow}(\vec{r}), n^{\downarrow}(\vec{r})) = \int [n^{\uparrow}(\vec{r}) + n^{\downarrow}(\vec{r})]\epsilon_{xc}^{hom}(n^{\uparrow}(\vec{r}), n^{\downarrow}(\vec{r}))d\vec{r} \tag{2.45}$$

where $n^{\downarrow}(\vec{r})$ is the density of down-spin electrons and $n^{\uparrow}(\vec{r})$ is the density of up-spin electrons.

2.5.2 The Generalized Gradient Approximation (GGA)

LDA is based on the idea that density of the system is not changing rapidly, however real systems do not usually obey this. For the Generalized Gradient Approximation (GGA) takes into account the inhomogeneity by considering density gradient contributions to exchange-correlation functionals. A convenient definition of the functional in the gradient form is [14]

$$E_{xc}^{GGA}[n^{\uparrow}, n^{\downarrow}] = \int d^3 r n(\vec{r}) \epsilon_{xc}(n^{\uparrow}, n^{\downarrow}, |\nabla n^{\uparrow}|, |\nabla n^{\downarrow}|, ...) \\ = \int d^3 r n(\vec{r}) \epsilon_x^{hom}(n) F_{xc}(n^{\uparrow}, n^{\downarrow}, |\nabla n^{\uparrow}|, |\nabla n^{\downarrow}|, ...) \quad (2.46)$$

where F_{xc} is a dimensionless functional of density and its various derivatives and $\epsilon_x^{hom}(n)$ is the exchange energy of the unpolarized gas system of density $n(r)$.

GGA usually provides improvements to total energies, atomization energies, energy barriers and structural energy differences [15].

2.6 Planewave Expansion

For the eigenstates of any independent Schrödinger like equations such as the Kohn-Sham equations in Eq. 2.41, planewaves (PW) are one of the suitable basis sets to solve these equations in periodic systems since PWs provide an easier way to solve Kohn-Sham equation. Kohn-Sham orbitals can be expanded in terms of PWs therefore Kohn-Sham equation can be represented in matrix form. Considering the expansion of the periodic functions in terms of PWs is the complete set of Fourier components due to Bloch's theorem [16], then the expansion of Kohn-Sham orbitals in terms of PWs

$$\psi_i(\vec{r}) = \sum_{\vec{q}} c_{i,\vec{q}} \frac{1}{\sqrt{\Omega}} exp(i\vec{q} \cdot \vec{r}) \equiv \sum_{\vec{q}} c_{i,\vec{q}} |\vec{q}\rangle \quad (2.47)$$

where $c_{i,\vec{q}}$ are the expansion coefficients of the wavefunction in the basis of orthonormal planewaves $|\vec{q}\rangle$ and $\frac{1}{\sqrt{\Omega}}$ is the normalization constant

To obtain the matrix form of the Kohn-Sham equation, the general form of the Kohn-Sham Hamiltonian, H_{eff}, is multiplied by the equation with $\langle\vec{q'}|$ from the left and integrating in real space one obtains

$$\sum_{\vec{q}}\langle\vec{q'}|\hat{H}_{eff}|\vec{q}\rangle c_{i,\vec{q}} = \varepsilon_i \sum_{\vec{q}}\langle\vec{q'}|\vec{q}\rangle c_{i,\vec{q}} = \varepsilon_i c_{i,\vec{q}} \tag{2.48}$$

The matrix element of the kinetic energy operator can be written as

$$\langle\vec{q'}| - \frac{\hbar^2}{2m_e}\nabla^2|\vec{q}\rangle = \frac{\hbar^2}{2m_e}|q|^2\delta_{\vec{q},\vec{q'}} \tag{2.49}$$

where the last term is in Hartree atomic units. Since $V_{eff}(\vec{r})$ has the periodicity for crystals, $V_{eff}(\vec{r})$ can be written as a sum of Fourier components in terms of the wavevectors in the reciprocal space of the crystal

$$V_{eff}(\vec{r}) = \sum_{m} V_{eff}(\vec{G}_m)exp(i\vec{G}_m \cdot \vec{r}) \tag{2.50}$$

where

$$V_{eff}(\vec{G}_m) = \frac{1}{\Omega_{cell}}\int_{\Omega_{cell}} V_{eff}(\vec{r})exp(-i\vec{G}_m \cdot \vec{r})d\vec{r} \tag{2.51}$$

The matrix elements of the effective potential

$$\langle\vec{q'}|V_{eff}|\vec{q}\rangle = \sum V_{eff}(\vec{G}_m)\delta_{\vec{q'}-\vec{q},\vec{G}_m} \tag{2.52}$$

Eq.2.52 is nonzero if only if $\vec{q}$ and $\vec{q'}$ are different from the $\vec{G}_m$. Hence, $\vec{q'}$ and $\vec{q}$ can be defined with the wavevector k such that $\vec{q} = k + \vec{G}_m$ and $\vec{q'} = k + \vec{G}_{m'}$

For a given any k, the Schrödinger-like equation can be expressed as the matrix equation such that:

$$\sum_{m'} \hat{H}_{m,m'}(\vec{k}) c_{i,m'}(\vec{k}) = \varepsilon_i(\vec{k}) c_{i,m}(\vec{k}) \tag{2.53}$$

where

$$\hat{H}_{m,m'}(\vec{k}) = \langle \vec{k} + \vec{G}_{m'} | \hat{H}_{eff} | \vec{k} + \vec{G}_m \rangle = \frac{\hbar^2}{2m_e} |\vec{k} + \vec{G}_m|^2 \delta_{m',m} + V_{eff}(\vec{G}_m - \vec{G}_{m'}) \tag{2.54}$$

As seen in the Eq.2.54, the effective potential depends on the difference between two reciprocal lattice vectors $\vec{G}_m$ and $\vec{G}_{m'}$. Since the Hamiltonian is dependent on the wavevector $\vec{k}$, other terms in the total energy such as Hartree, exchange-correlation etc. should be written in terms of wavevector $\vec{k}$. After that planewave basis set provides a complete solution of the Schrödinger-like equation of a system.

A limitation is necessary for the PW expansion to make calculation with PW-DFT codes. This limitation is imposed through

$$\frac{1}{2} |\vec{G}|^2 < E_{cut} \tag{2.55}$$

where E_{cut} is a suitably chosen cutoff energy.

2.7 Pseudopotentials

The basic idea of pseudopotentials is dividing the electronic states of an atom into two parts: core and valence states. Since core electrons are strongly bonded to nuclei, they are not affected by the change of their environment considerably in this way the definition of the valence wavefunction inside the core region is not necessary. On the contrary, valence electrons are affected by any changes in their environment and the valance states exhibit rapid oscillation close to the core regions. To solve the valence states, a large number of planewaves is needed which causes further increases the cost of the computational works.

The aim of the pseudopotential is to make the valance orbitals smooter in the core region as taking into consideration the balance between transferability and efficiency of the pseudo wavefunction. To generate a pseudopotential, the core electrons are removed from calculation, and the interaction between the valance electrons and the nucleus including orthogonalization is replaced by an effective potential which depends on the angular momentum of the valance electrons. Kohn-Sham orbitals for an isolated atom are solved and a certain radius named cutoff radius, r_{cutoff}, is determined. The important point is to choose accurate r_{cutoff} for the generating pseudopotential. Although small r_{cutoff} gives good transferability, it brings difficulty to obtain smooter pseudopotential. Despite of providing smoother pseudopotential, larger r_{cutoff} do not provide good transferability. Therefore r_{cutoff} should be choosen carefully to obtain both good transferability and smoother pseudopotential. At r_{cutoff} , the pseudo wave function should obey these conditions:

- Beyond the cutoff radius, pseudo wave function should decay exactly same with the all-electron wave function,
- Eigenvalues of the pseudo and all-electron wave functions of the valence state should be the same,
- The logaritmic derivatives of the pseudo and all-electron wave function at the r_{cutoff} should be the same.

In the litarature, there are two types pseudopotentials mostly used for DFT calculations: *Norm−conserving pseudopotentials* [11] and *ultrasoft pseudopotentials* [14].The norm conserving pseudopotential is a non-local approach due to the dependency of angular momentum. The construction requirements of norm-conserving pseudopotentials are to keep the properties of the reference system. In addition to the conditions emphasized above the pseudo system should agree with the all-electron system in terms of the norm square integrations and the energy derivatives inside the region of the r_{cutoff} . Hence, the generated pseudopotential provides a potential that exhibits good transferability and smoothness as long as one choses the proper cutoff radius. On the contrary, ultrasoft pseudopatential does not require norm conservation and it is based on redefining the non-local potential in the form of smooth wavefunction. The new wavefunction differs from all-electron and pseudo wavefunctions, however, it keeps the high accuracy results. Ultrasoft pseudopotentails provide easier way than norm-conserving pseudopotantials since it needs less number of planewaves and gives

an opportunity to chose larger cutoff radius.

2.8 Hellmann-Feynman Theorem

After the system reaches the self-consistent solution, the density corresponded by the Kohn-Sham orbitals should be used to calculate some properties of the system such as forces on the atoms with appropriate accuracy and inexpensive manner. The Hellmann−Feynman theorem [14] is the satisfying method for calculation forces on atoms. The theorem is related to the a derivative of the total energy of a system and it suggests that all the forces in the system can be calculated with the classical electrostatics approach if the spatial distribution of the charged particles is determined by solving the Schrödinger equation. The clasical force on an I^{th} atom or ion can be written as:

$$\vec{F}_I = -\frac{\delta E}{\delta \vec{R}_I} \tag{2.56}$$

where $E = \langle\psi|\hat{H}|\psi\rangle$ or $\hat{H}\psi = E\psi$ and substituting E in the Eq. 2.56

$$\vec{F}_I = -\left[\langle\frac{\delta\psi}{\delta\vec{R}_I}|\hat{H}|\psi\rangle + \langle\psi|\frac{\delta\hat{H}}{\delta\vec{R}_I}\psi\rangle + \langle\psi|\hat{H}|\frac{\delta\psi}{\delta\vec{R}_I}\rangle\right] \tag{2.57}$$

$$\vec{F}_I = -\left[\langle\frac{\delta\psi}{\delta\vec{R}_I}|E\psi\rangle + \langle\psi|\frac{\delta\hat{H}}{\delta\vec{R}_I}\psi\rangle + \langle E\psi|\frac{\delta\psi}{\delta\vec{R}_I}\rangle\right] \tag{2.58}$$

Since the eigen values of $\hat{H}$ are real and wavefunctions are normalized $\langle\psi|\psi\rangle$=constant, than the first and third terms must equal to zero such that:

$$\langle\frac{\delta\psi}{\delta\vec{R}_I}|E\psi\rangle + \langle E\psi|\frac{\delta\psi}{\delta\vec{R}_I}\rangle = E\frac{\delta}{\delta\vec{R}_I}\langle\psi|\psi\rangle = 0 \tag{2.59}$$

$$\vec{F}_I = -\langle\psi|\frac{\delta\hat{H}}{\delta\vec{R}_I}|\psi\rangle \tag{2.60}$$

By this way, forces can be calculated only based on the change in the Hamiltonian operator and so regarding of the change in the wavefunctions can be neglected to simplify the DFT

calculations. After adding the ionic and electronic contributions to total force on the I^{th} atom

$$\vec{F_I} = -\int d\vec{r} n(\vec{r}) \frac{\delta V_{ext}}{\delta \vec{R_I}} - \frac{\delta E_{II}}{\delta \vec{R_I}} \tag{2.61}$$

2.9 Self-Consistent Cycle of the Kohn-Sham Equations

As mentioned before, the Kohn-Sham equations are the single particle Schrödinger like equations and the effective potential depends on the density directly and it depends on the orbitals that determine the density indirectly. Therefore the Kohn-Sham equations must be solved self-consistently. The density is calculated from a given potential V_{in}, on the other hand, the effective potential V_{eff} is calculated by the density n. This implies that taking initial density as an input and then a new density is found and then a new density is put into the equation system to obtain an output density and the new potential. This process must continue till reaching good convergency results. This self-consistent cycle can be explained by these steps:

- Start from a trial density n($\vec{r}$),

- Calculate the effective potential, V_{eff},

$$V_{eff} = V_{ext}(\vec{r}) + V_{Hartree} + V_{xc} \tag{2.62}$$

- Solve the Kohn-Sham equation and obtain new Kohn-Sham orbitals,

$$[\hat{T} + V_{eff}]\phi_i(\vec{r}) = \varepsilon_i \phi_i(\vec{r}) \tag{2.63}$$

- Calculate the new density n$'$($\vec{r}$).

This process continues until the differences between the two electron densities, n($\vec{r}$) and n$'$($\vec{r}$), are the same or below a pre-determined small number. In other word, the input and output electron densities should agree with each other in order to solve the Kohn-Sham equations. After finding the solution of the Kohn-Sham equations, forces, energies etc. can be calculated.

CHAPTER 3

γ-Al_2O_3 SUPPORT MATERIAL FOR THE NO_x STORAGE-REDUCTION (NSR) CATALYST SYSTEM

The control of NO_x (NO, NO_2) and CO_2 emissions generated from combustion process of vehicles and power stations have become a significant research area since emission of NO_x causes serious damages to the environment such as photochemical smog and formation of acid rains which harm plants, animals and also human health [17]. The NSR catalysis is one of the promising candidates for reducing NO_x emissions and it is an appropiriate alternative for worldwide environmental regulations.

3.1 NSR Catalysis

Lean-burn engines operate with oxygen in a certain stoichiometric air to fuel ratio (A/F) for the combustion process (A/F =14.7 for gasoline engines and A/F =20-25 for diesel engines) and gasoline engines run little or no amount of presence of oxygen in the exhaust [18]. Besides, diesel engines are more efficient than gasoline engines while keeping the consumption at a lower level when burn the fuel and releasing less amount of CO_2. Under these conditions, the conventional three-way catalysts are not sufficient for NO_x reduction because of the presence of excess oxygen. However, the NSR catalyst exhibits increased efficiency for the reduction of NO_x emission.

The NSR catalysis has been studied extensively in the recent years. Among these works alkaline and alkaline earth oxide (AEO) based NSR catalysts are the most popular issue. Alkaline and alkaline earth oxide based the NSR catalysts especially Pt-Rh/BaO/Al_2O_3, were intro-

duced by Toyota in the mid 1990s [19]. This NSR catalyst consists of three main parts. These are precious metals (Pt, Rh, Pd) operating as the catalytic redox component, an alkali earth oxide (BaO, MgO, CaO, SrO, K_2O) operating as NO_x storage component and finally a high surface area support material (γ-Al_2O_3, TiO_2, ZrO_2). The NSR catalysts operate in a cyclic manner during the lean-burn and oxygen rich periods. This cycle can be broken down into five steps [5].

1- NO oxidation to NO_2 on the precious metal
2- NO_x storage on the surface of alkali earth oxides in the form of nitrate
3- Reductant evolution
4- NO_x extraction from trapping sites
5- NO_x reduction to N_2

Each of the step above includes complex reaction steps and many factors affect the mechanism such as reduction agents such as H_2, CO, C_3H_6, dopant materials and H_2O. M. Weibel et al. mentioned that these steps can be elucidated by the global reaction kinetic model for the NSR catalysts and the reaction rate values of these steps, including NH_3 formation and consumption [6].

Increasing the catalytic activity of the NSR catalysts has been the subject of numerous studies in literature. Mixed-oxide support materials, such as CeO_2-ZrO_2 [20], ZrO_2-TiO_2 [21]; different methods for catalyst fabrication [22] and morphology of the precious metal [23,24,25] are only some of the issues considered in experimental and theoretical literature.

Sulphur poisoning is another important subject for the NSR catalysis. Sulphur is one of the elements included by the fuel and after the combustion process it exists in a form of sulphur oxide SO_x, i.e SO_2 and SO_3. SO_2 interacts with the catalyst storage component and generates sulfate salts that causes deactivation of the catalyst [26]. Effects of the precious metals (Pt, Rh, Pd) and tolerance capacity of the support materials (γ-Al_2O_3, TiO_2, ZrO_2) are still under investigation.

3.2 Storage Materials Investigations for the NSR Catalysts

In NSR catalysis, NO_x is stored on the surface of alkaline earth oxides (BaO, MgO, CaO, SrO) during the lean period. Determining the convenient alkaline earth oxide (AEO) and the contribution of the AEO component to catalytic activity are debated subjects for the NSR catalysis. However the mechanism of the NO_x storage with the AEO component is clear. Kwak et al. explained the uptake mechanism of NO_x for $Pt/BaO/Al_2O_3$ catalyst and they stated that two different NO_x uptake mechanism observed [4]. The first one included Pt and the other one bulk nitrates. It was concluded in this study that the NO_2 produced by $NO+O_2$ on the Pt was initially transferred to BaO through a spillover mechanism and this process continued until a certain amount of $Ba(NO_3)_2$ formed around the Pt. In addition to this spill-over process, gas phase NO_2 adsorption continued depending on the bulk diffusion rate of nitrates. Also Cant et al. investigated the spillover processes (forward and reverse) between Pt and BaO using different catalysis systems (BaO/Al_2O_3, Pt/SiO_2, BaO/Al_2O_3+Pt/SiO_2 and $Pt/BaO/Al_2O_3$) with temparature-programmed desorption (TPD) method [27]. One of the results was that the reduction of stored NO_x on the $Pt/BaO/Al_2O_3$ catalyst was faster than others in which BaO and Pt were seperated from each other. Furthermore, Su et al. agreed with Ref. [30] regarding lower catalytic activity of BaO/Al_2O_3 in the absence of Pt [28].

The widely used BaO and other AEOs have also been investigated. Verrier et al. worked with different AEOs (BaO, MgO, CaO and SrO) and compared their catalytic activities on the γ-Al_2O_3 support material during NO_2 uptake and release [29]. They used Fourier transform infrared spectroscopy (FTIR), N-solid magic angle spinning nuclear magnetic resonance (MAS NMR) and TPD methods for the comparison of AEOs. Results of this work suggested that the amount of the surface and bulk nitrates were related with the basicity property of the AEO and the presence of water. The amount of the surface nitrates decreased and the amount of the bulk nitrates increased when the basicity of the AEO increased. Consequently the order of the storage capacities of the catalysis arranged in decreasing capacity was determined as BaO $\geqslant$ SrO > CaO >MgO. Thus BaO is the one of the most favorable AEOs for the NSR catalysts.

3.3 Noble Metal Investigations for the NSR Catalysts

Noble metals are widely used in the petrochemical industrial area for refinement of petroleum and conversion of exhaust gases. In the NSR catalysts, noble metals have an important role in increasing the catalytic activity and act as a catalytic redox component. Among these metals Pd, Pt and Rh are the most widely used due to their high selectivity. In the literature, several studies have been conducted to examine the contribution of Pd, Pt and Rh to the catalytic activity, including clusters of single kind of metals, monolayers or their bimetalic alloys.

Although Pd does not have good reduction efficiency, it is still one of the preferred precious metals for catalysis due to its low cost. Macleod and Lambert investigated the NO_x reduction with H_2+CO under oxygen-rich conditions for Pd/TiO_2- Al_2O_3, Pd/TiO_2 and Pd/Al_2O_3 at low temparature and they stated that Pd/TiO_2- Al_2O_3 exhibited more resistance to sulphur poisoning and it had high degree of NO_x conversion in wide-range of H_2:CO ratio [30]. Also Lee and Gulari worked with Pd/Al_2O_3 catalyst at low temparature and in the presence of H_2+CO [31]. Their research was done for development of the NO_x reduction performance and they compared the Pd/Al_2O_3 and $PdCl_2$/Al_2O_3 catalysis. The results of this work showed that using $PdCl_2$ as a metal precursor improved the NO_x reduction to N_2. Besides these experimental studies, Pd is also popular for theoretical studies. Especially first principle (DFT) studies have been performed for single Pd, clusters of Pd and the monolayer model of Pd. Valero et al. examined the effects of the hydroxylation of γ-Al_2O_3 surfaces on the diffusion and stability of single Pd atom using DFT [32]. They compared dehydrated (100) and (110) surfaces and hydrated (110) surface of γ-Al_2O_3. It was found that presence of hydroxyl group caused a decrease in the catalytic activity because Pd atom interacted with the OH groups instead of interacting with surface five-fold coordinated Al (Al_{penta}) and O atoms strongly. Furthermore, it was discovered that Pd donated electrical charge to the surface and the mobility of the Pd atom was lower on the hydrated surface than dehydrated surfaces. Another study of Valero et al. is based on Pd_n (n=1-5) clusters on the γ-Al_2O_3 surface [25]. Free Pd_n clusters were modelled and their adsorptions on the both surfaces dehydrated (100) and hydrated (110) surface of γ-Al_2O_3 were investigated. Pd_3 cluster was found to be the most stable for both surfaces due to its 2-dimensional raft like shape. Pd_4 and Pd_5 clusters became 3-dimensional accompained by a decrease in the adsorption energies. Moreover, the hydrated surface results agreed

with their previous work. It was observed that the Pd-O bond strength decreased, as a result of this, the Pd-Pd bonds became stronger therefore the number of Pd atoms in clusters increased.

Pt is another commonly used precious metal in the NSR catalysts in spite of its high cost and its adsorption behaviour is still under search. Olsson and Fridell worked on the influence of Pt oxide formation and dispersion over Pt/Al_2O_3 and $Pt/BaO/Al_2O_3$ catalysis during NO_x reduction with TPD experiments and with two flow reactors (O_2-CO-TPD, NO_x-TPD) [22]. The formation of platinum oxide after exposing gas flows (NO_2/ Ar, O_2/Ar, NO_2+ O_2) was found to act as an inhibitor for catalysis and platinum oxide was observed in the form of PtO and PtO_2 on the surface by X-ray photoelectron spectroscopy (XPS). Moreover, Pt/Al_2O_3 was discovered to be more active than $Pt/BaO/Al_2O_3$ catalyst because BaO caused a great amount of platinum oxide formation. Donghai Mei et al. worked on the active binding sites of γ-Al_2O_3 for binding Pt [33]. It was claimed that Al^{+3}_{penta} sites were the active sites and Pt bonded with these sites. Therefore strong Pt-Al^{+3}_{penta} interactions were observed by high-angle annular dark-field scanning transmission electron microscopy (HA-ADF STEM) and MAS-NMR. Increasing the loading of Pt on the surface causes formation of 2-dimensional Pt rafts. DFT calculations were also done and their results agreed with the experimental results. Another DFT study of Denkins and Mei et al. is the adsorption of single Pt atom on the γ-Al_2O_3 surface [23]. Two different γ-Al_2O_3 models (Digne [34] and Pinto [35] models) were used in this study and binding energies were compared with each other. Besides, different adsorption configurations were examined and one of them gave unpredictable result such that Pt atom bonded surface O atom initially moved into the surface and this configuration gave the highest binding energy of Pt atom on the surface (-3.50 eV). Except that, it was found that Pt atom preferred O atom-bond and also bridge configurations on O-Al atoms occurred. In contrast to Pd, Pt was charged negatively, however, similarly Pd, presence of hydroxyls caused decreasing in the catalytic activity. The two models used gave similar results in the adsorption manner and range of the adsorption energies. According to kinetic Monte Carlo method results, it was also claimed that the Pt atom preferred sites in the vicinity of the Al atom at low temparature but when temperature increased it moved across different region of the surface giving way to the formation of larger clusters.

Rh is another noble metal used in the NSR catalysis with γ-Al_2O_3. Despite the fact that Rh

has not been studied specifically with DFT method in the literature like Pt and Pd, experimental works have performed for Rh with different approaches. Suarez et al. worked on the Rh/γ-Al_2O_3-sepoilite monolithic catalysts to investigate formation of N_2O in the presence of oxygen [36]. Rh loading to γ-Al_2O_3-sepoilite monolithic catalysts between 0.2 % and 0.8 % weight ratio and it was reported that higher Rh loading enhanced the activity of the catalysts due to increasing in the N_2O conversion. Increasing the catalytic activity was found to scale with the number of active sites. Another important point was that excess of oxygen did not affect the activity of the catalysts. Another study of the Suarez et al. concentrated on the Rh/TiO_2 sepiolite monolithic catalyst for N_2O decomposition [37]. By contrast to Rh/γ-Al_2O_3 results, lower Rh loading (0.2 wt %) gave the best performance of the catalysts because the formation of larger Rh particles caused a decrease of the reaction rate of N_2O decomposition. Therefore catalytic activity decreased and it was stated that the formation of metal oxide was prevented by TiO_2-sepoilite monolithic catalysts. The decomposition of the N_2O was also examined with the promotion of the alkali-metals (Li, K, Na, Cs)[38]. It was seen that promoters supplied higher dispersion of Rh, in this way, the catalytic activity of the Rh/γ-Al_2O_3 catalyst was increased. C. D. Zeinalipour-Yazdi et al. investigated the CO adsorption on Rh/γ-Al_2O_3 catalyst by using DFT calculations and DRIFTS studies [39]. It was observed that inreasing the metal coverage on the surface caused a decrease of the adsorption energy because of enhancement of the dipole-dipole repulsion between Rh atoms. Using DFT calculations, an isolated Rh_4 cluster (tetrahedral configuration) was simulated and bridge configuration of CO on the cluster was found to be the most stable configuration which agreed with DRIFTS studies.

Jelic et al. studied Pd and Pt pseudomorphic monolayer catalysis for NO_x storage and they considered monolayers on the host metals (Au, Ir, Rh, Cu, Ru, Pd) and the subsurface layer [24]. They compared the activation energies, segregation energies and adsorption energies of NO and NO_2 for systems exposing NO and O. It was concluded that for the Pt monolayer, the largest adsorption energies for NO and NO_2 were both found on the Au. For the Pd monolayer, the largest adsorption energies for NO and NO_2 were both on the Au as host metal systems. Also Pd monolayer adsorption energies were slightly higher than adsorption energies of Pt monolayer. In addition, it was stated that the change in the d-band due to charge transfers affected the NO adsorption unlike the NO_2 adsorption. Salasc and Fridell et

al. compared the performances of Pt and Pd in NO_x storage on BaO/Al_2O_3 in which Al_2O_3 consisted of 80 wt % γ-Al_2O_3 and 20 wt % boehmite with XPS studies and the TPD measurements [40]. It was seen that $Pd/BaO/Al_2O_3$ had higher storage capacity at low temperature (300^oC) than $Pt/BaO/Al_2O_3$ however at higher temparature (400^oC) $Pt/BaO/Al_2O_3$ gave better storage result. The reason why $Pt/BaO/Al_2O_3$ became more sensitive as temparature was increased was explained by the observation that BaO acted as a hinder for self-poisoning of metal sites. Moreover, it was stated that Pt was more efficient for NO oxidation process but NO_2 was more strongly bound to $Pd/BaO/Al_2O_3$ than $Pt/BaO/Al_2O_3$. Similarly to Fridell et al., $Pt/BaO/Al_2O_3$ and $Pd/BaO/Al_2O_3$ NSrs were investigated by Amiridis et al. reactor and in situ FTIR studies between the temperature range 250-375^oC using the gas flows C_3H_6+He and NO/O_2/He [41]. After exposing C_3H_6+He gas mixture at 275^oC, $Pt/BaO/Al_2O_3$ catalyst exhibited lower NO_x storage capacity than $Pd/BaO/Al_2O_3$ and propylene (C_3H_6) activation activity was also lower for Pt than Pd due to lower oxidation activity of Pt. Furthermore, the accumulation of the surface carboxylates on $Pt/BaO/Al_2O_3$ catalyst hindered the formation of nitrite and nitrate species consequently NO_x storage capacity was decreased. Both catalysis showed higher activity at higher temparature (350^oC) and the difference between catalysis was that concentration of the nitrite species on the surface of $Pd/BaO/Al_2O_3$ catalyst was observed to be slightly higher than $Pt/BaO/Al_2O_3$ catalyst. Both investigations [40, 41] agreed that $Pd/BaO/Al_2O_3$ catalyst indicated higher catalytic activity than $Pt/BaO/Al_2O_3$ at below 300^oC.

Dimick et al. examined the contributions of the noble metals for Pt/γ-Al_2O_3, Rh/γ-Al_2O_3 and Pt-Rh/γ-Al_2O_3 using FTIR [42]. Especially, adsorption of NO in a linear configuration on Pt was mentioned for Pt/γ-Al_2O_3 and Pt-Rh/γ-Al_2O_3 catalysis. In contrast to Pt, NO was observed neutral or cationic (Rh/γ-Al_2O_3 and 90/10 wt. Pt-Rh/γ-Al_2O_3) or anionic (95/5 wt. Pt-Rh/γ-Al_2O_3). In addition, it was concluded that 95/5 wt. Pt-Rh/γ-Al_2O_3 catalyst was more active than 90/10 wt. Pt-Rh/γ-Al_2O_3 because of the different roles of Pt and Rh on surface of the catalyst and difference between the morphology of the catalysis. Rh was described as a single atom surrounded by Pt atoms on 95/5 wt. Pt-Rh/γ-Al_2O_3 and Rh clusters on 90/10 wt. Pt-Rh/γ-Al_2O_3 were also surrounded by Pt atoms. In addition, Pt atoms enabled sites for the dissociative adsorption of H_2 while Rh atoms provided a site for the dissociative adsorption of NO during the reduction of NO with H_2. Higher Rh loading caused a decrease in the catalytic

activity because Rh atoms on the surface had a partially oxidized character and they acted as an inhibitor for NO adsorption and dissociation. Resembling in many respects to the study of Dimick et al., Hu et al. worked on the Pt-Rh synergism for the Al_2O_3 based NSR catalysts in the gas conversion of HC/CO/NO mixture at 400^oC [43]. They observed that under oxidizing condition Rh deactivated and the formation of larger size of Pt clusters also caused a decrease in the catalytic activity at high temperature. Rh was described as the main active part of the catalyst with help from Pt. Mainly it was stated that Rh-Pt/ Al_2O_3 alloy catalyst exhibited higher catalytic activity than Rh/Al_2O_3 or Pt/Al_2O_3 catalysis. Rh-Pt bimetallic nanoparticles and clusters were also studied using DFT method and electronic sturucture of bimetallics and segregation paths were investigated in the literature [44, 45].

3.4 Investigations of the Support Materials for the NSR Catalyst

Support materials are another crucial factor for the NSR catalysts. Tolerating sulphur poisoning and high efficiency on storage-reduction process are the main selective properties of the support materials. In literature, there are several support materials used for NO_x catalysis such as TiO_2, Al_2O_3, ZrO_2, SiO_2, CeO_2 etc. Some of the most commonly studied alternative materials are γ-Al_2O_3 and TiO_2 for the NSR catalysis and they are studied widely in literature. Han et al. studied anatase phase of TiO_2 (101) surface with DFT calculation to investigate the interaction between Pt clusters and surface of the anatase TiO_2 [46]. They examined adsorption of Pt_n (n=1,2,3) clusters on TiO_2 and concluded that increasing the number of Pt atoms caused strong Pt-Pt bonding and 3-dimensional Pt clusters were seen. Also Pt atoms prefered coordinatevely unsatured sites and O atoms similarly Pt atoms on γ-Al_2O_3 [23]. L. Li et al. worked Pt/TiO_2 catalyst to examine oxidation of NO by FTIR spectra in the presence of SO_2 gas flow [49]. Despite using NO in the gas mixture, SO_2 adsorption and oxidation was not affected by NO but presence of SO_2 caused changes in the formation of surface nitrates and nitrites and it was seen that SO_2 prevented the formation of unstable surface nitrates. Also, it was proven that NO oxidation was lower for TiO_2 catalyst without Pt. Takahashi et al. investigated Pt/K on the mixed support material catalysts made of ZrO_2 and TiO_2 to obtain higher sulphur tolerance [22]. It was found that the best mixture of the catalyst consisting of 70 % ZrO_2+ 30 % TiO_2 exhibited the highest NO_x removal ability and K acted as an inhibitor for NO_x removal of the surface.

CHAPTER 4

CALCULATIONS and DISCUSSION

4.1 Bulk Structure of γ-Al_2O_3

Al_2O_3 is a crucial industrial material used widely in many technological applications, for example, electrical insulators, tunneling barriers and catalysis [48]. Alumina has several metastable phases named 'transition aluminas' such as β, θ, η, κ, χ , γ and one thermodynamically stable phase called corondum α-Al_2O_3 [49].

Among all the phases, γ-Al_2O_3 exhibits unique properties, such as high surface area and these unique properties lead to be an attractive choice to be used as catalysts and catalyst support material [50]. Even though γ-Al_2O_3 is used widely in industry, especially in petrochemical industry, its structure is still under debate. Positions of vacancies, the space group of γ-Al_2O_3 (cubic or tetragonal space group), the appropriate model (spinel or nonspinel) and presence of H in the bulk are the main questions about the structure of γ-Al_2O_3. In the literature it is reported that there are two ways to derive γ-Al_2O_3. The first one is through the use of mineral spinel $MgAl_2O_4$ and the other is via dehydration of boehmite (AlOOH). It is claimed that γ-Al_2O_3 derived from boehmite has cubic and tetragonal lattice [51] whereas γ-Al_2O_3 derived from spinel $MgAl_2O_4$ has spinel cubic lattice [52].

Derivation of γ-Al_2O_3 from spinel $MgAl_2O_4$ is based on switching Mg atoms with Al atoms in the structure and determination of vacancies. It is claimed that γ-Al_2O_3 derived from spinel $MgAl_2O_4$ has spinel cubic structure [51]. Based on this, Gutierrez at al. stated that γ-Al_2O_3 is described as defective spinel, expressed as $\square_{2\frac{2}{3}}Al_{21\frac{1}{3}}O_{32}$ ($\square$=vacancies) referring a cubic

cell structure including 24 cation sites in tetrahedral and octahedral position with 32 O atoms on a fcc lattice [52]. To reach the Al_2O_3 stoichiometry, the unit cell must be enlarged by a factor of 3 and an average number $2\frac{2}{3}$ of cation vacancies must be introduced for per unit cell. However, ambiguity remains regarding the location of vacancies, and the ratio of vacancies in octahedral positions to in tetrahedral positions. Paglia et al. mentioned that according to results of XRD, electron microscopy and NMR studies, vacancies occupy completely octahedral or tetrahedral positions or a mixture of both [54]. Due to ambiguity in the placement of vacancies, there exist many configurations of distribution of the vacancies. This makes it necessary to use extended unit cells which cause difficulties for studying γ-Al_2O_3 computationally. Gutierrez et al. succeed decreasing the number of atoms in the unit cell by DFT study and thereby the number of possible configurations of vacancies were also decreased [52]. The unit cell introduced by Gutierrez et al. had 40 atoms (24 O atoms and 16 Al atoms) and 2 vacancies. In addition, 14 inequivalent configurations of vacancies were determined and their energies were calculated using DFT and the minimum energy configuration was found to be in which two vacancies were in octahedral positions and DOS (Density of States) calculations also supported the result.

In contrast to the other transition aluminas, γ-Al_2O_3 presents difficulties in determining the structure because of vacancies and poor crystallinity. Krokidis et al. attempted to elucidate the pathway of the transformation of boehmite into γ-Al_2O_3 using both molecular dynamics simulations and XRD patterns [53]. Krokidis et al. stated that boehmite-derived γ-Al_2O_3 is obtained by dehydration of boehmite which has an orthorhombic layered structure held together by hydrogen bonds [53]. During the dehydration process, transition aluminas are observed depending on the temperature of operation. It was concluded that this transformation could be described in four steps. Starting with hydrogen transfer and the following steps claimed that the structure sheared as a consequence of structural collapse which was due to the extraction of water from the structure. Recently, contrary to the results of the Gutierrez et al. [52], it was asserted that migration of Al atoms were towards tetrahedral sites from octahedral sites and that unoccupied tetrahedral positions were assigned to vacancies. Paglia et al. studied the tetragonal structure model for boehmite-derived γ-Al_2O_3 with NMR, TEM and neutron diffraction [51]. It was concluded that although γ-Al_2O_3 is widely regarded as belonging to the cubic space group Fd3m, it was better described by the tetragonal space

group $I4_l/amd$ since boehmite-derived γ-Al_2O_3 had tetragonal distortion. Another conclusion reached in this work was that Al cations could not occupy both tetrahedral and octahedral positions, in other words, each Al could only be located either in a tetrahedral or octahedral position. However, vacancies could be placed in tetrahedral or octahedral positions. In addition, it was suggested that the most stable model for γ-Al_2O_3 consisted of 25 % tetrahedral aluminum (Al_{tetra}) [34].

The other unresolved debate is on whether spinel or nonspinel structure is more appropriate for describing γ-Al_2O_3. Sun et al. studied spinel and nonspinel structural models with DFT and the Rietveld refinement simulation method [54]. Their work also included both the presence of hydrogen in the bulk material (fully and partially hydrogenated structures) and fully dehydrated structure. Spinel structure models of γ-Al_2O_3 in this work derived from mineral spinel structure $MgAl_2O_4$ and the nonspinel model derived from boehmite (AlOOH). In this study, spinel models were identified as more convenient choice than a nonspinel model according to synchrotron X-ray power diffraction (SXPD) results. On the contrary, another computational study done by Paglia et al. claimed opposite results. Paglia et al. examined the structure of γ-Al_2O_3 using both an interatomic potential and DFT calculations [55]. Cubic and tetragonal spinel and nonspinel models were studied using a large number of possible models of γ-Al_2O_3. It was found that spinel structures were not the most energetically favorable because the lowest energy configurations belong to the nonspinel structure. In addition, it was stated that the diffraction pattern of nonspinel models yielded better matches to the experimental diffraction pattern of γ-Al_2O_3 and the tetragonal structure model attained more accurate results to describe the structure of γ-Al_2O_3 with an a/c ratio of 2.001.

In this thesis, nonspinel, tetragonal and fully dehydrated bulk structure model of γ-Al_2O_3 with no vacancies was used for the DFT calculations. This model was derived from a model created by Digne et. al [34] which is one of the most popular models for the γ-Al_2O_3 in the literature. Unit cell of the model consists of 16 Al atoms (Al_{tetra}/Al_{octa}=0.33 or 25 % Al_{tetra}) and 24 O atoms (Fig. 4.1) and a 2x1 unitcell was used for all calculations.

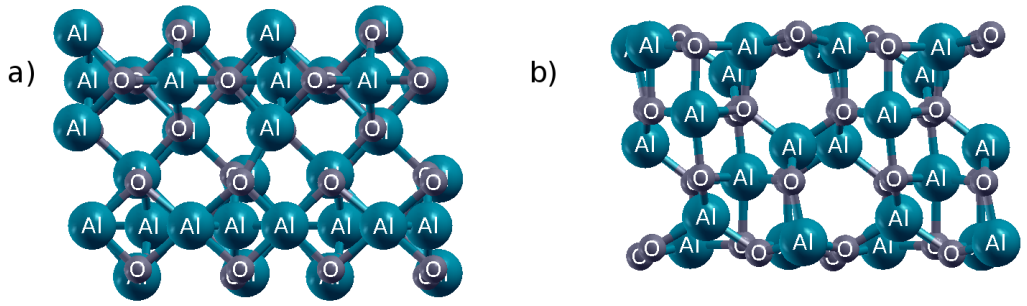

Figure 4.1: (a) Top view and (b) side view of the (2x1) cell of bulk γ-Al_2O_3

4.2 Surface Studies of γ-Al_2O_3

In this thesis the (100) surface was studied to investigate the performance of Pt and Rh atoms as a single metal and small Pt/Rh clusters on the γ-Al_2O_3 for the NO_2 adsorption using DFT calculations. Although the (100) surface is not the energetically most favorable for the non-spinel γ-Al_2O_3 structure, it is widely studied due to having large number of Al_{penta} sites, which are claimed to be the most probable nucleation sites of Pt [33] and BaO [8] for the non-spinel γ-Al_2O_3 structure. All calculations were performed within the generalized gradient approximation (GGA) [14] using the Perdew-Burke-Ernzerhof (PBE) functional [15] for the exchange-correlation energy. Quantum Espresso simulation package [56] was used for the energy calculations and the core electrons were represented by ultrasoft-pseudo potentials [11]. All calculations were done with a 2x2x1 k-points mesh and Kohn-Sham orbitals were expanded with PWs up to a kinetic cutoff energy of 476 eV. .

The γ-Al_2O_3 (100) surface has four penta-coordinated Al surface atoms and, one tetra coordinated Al surface atom and five tri-coordinated O surface atoms and one tetra-coordinated O atom. In the convention employed in this work, Al atoms are labeled with numbers and O atoms with letters (Fig. 4.2). The surface Al(1)-Al(6), Al(2)-Al(7), Al(3)-Al(8) and Al(4)-Al(9) atoms are derived from six-coordinated bulk Al atoms in octahedral environments, while Al(5)-Al(10) are sub-surface atoms in tetrahedral coordination. Al(5)-Al(10) atoms are not directly used for the adsorptions since they are below the surface by about 1.58 Å and Al atoms are chosen as primary locations for adsorption of single atom on the γ-Al_2O_3 (100) surface.

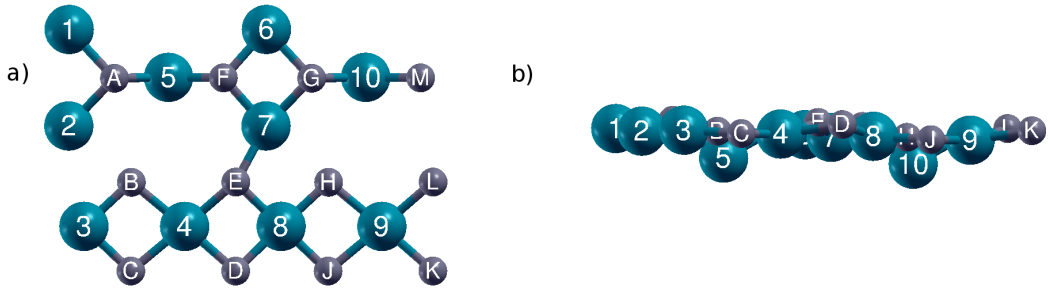

Figure 4.2: Fully Relaxed γ-Al_2O_3 (100) surface, (a) top (b) side views

The γ-Al_2O_3 (100) surface is relaxed fully for all the adsorption calculations with 12 Å vacuum. During the relaxation process, surface atoms exhibited displacements in the cell given in Table 4.2 in the x, y and z directions in percentage. Al(1), Al(2), Al(3) and O(A) atoms showed relatively large displacements in the x direction while Al(1), Al(2) and O(B) changed their coordination numbers. Al(1) and Al(2) atoms became tetra-coordinated and O(B) atom became tri-coordinated. These results are in agreement with the work of Deskins et al.[36]. They stated the same distortion of the surface after relaxation and the same changes in the coordination numbers of Al atoms after relaxation of the γ-Al_2O_3 (100) surface. In addition, the distance between the top and fourth layers diminishes after relaxation by about 1.55 % with respect to the bulk distance.

Table 4.1: Atomic Displacements (Å) of the relaxed γ-Al_2O_3 (100) surface (%)

Atom	x	y	z	Atom	x	y	z
Al(1)	-47.46	-0.56	-1.74	Al(6)	-4.72	-0.56	-1.74
Al(2)	-49.13	1.74	-1.78	Al(7)	-4.88	1.74	-1.79
Al(3)	13.02	-0.62	-1.51	Al(8)	1.37	-0.62	-1.51
Al(4)	5.21	-0.71	-1.78	Al(9)	1.98	-0.71	-1.79
Al(5)	-7.41	0.24	1.75	Al(10)	-2.80	0.24	1.75
O(A)	-18.92	0.21	-0.36	O(G)	-4.95	0.21	-0.36
O(B)	7.11	-1.94	0.64	O(H)	1.84	-1.94	0.64
O(C)	6.33	2.79	0.60	O(I)	1.64	2.79	0.61
O(D)	3.00	3.67	0.33	O(J)	1.40	3.67	0.33
O(E)	3.11	-1.47	0.29	O(K)	1.45	-1.47	0.29
O(F)	-3.45	0.33	-0.51	O(L)	-1.60	0.33	-0.51

As a further validation of our results, the surface energy of the γ-Al_2O_3(100) was calculated. For this work, the surface energy, E_{surf}, was defined as

$$E_{surf} = \frac{E_{slab} - (\frac{N_{slab}}{N_{bulk}})E_{bulk}}{2A} \tag{4.1}$$

where E_{slab} is the energy of the total slab, E_{bulk} is the energy of the bulk, N_{slab} and N_{bulk} are the number of the atoms in the slab and the bulk unit cell respectively. A is the surface area of the unit cell and the factor of 2 in the denominator accounts for two equivalent surfaces on either side of the slab. The surface energy of the γ-Al_2O_3(100) was found to be 1.03 J/m^2. This compares well to 0.97 J/m^2 quoted in [34]. In addition,the surface energy of an 8-layer (1x1) slab was calculated to examine the effect of the number of layers on surface energy. Following a full geometric optimization, the surface energy of the 8-layer slab was calculated 1.06 J/m^2 which agrees well with the 4-layer slab. Therefore, 4-layer and a (2x1) cell model was used for the rest of the calculations.

4.3 Single Atom Noble Metal Adsorption on the γ-Al_2O_3(100) Surface

One of the critical subjects in the study of NSR catalysis is noble metals as mentioned in the previous chapter. In this work, calculations with mono and bimetallic clusters were performed to investigate effects of the noble metal on the NO_2 adsorption on the γ-Al_2O_3(100) surface. The Pt and Rh atoms were chosen for calculations and their adsorption behaviours over the γ-Al_2O_3(100) surface and their effects on the NO_x adsorption were studied.

4.3.1 Adsorption of a Single Pt Atom on the γ-Al_2O_3(100) Surface

Although it is known that the Pt atom prefers to bind to O atoms rather than Al atoms [34], Ja Hun Kwak et al. claimed that the Pt atom interacts with the penta-coordinated Al atoms on the surface strongly [57]. Furthermore, it was reported that bridging configurations gave stronger adsorptions rather than the adsorptions above one atom [23]. Because of these reasons, in this work, a single Pt atom adsorption was investigated in the bridging configurations and embedded configurations. The adsorption energy was defined as

$$E_{ads} = E_{slab+Pt} - E_{slab} - E_{Pt} \tag{4.2}$$

where $E_{slab+Pt}$ is the energy of the slab with Pt adsorbed, E_{slab} is the energy of bare surface and E_{Pt} is the energy of Pt in the gas-phase.

Starting with the Al(1) atoms, the Pt atom was placed in two different bridge configurations (Pt-Al(1)-B1 and Pt-Al(1)-B2). In the Pt-Al(1)-B1 configuration, the Pt atom was bonded to Al(1), Al(2) and O(A) in the bridge configuration (Fig. 4.3). After relaxation, no considerable geometric changes on the surface was observed. The adsorption energy of the Pt atom for this configuration was calculated to be -2.02 eV and the average bond distance of the Pt atom was found to be 2.45 Å. In the Pt-Al(1)-B2 configuration, the Pt atom was bridged to Al(1) and O(A) atoms (Fig. 4.4). Relaxation caused the bond to break between Al(1) and O(A) atom and it was found that the Pt atom was more stable in this configuration since the adsorption energy was found to be -2.23 eV. For this configuration, the average bond distance of the Pt atom was 2.05 Å.

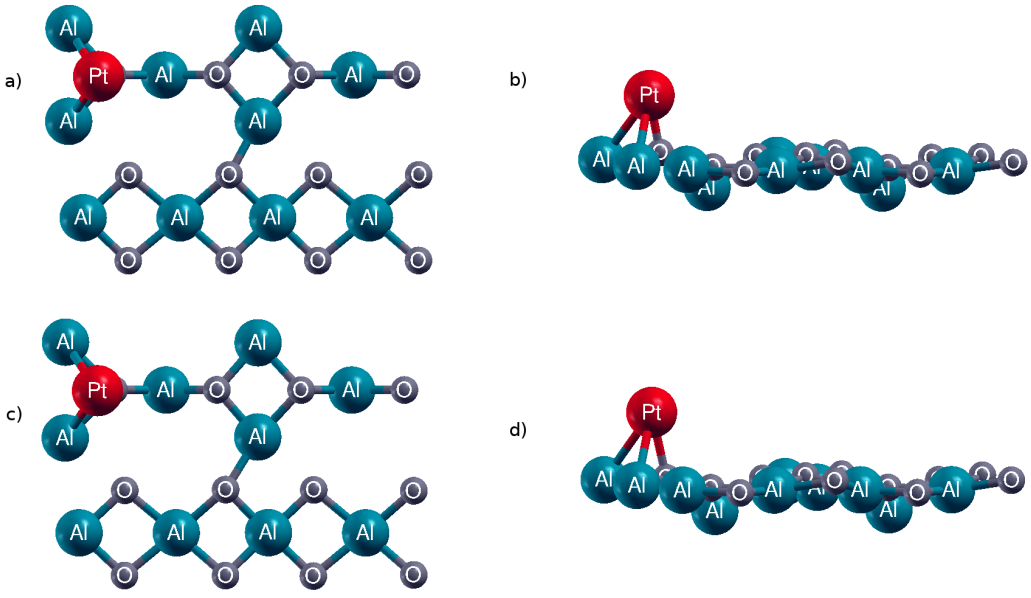

Figure 4.3: Adsorption of the Pt atom in the Al(1)-B1 configuration, (a) and (b) are the initial , (c) and (d) are the final top and side views

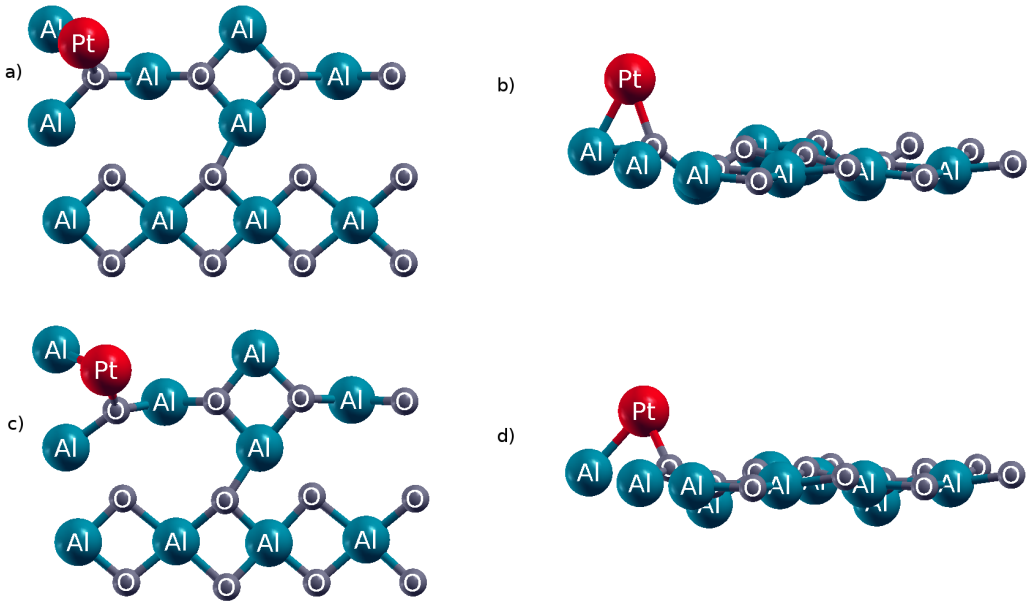

Figure 4.4: Adsorption of the Pt atom in the Al(1)-B2 configuration, (a) and (b) are the initial , (c) and (d) are the final top and side views

The Pt atom was investigated in bridging configuration, Pt-Al(2)-B, around of the Al(2) atom. For Pt-Al(2)-B configuration, Pt was bridged to the Al(2) and O(A) atoms. Unfortunately, this configuration failed to stabilize. However, a second configuration, Pt-Al(2)-E, inspired by Deskins et al. [23] where the Pt atom was embedded into the surface, was attempted. For the Pt-Al(2)-E configuration where the Pt atom was bonded to the Al(2), O(A) and O(B) atoms and placed close to the surface. After relaxation, Pt moved down into the surface and caused displacement of the surface Al(2), O(A) and O(B) atoms. The bond between Al(2) and O(A) was broken and O(B) atom moved out to the surface by about 1.2 Å (Fig.4.5). Therefore the Pt atom could be considered a part of the surface rather than adsorbed over the surface. Moreover, the Pt atom was stabilized in this configuration strongly, having an adsorption energy of -3.66 eV and the average bond distance of the Pt atom was found to be 2.16 Å.

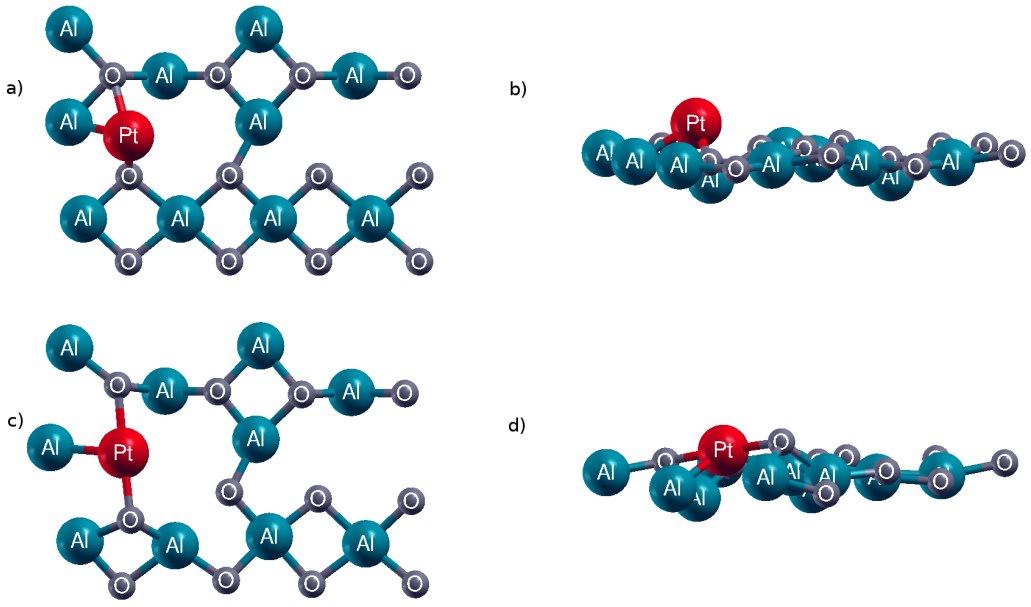

Figure 4.5: Adsorption of the Pt atom in the Al(2)-E configuration, (a) and (b) are the initial , (c) and (d) are the final top and side views

The bridge configurations on the Al(3)-O(B) and the Al(3)-O(C) atoms were the two possible configurations to bind the Pt atom over the surface but since the O(B) and the O(C) atoms were in a similar environment and possessing similar coordination, their interaction with the Pt atom was expected to be similar. Thus only one, the bridging configuration of the Pt over the Al(3) and the O(B) atoms, was taken into account. After relaxation, the Pt atom formed an additional bond with the Al(2) atom and became tri-coordinated (Fig. 4.6). The adsorption energy of this configuration was almost the same with the Pt-Al(1)-B1 configuration, -2.01 eV, and the average bond distance of the Pt atom was found to be 2.42 Å. In addition, another configuration in which the Pt atom placed over the Al(2) and Al(3) atoms in the bridge configuration, failed to stabilized. It could be concluded from this calculation that the Pt atom prefered a bridging configuration over the Al and O atoms rather than a bridging configuration over the Al atoms.

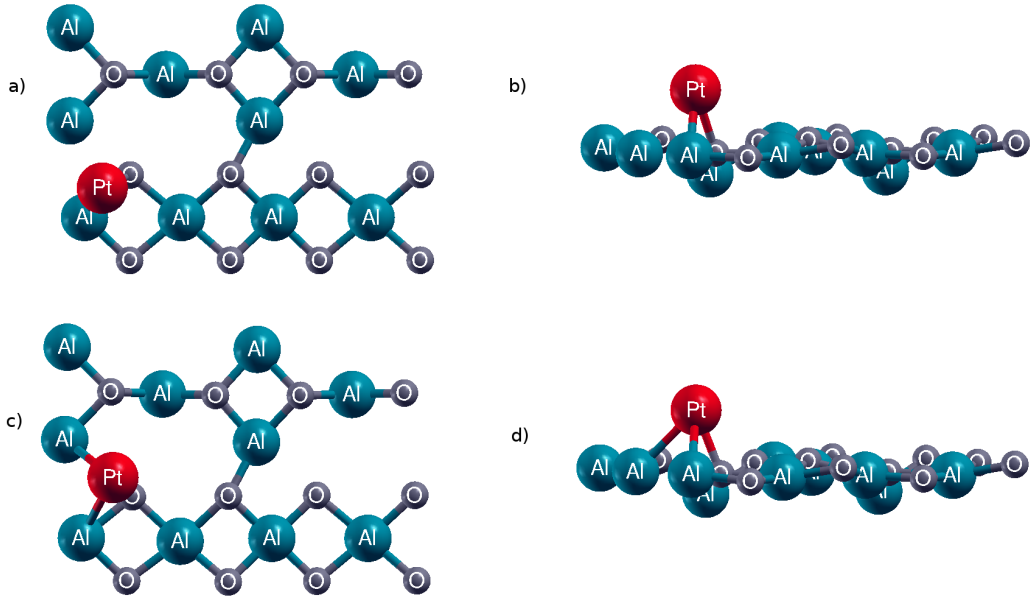

Figure 4.6: Adsorption of the Pt atom in Al(3)-B configuration,(a) and (b) are the initial , (c) and (d) are the final top and side views

Similar to the results of the Pt-Al(2)-B configuration, the bridging configuration of the Pt atom over the surface failed to stabilize around the Al(4) atom. However, two embedded configurations, the Pt-Al(4)-E1 and Pt-Al(4)-E2 configurations, were succesfully stabilized. The Pt-Al(4)-E1 configuration was mentioned in the work of Deskins et al. [23] but The Pt-Al(4)-E2 configuration was inspired from the Pt-Al(2)-B configuration. In the Pt-Al(4)-E1 configuration, the Pt atom was bonded to the Al(4), O(C) and O(D) and placed close to the surface. After relaxation, the bonds between Al(4)-O(C) atoms and Al(4)-O(D) atoms were broken and the O(D) atom moved out to the surface while the Pt atom moved into the surface. Once again, the Pt atom could be considered as a part of the surface for this configuration (Fig. 4.7). In addition, the Pt atom exhibited the most stable adsorption for this configuration. The adsorption energy of the Pt atom was found to be -3.87 eV which was in good agreement with the result of the work of Deskins et al. where the adsorption energy of the Pt atom was calculated to be -3.50 eV [23]. In addition, the bond distance between Pt and O(C) atoms was only 1.4 % longer than that in work of Deskins et al. The slight differences between this work and the work of Deskins et al. may be attributed to the use of different parameters. In spite of the differences, the bond distances between Pt-Al(4) and Pt-O(D) atoms had the same value of the work of Deskins et al. and they were found to be 2.32 Å and 2.03 Å respectively. Finally, the average bond distance of the Pt atom was calculated

as 2.14 Å. Likely the Pt-Al(4)-E1 type configuration, in the Pt-Al(4)-E2 type configuration the Pt atom was placed close to the surface bonded to the Al(4), O(B) and O(E) atoms. It was expected that this configuration would give almost the same results with the Pt-Al(4)-E1 configuration since both configurations had the same environments. The bonds between the Al(4) atom and O atoms were broken and the Pt atom moved into the surface while the O(E) atom moved towards to out to the surface (Fig. 4.8). Furthermore, the adsorption energy of this configuration, -3.76 eV, was close to the Pt-Al(4)-E1 configuration and the bond distances between the Pt atom and the nearest neighbour surface atoms bonded to the Pt atom were the same with the Pt-Al(4)-E1 configuration. The Pt-Al(4) and Pt-O(D) distances were 2.32 Å and 2.03 Å respectively and the average bond distance of the Pt atom was found to be 2.14 Å.

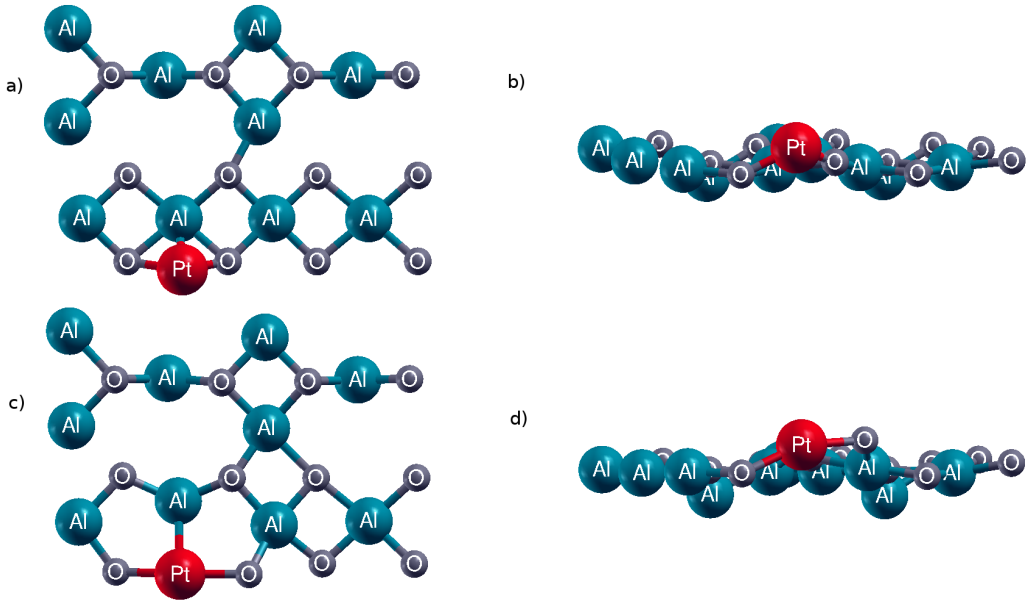

Figure 4.7: Adsorption of the Pt atom in the Al(4)-E1 configuration,(a) and (b) are the initial , (c) and (d) are the final top and side views

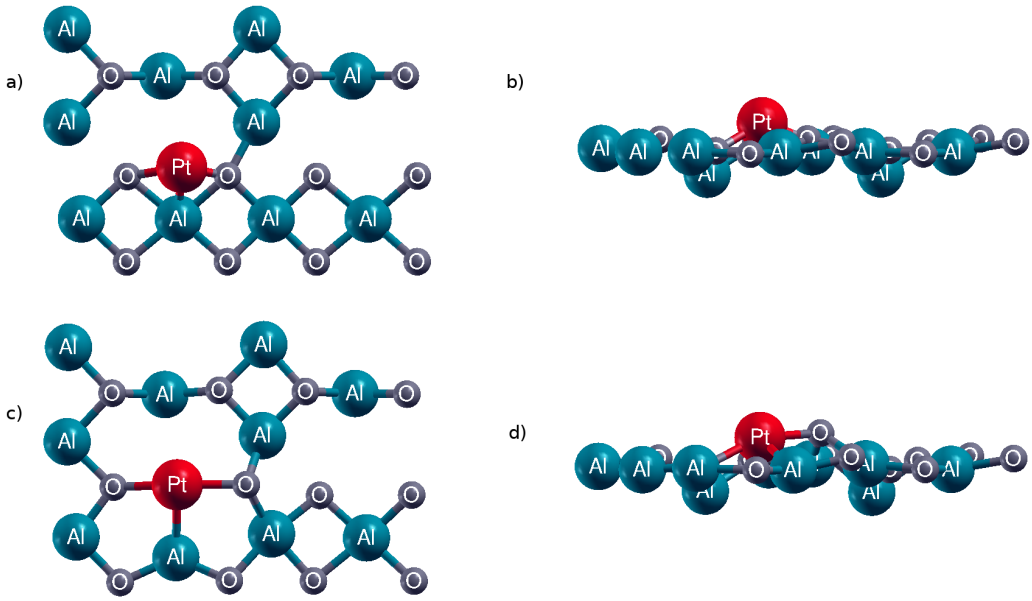

Figure 4.8: Adsorption of the Pt atom in the Al(4)-E2 configuration,(a) and (b) are the initial , (c) and (d) are the final top and side views

In Table 4.2, the final geometries of the relaxed configurations, adsorption energies of the Pt atom and the bond distances are given.

Table 4.2: The final geometries, the adsorption energies and the bond distances (Å) of the relaxed Pt/γ-Al_2O_3(100) configurations

Configuration	Description	E_{ads}	Pt-Al	Pt-O
Pt-Al(1)-B1	Bridged to Al(1), Al(2) and O(A)	-2.02	Pt-Al(1) 2.68 Pt-Al(2) 2.67	Pt-O(A) 2.00
Pt-Al(1)-B2	Bridged to Al(1) and O(A) atoms	-2.23	Pt-Al(1) 2.41	Pt-O(A) 2.00
Pt-Al(2)-E	In-surface	-3.66	Pt-Al(2) 2.39	Pt-O(A) 2.06 Pt-O(B) 2.02
Pt-Al(3)-B	Bridged to Al(2), Al(3) and the O(B)	-2.01	Pt-Al(2) 2.60 Pt-Al(3) 2.65	Pt-O(B) 2.02
Pt-Al(4)-E1	In-surface	-3.87	Pt-Al(4) 2.32	Pt-O(C) 2.06 Pt-O(D) 2.03
Pt-Al(4)-E2	In-surface	-3.76	Pt-Al(4) 2.32	Pt-O(B) 2.06 Pt-O(E) 2.03

4.3.2 Adsorption of a Single Rh Atom on the γ-Al_2O_3(100) Surface

Although the Rh atom has not been studied as frequently as the Pt atom with DFT method, Rh is one of the promising candidates for the redox component of the NSR catalyst as men-

tioned in the previous chapter. To investigate the behaviour of the single Rh atom on the γ-Al_2O_3(100) surface, we followed bridging and embedded configurations similar to the configurations of the adsorption of single Pt atom. Similar to the previous part, the adsorption energy of the Rh atom was defined as

$$E_{ads} = E_{slab+Rh} - E_{slab} - E_{Rh} \tag{4.3}$$

where $E_{slab+Rh}$ is the energy of the slab with Rh adsorbed, E_{slab} is the energy of bare surface and E_{Rh} is the energy of Rh in the gas-phase.

Using the same name convention, the Rh atom was first placed on the γ-Al_2O_3(100) surface in bridging configurations, Rh-Al(1)-B1 and Rh-Al(1)-B2. In the Rh-Al(1)-B1 configuration, the Rh atom was bridged to Al(1), Al(2) and the O(A) atoms (Fig. 4.9). For this configuration, the Rh atom did not break any bonds and exhibit any important dislocation. The adsorption energy of the Rh atom was found to be -1.68 eV which was less than the adsorption energy of the Pt atom in the same environment (Pt-Al(1)-B1). The average bond distance of the Rh atom was 2.35 Å and it was also less than the average bond distance of the Pt atom in the Pt-Al(1)-B1 configuration. For Rh-Al(1)-B2 configuration, the Rh atom placed over Al(1) and O(A) atoms in the bridging configuration (Fig. 4.10). This configuration gave unexpected results. After relaxation, the bond between the Rh atom and the subsurface Al(5) atom formed and therefore the Al(5) atom changed into five-coordinated from tetra-coordinated. Unlike the Pt atom, the Rh atom moved into the surface then the Rh atom nearly became a part of the surface. The adsorption of the Rh atom on the surface was more stable than the Rh-Al(1)-B1 configuration since the adsorption energy was found to be -2.64 eV, which was much higher than the Rh-Al(1)-B1 configuration of by -0.96 eV. The average bond distance of the Rh atom for this configuration was calculated to be 2.36 Å.

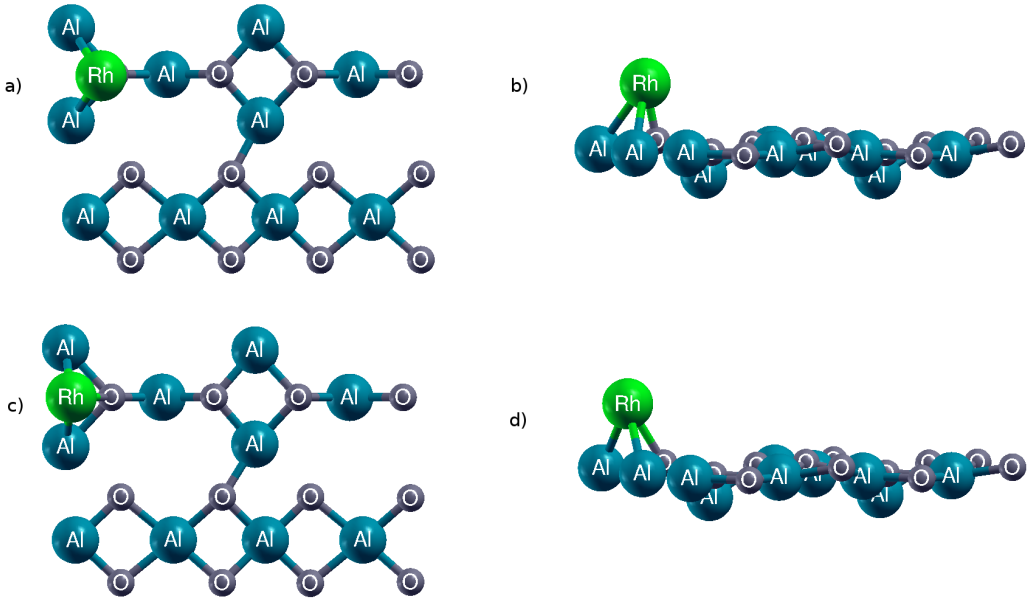

Figure 4.9: Adsorption of the Rh atom in the Al(1)-B1 configuration, (a) and (b) are the initial , (c) and (d) are the final top and side views

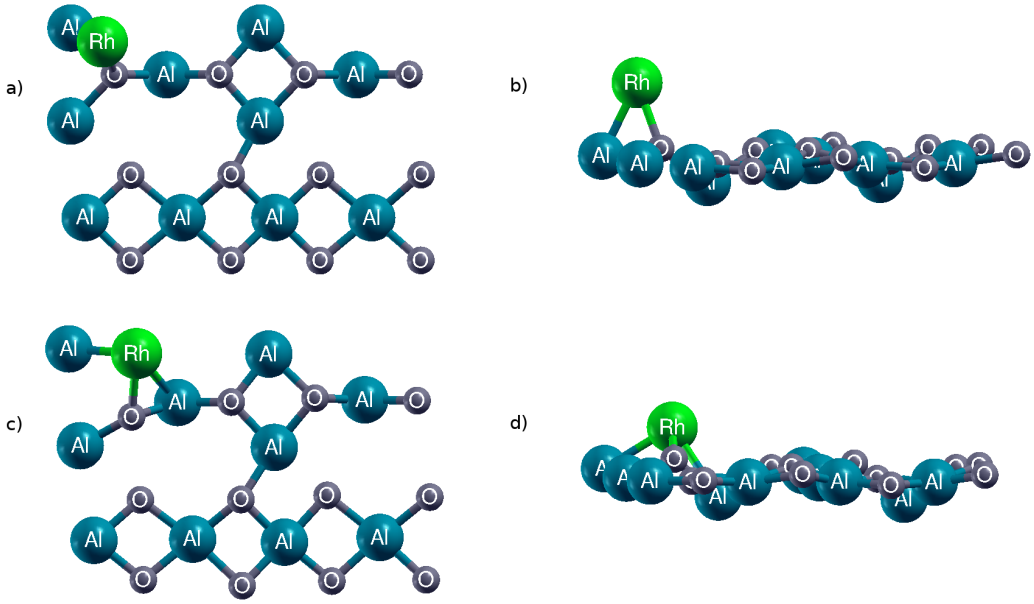

Figure 4.10: Adsorption of the Rh atom in the Al(1)-B2 configuration, (a) and (b) are the initial , (c) and (d) are the final top and side views

The Rh atom was placed both in a bridging, the Rh-Al(2)-B configuration, and an embedded, the Rh-Al(2)-E configuration, configurations anchored to the Al(2) atom. The Rh atom was placed in the bridging over Al(2) and O(A) atoms and close to the surface bound to Al(2), O(A) and O(B) atoms for the Rh-Al(2)-B and Rh-Al(2)-E configurations respectively. Although these initial configurations were different at the begining of the calculations, the same final geometries were obtained after calculations. During the calculation of the bridging type Rh-Al(2)-B configuration, the Rh atom exhibited a tendency to be a part of the surface and it moved down into the surface and finally embedded into the surface (Fig. 4.11). It was also observed that the Rh atom embedded into the surface in the Rh-Al(2)-E configuration as shown in Fig. 4.12. The distinguishable difference between the Pt-Al(2) and Rh-Al(2) configuration was an additional bond of the Rh atom with the subsurface Al(5) atom. The adsorption energies of the Rh-Al(2) configurations were found to be -2.66 eV for both configurations and they were lower than the adsorption energy of the Pt atom in the same environment. The decreasing in the adsorption energy of the Rh atom might be caused by the additional bond of the Rh atom with the Al(5) atom. The average bond distances of the Rh atom for both configurations were also found to be the same, 2.28 Å.

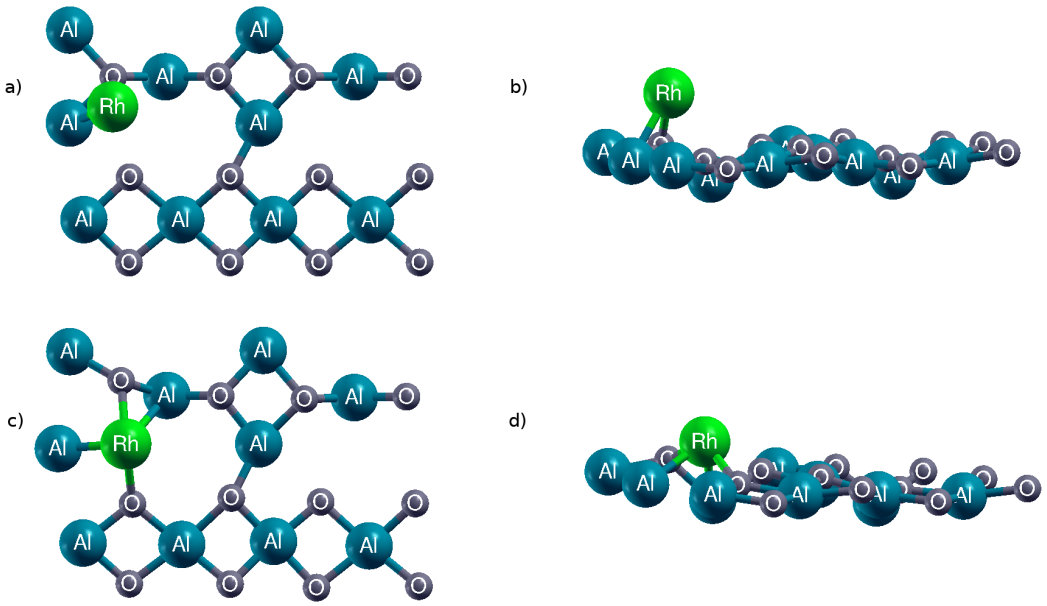

Figure 4.11: Adsorption of the Rh atom in the Al(2)-B configuration, (a) and (b) are the initial , (c) and (d) are the final top and side views

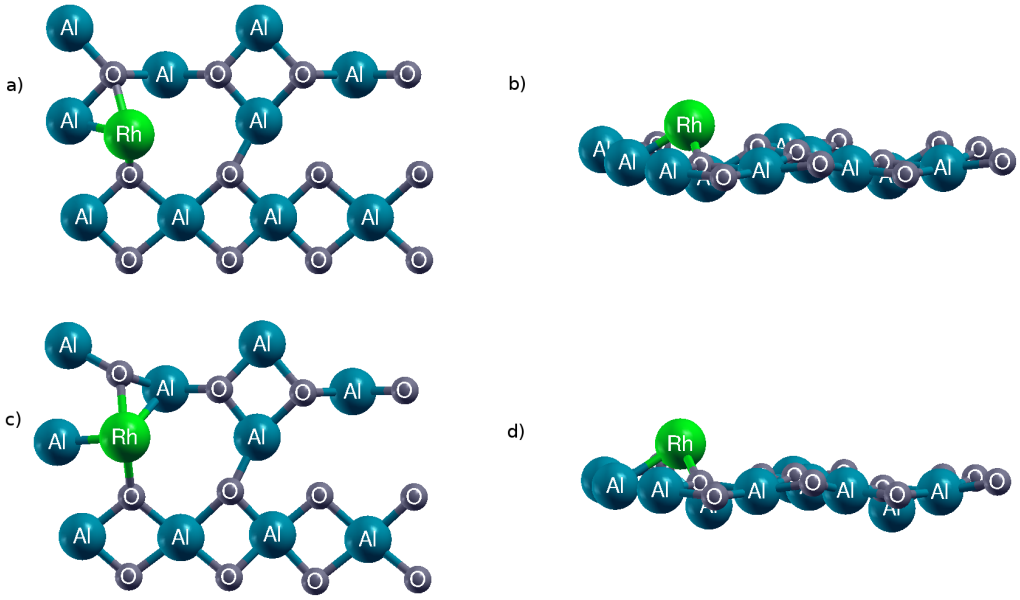

Figure 4.12: Adsorption of the Rh atom in the Al(2)-E configuration, (a) and (b) are the initial , (c) and (d) are the final top and side views

For the adsorption of the Rh atom anchored to the Al(3) atom, the same initial configuration of the Pt-Al(3)-B configuration was used. The Rh atom was bridged to the Al(3) and the O(B) atom (Rh-Al(3)-B). After relaxation, unlike the Pt atom, the bond between the Rh atom and O(B) atom was broken and a bond between the Rh atom and the Al(2) atom was formed (Fig. 4.13). The adsorption energy of this configuration was found to be -3.40 eV which was considerably higher than the Pt-Al(3)-B configuration. This adsorption energy was close to the embedded configurations of the Rh and the Pt atom on the surface and it was the highest value among all the studied bridging configurations. This difference possibly indicates a stronger bond between Al and the metal atom as compared the Al-O bond. The average bond distance of the Rh atom was calculated to be 2.42 Å.

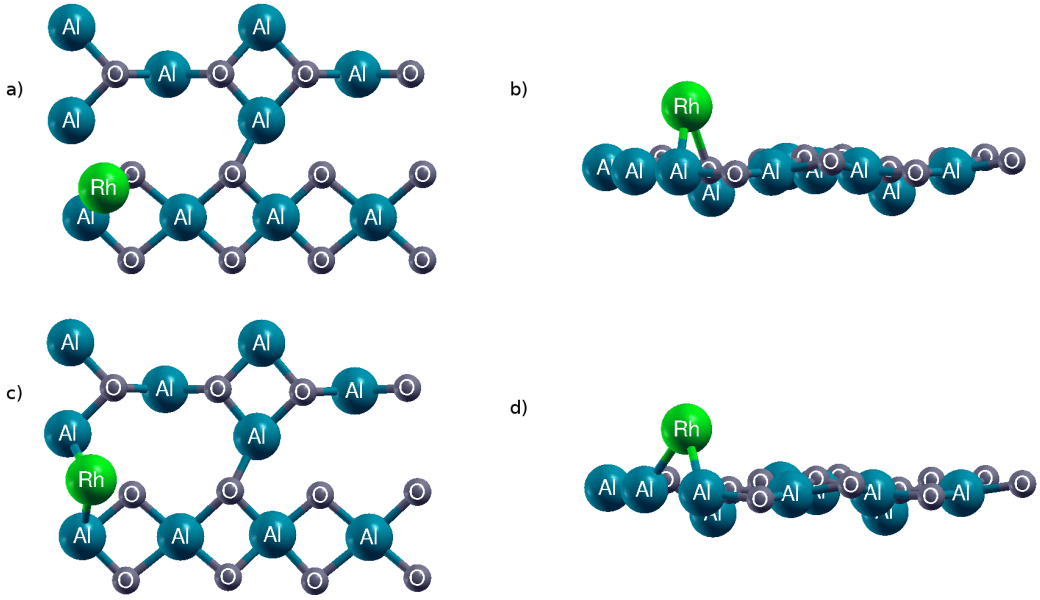

Figure 4.13: Adsorption of the Rh atom in the Al(3)-B configuration, (a) and (b) are the initial , (c) and (d) are the final top and side views

The Rh atom was adsorbed on the Al(4) atom in both the bridging and embedded configurations. In the Rh-Al(4)-B configuration, the Rh atom was placed on the Al(4) atom and the O(B) atoms. After relaxation, the Rh atom moved into the surface and bonded to the O(E) atom (Fig. 4.14). The O(E) atom was distorted and moved out of the surface by about 0.5 Å. The adsorption energy of this configuration was found to be -3.40 eV and the average bond distance of the Rh atom was calculated to be 2.14 Å. Since the Rh-Al(4)-B configuration became an embedded configuration, the embedded configuration of the same region was not attempted. The Rh-Al(4)-E configuration had the same geometry with the Pt-Al(4)-E1 configuration, however, this configuration failed to stabilize in this environment. Because of the bridging configuration became an embedded configuration and there was no embedded configuration obtained on the Al(4) atom except the Rh-Al(4)-B configuration, the only stable configuration Rh-Al(4)-B was named as Rh-Al(4)-E for in Table 4.3 and the following sections.

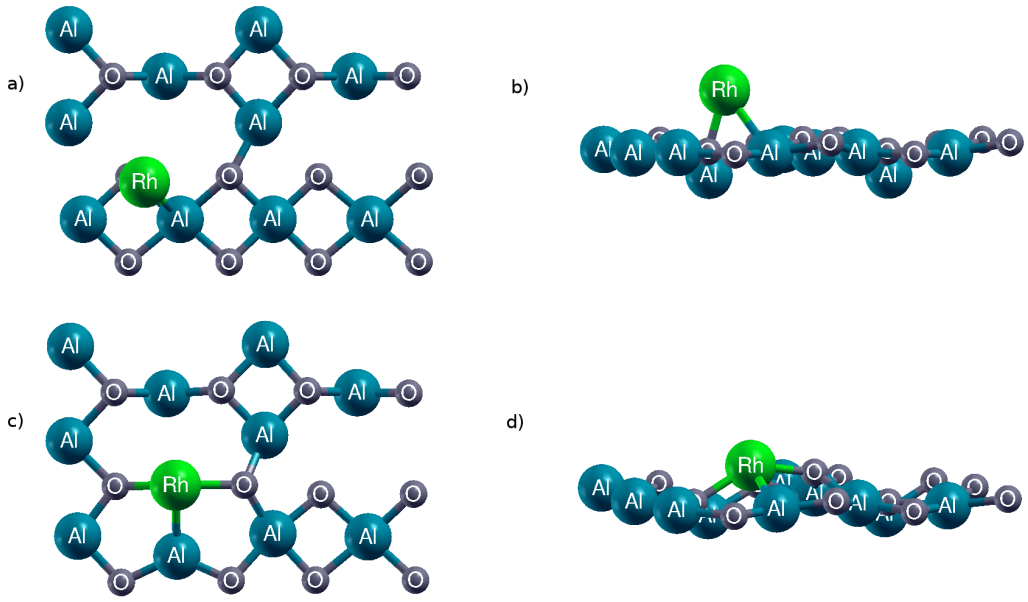

Figure 4.14: Adsorption of the Rh atom in the Al(4)-E configuration, (a) and (b) are the initial , (c) and (d) are the final top and side views

In Table 4.3, the final geometries, adsorption energies of the Rh atom and the bond distances of the relaxed Rh/γ-Al_2O_3(100) configurations are given.

Table 4.3: The final geometries, the adsorption energies and the bond distances (Å) of the relaxed Rh/γ-Al_2O_3(100) configurations

Configuration (Rh)	Description	E_{ads}	Rh-Al		Rh-O	
Rh-Al(1)-B1	Bridged to Al(1), Al(2) and O(A)	-1.68	Rh-Al(1) Rh-Al(2)	2.46 2.46	Rh-O(A)	2.13
Rh-Al(1)-B2	Bridged to Al(1), Al(5) and O(A)	-2.64	Rh-Al(1) Rh-Al(5)	2.41 2.71	Rh-O(A)	2.03
Rh-Al(2)-B	In-surface	-2.66	Rh-Al(2) Rh-Al(5)	2.34 2.70	Rh-O(A) Rh-O(B)	2.03 2.05
Rh-Al(2)-E	In-surface	-2.66	Rh-Al(2) Rh-Al(5)	2.34 2.70	Rh-O(A) Rh-O(B)	2.03 2.05
Rh-Al(3)-B	Bridged to Al(2) and Al(3)	-3.40	Rh-Al(2) Rh-Al(3)	2.39 2.44	-	
Rh-Al(4)-E	In-surface	-3.40	Rh-Al(4)	2.31	Rh-O(B) Rh-O(E)	2.06 2.04

4.4 Adsorption of the Diatomic Clusters on the γ-Al_2O_3(100) Surface

In this section, three types of diatomic clusters, 2Pt, 2Rh and Pt+Rh, were considered to examine the behaviour of diatomic clusters for NO_2 adsorption on the γ-Al_2O_3(100) surface.

All calculations were performed adding the second precious metal atom on the single metal atom systems explained in previous part and all the configurations were relaxed fully. The adsorption energies were defined like previous part

$$E_{ads} = E_{slab+metals} - E_{slab+metal} - E_{metal} \tag{4.4}$$

where $E_{slab+metals}$ is the energy of the slab with the adsorbed diatomic clusters, $E_{slab+metal}$ is the slab with the adsorbed a single metal and E_{metal} is the energy of metal in the gas-phase.

4.4.1 Adsorption of 2 Pt Atoms on the γ-Al_2O_3(100) Surface

The second Pt atom was added to the final configurations of the described in the section 4.3.1. The second Pt on the Pt-Al(1)-B1 configuration was obtained by replacing the second Pt atom bridged to O(A) and previously adsorbed Pt atom (2Pt-Al(1)-B1). After relaxation, a bond between the Al(2) atom and the second Pt atom was formed and the bonds of the previosly adsorbed Pt atom with Al(1) and Al(2) atoms were broken (Fig. 4.15). The adsorption energy of the second Pt atom for this configuration was found to be -3.44 eV and the average bond distance of the secondly adsorbed Pt atom was calculated to be 2.35 Å. Next calculation was based on the Pt-Al(1)-B2 configuration. The second Pt atom was placed on the Al(2) atom (2Pt-Al(1)-B2). Unlike the 2Pt-Al(1)-B1 configuration, none of the bonds were broken or formed. The second Pt atom moved out of the surface; on the contrary, the previously adsorbed Pt moved into the surface slightly (Fig. 4.16). The adsorption energy was very close to the preceding one, -3.45 eV, and the average bond distance of the second Pt atom was found to be 2.53 Å.

For the second Pt adsorption on the Pt-Al(2)-E configuration, there were two possible different configurations, 2Pt-Al(2)-E(1) and 2Pt-Al(2)-E(2). These two configurations had similar environment and they gave the same results as expected. The second Pt atom was placed on Al(7) and O(E) atoms and it had a bond with the previously adsorbed Pt atom in the 2Pt-Al(2)-E(1) configuration. For the 2Pt-Al(2)-E(2) configuration, Pt was located on the Al(7) and O(F) atoms and it bonded to the previously adsorbed Pt atom. After relaxation, the bond

between the Pt atoms was broken for both configurations (Fig. 4.17 and Fig. 4.18). The Pt atoms separated from each other on the surface and they kept the remaining bonds. As a results, there were two single Pt atoms on the surface, one of them part of the surface and the other one in a bridging configuration. Although both configurations had similar environment, the adsorption energies of the configurations were different, with -2.35 eV for 2Pt-Al(2)-E(1) and -1.95 eV for 2Pt-Al(2)-E(2) configurations respectively. The average bond distance of the secondly adsorbed Pt atom was 2.25 Å for 2Pt-Al(2)-E(1) configuration and 2.31 Å for 2Pt-Al(2)-E(2) configuration. These two configuration were not be used for the adsorption of the NO_2 molecule on the surface because of separation of the Pt atoms on the surface.

Based on the single Pt atom adsorption to the Al(3) atom, the second Pt atom was located with two different configurations (2Pt-Al(3)-B(1) and 2Pt-Al(3)-B(2)). For the first configuration, the second Pt atom was placed on the O(E) atom and bonded to the previosly adsorbed Pt atom (Fig. 4.19). After relaxation, a bond between the second Pt atom and the Al(4) atom was formed whereas the bond between the previously adsorded Pt atom and the Al(2) atom was broken. A bond between the Al(2) and O(B) which was slightly less than the same bond in bulk by 0.06 Å was formed and thus the Al(2) atom changed its coordination number from tetra-coordination to penta-coordination. The adsorption energy of the second Pt atom was considerable higher than the other configurations, -4.03 eV, and the average bond distance was calculated to be 2.30 Å. In the 2Pt-Al(3)-B(2) configurations, the second Pt atom was located in the same region. It was bonded to the Al(4) atom rather than the O(E) atom (Fig. 4.20). Although, the former configuration had the same Pt-Al bond, the final geometry of this configuration was completely different than the previous one. The second Pt atom bonded to the Al(3) atom and the previously adsorbed atom moved into the surface forced by the second Pt atom reaching a geometry similar to the final geometry of the Pt-Al(2)-E configuration. In addition, the final position of the Al(2) atom was lower about 0.7 Å than surface level. The most important point of this configuration was that this configuration exhibited the most stabilized second Pt adsorption, with -4.65 eV, among all the configurations of diatomic clusters. The average bond distance of the second adsorbed Pt atom was found to be 2.55 Å.

Finally, the second Pt atom was added to the Pt-Al(4)-E1 and Pt-Al(4)-E2 configurations. In the 2Pt-Al(4)-E1 configuration, the second Pt atom was placed on the Al(4) atom so as to bind the adsorbed Pt atom. At the end of the calculation, a bond between the second Pt atom and

the Al(3) atom formed and the previously adsorbed atom did not exhibit significant changes as seen in figure 4.21. The adsorption energy, -2.21 eV, was relatively lower than the other configurations. The average bond distance of the second Pt atom was found to be 2.55 Å. To add the second Pt atom on the Pt-Al(4)-E2 configurations, two different initial geometries were considered (2Pt-Al(4)-E2(1) and 2Pt-Al(4)-E2(2)). Although two initial geometry were different, the final geometries and the adsorption energies of the second Pt atom were the same for both configurations (Fig. 4.22 and Fig. 4.23). For the 2Pt-Al(4)-E1(1) configuration, the second Pt atom was located on the O(F) atom bonded to the adsorbed Pt atom. In the 2Pt-Al(4)-E2(2) configuration, the second Pt atom was located on the O(A) atom bonded to the adsorbed Pt atom. The second Pt atom in the 2Pt-Al(4)-E2(1) configuration located in the bridging geometry which was the same as the final geometry of the second Pt atom in the 2Pt-Al(4)-E2(2). The adsorption energy of the second Pt atom in this configuration was close to the 2Pt-Al(4)-E1 configuration, with -2.73 eV. Finally, the average bond distance of the second Pt atom was calculated to be 2.44 Å.

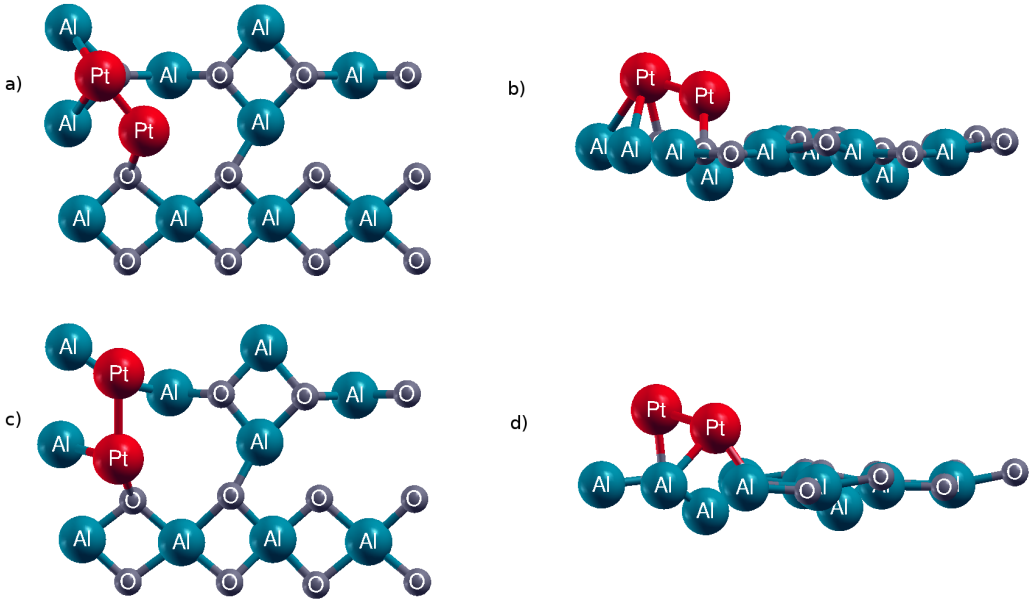

Figure 4.15: Adsorption of the second Pt atom adsorption in the 2Pt-Al(1)-B1 configuration, (a) and (b) are the initial , (c) and (d) are the final top and side views

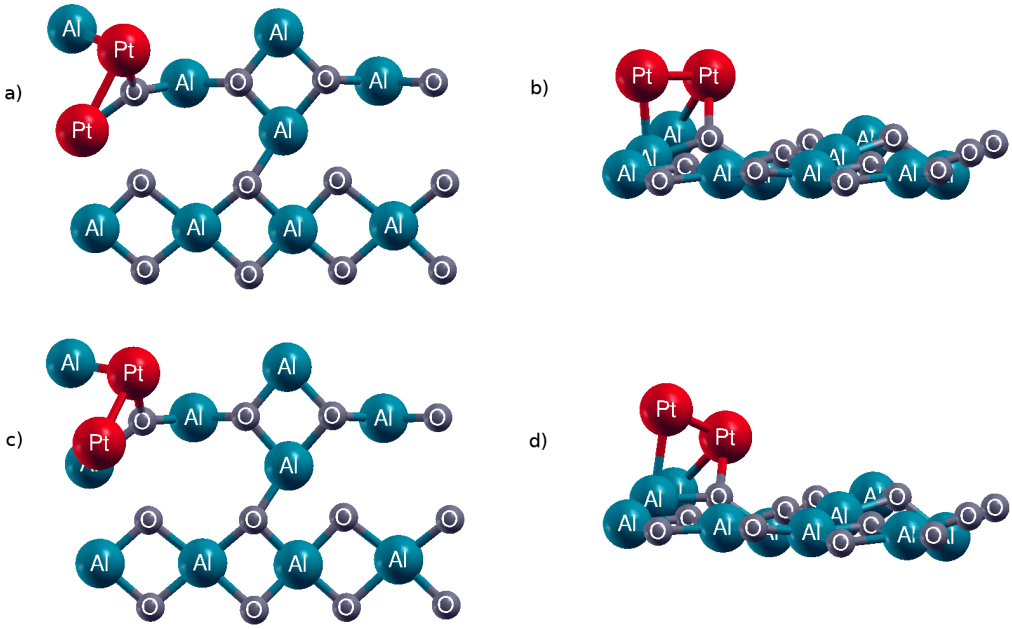

Figure 4.16: Adsorption of the second Pt atom adsorption in the 2Pt-Al(1)-B2 configuration, (a) and (b) are the initial , (c) and (d) are the final top and side views

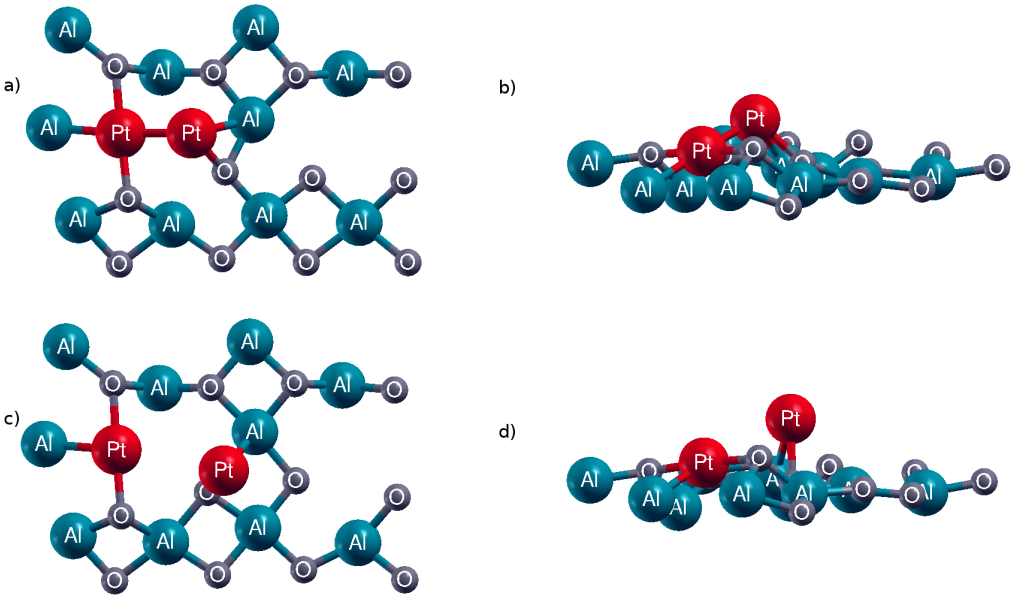

Figure 4.17: Adsorption of the second Pt atom adsorption in the 2Pt-Al(2)-E(1) configuration, (a) and (b) are the initial , (c) and (d) are the final top and side views

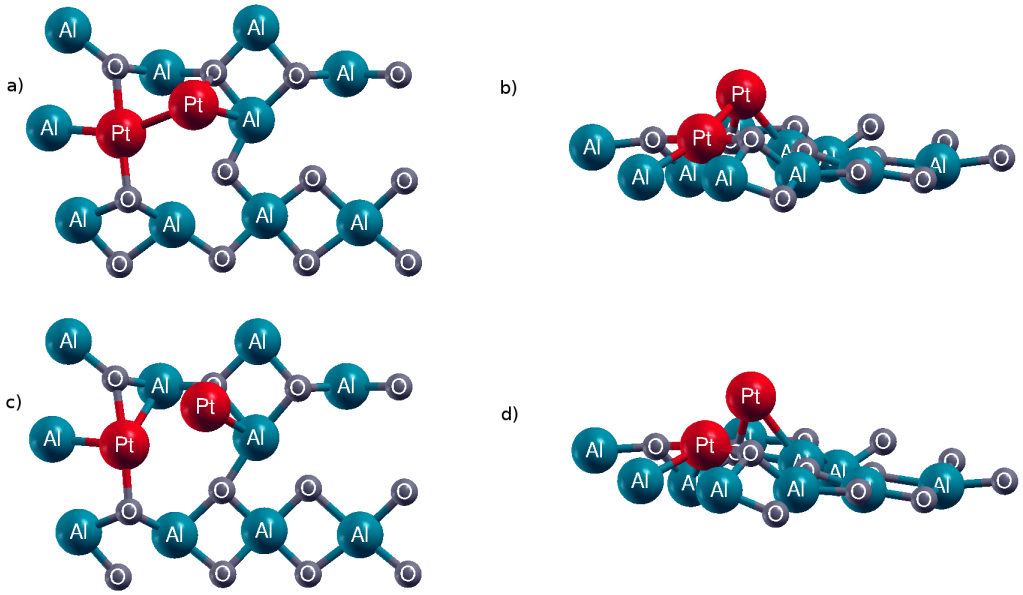

Figure 4.18: Adsorption of the second Pt atom adsorption in the 2Pt-Al(2)-E(2) configuration, (a) and (b) are the initial , (c) and (d) are the final top and side views

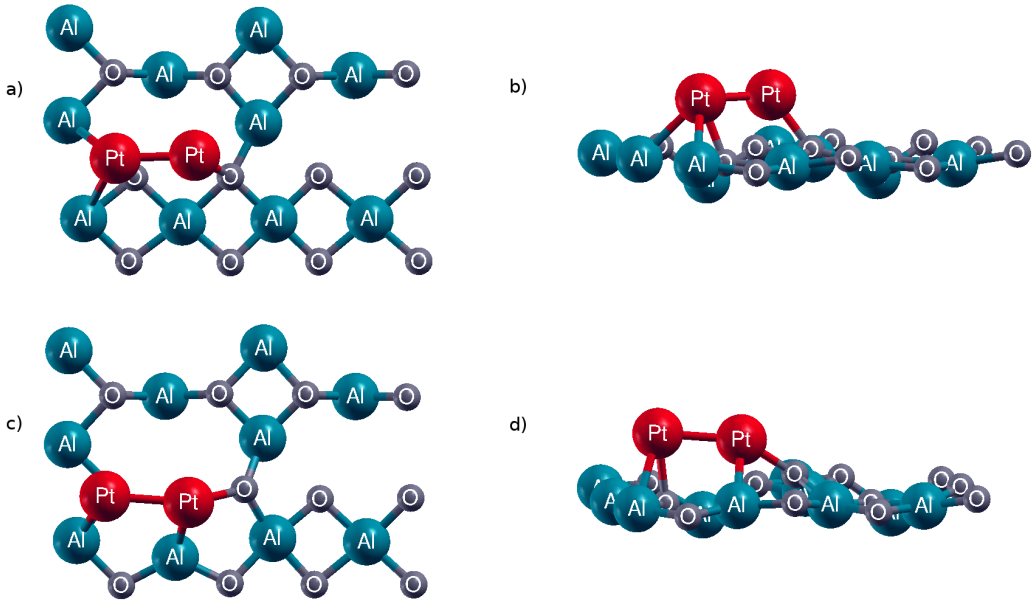

Figure 4.19: Adsorption of the second Pt atom adsorption in the 2Pt-Al(3)-B(1) configuration, (a) and (b) are the initial , (c) and (d) are the final top and side views

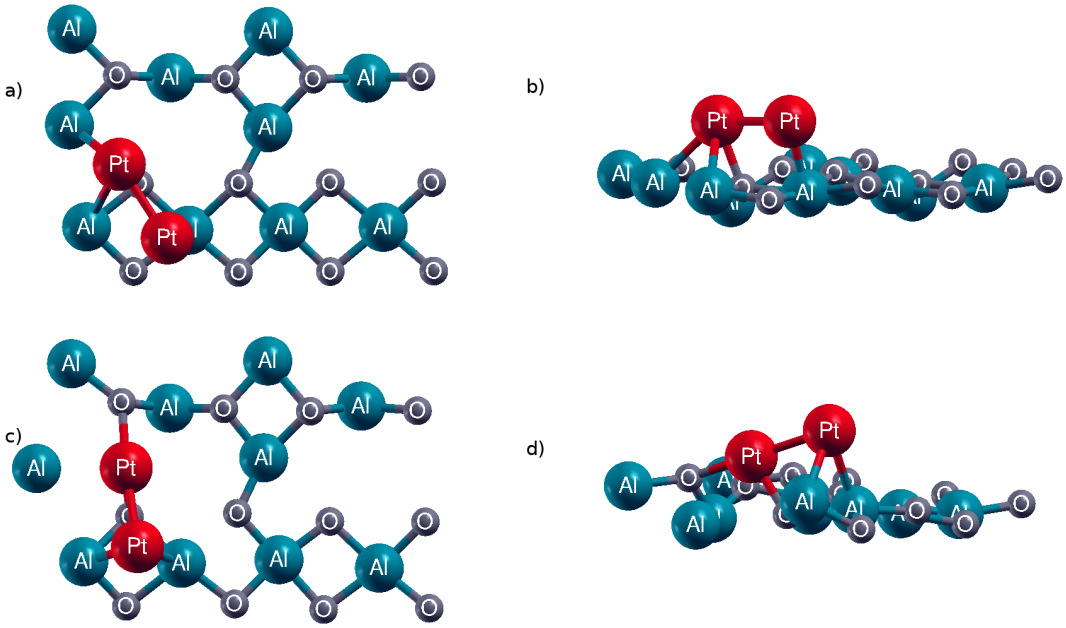

Figure 4.20: Adsorption of the second Pt atom adsorption in the 2Pt-Al(3)-B(2) configuration, (a) and (b) are the initial , (c) and (d) are the final top and side views

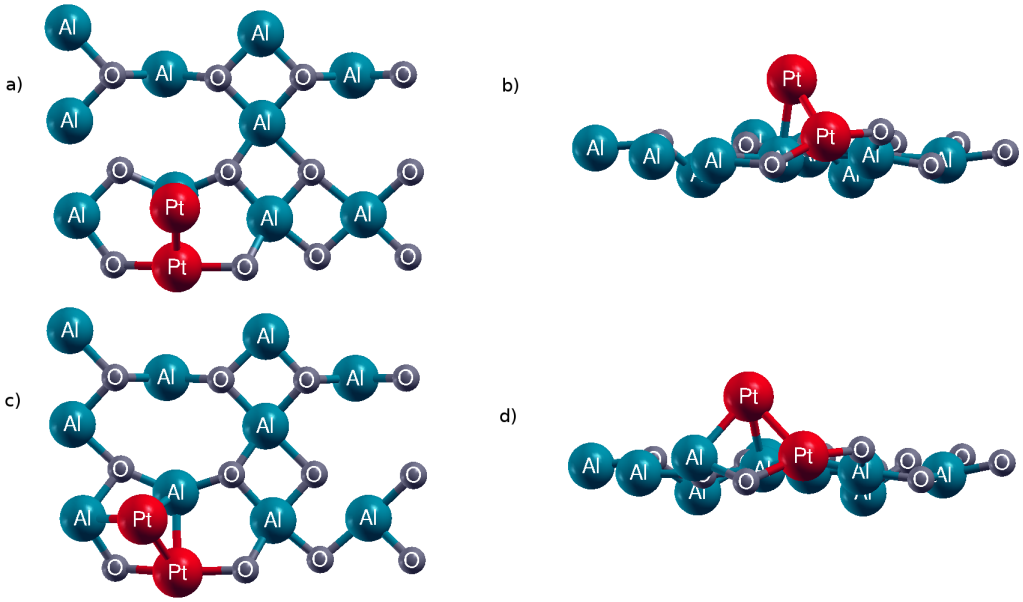

Figure 4.21: Adsorption of the second Pt atom adsorption in the 2Pt-Al(4)-E1 configuration, (a) and (b) are the initial , (c) and (d) are the final top and side views

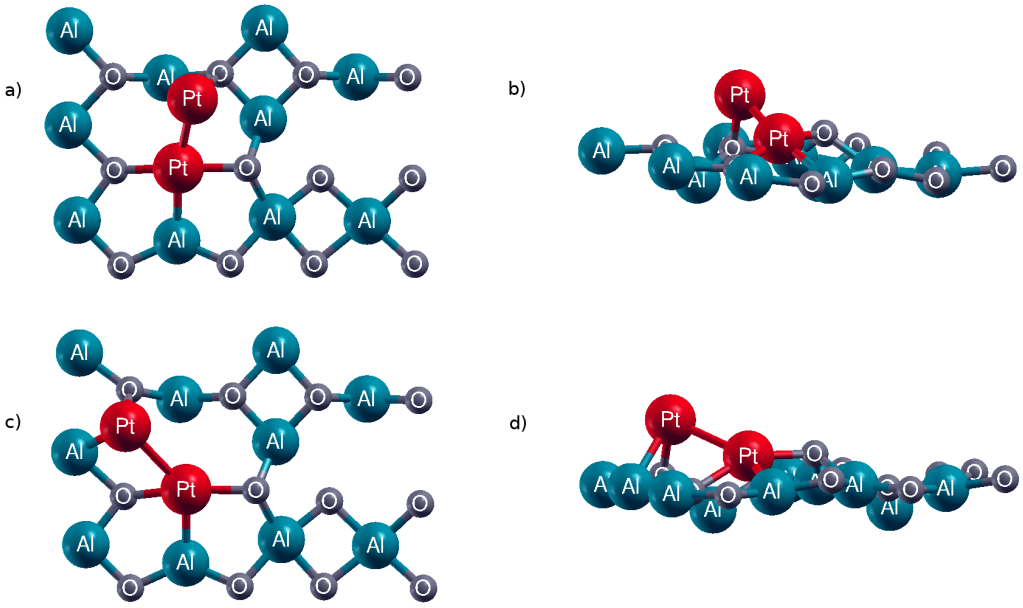

Figure 4.22: Adsorption of the second Pt atom adsorption in the 2Pt-Al(4)-E2(1) configuration, (a) and (b) are the initial , (c) and (d) are the final top and side views

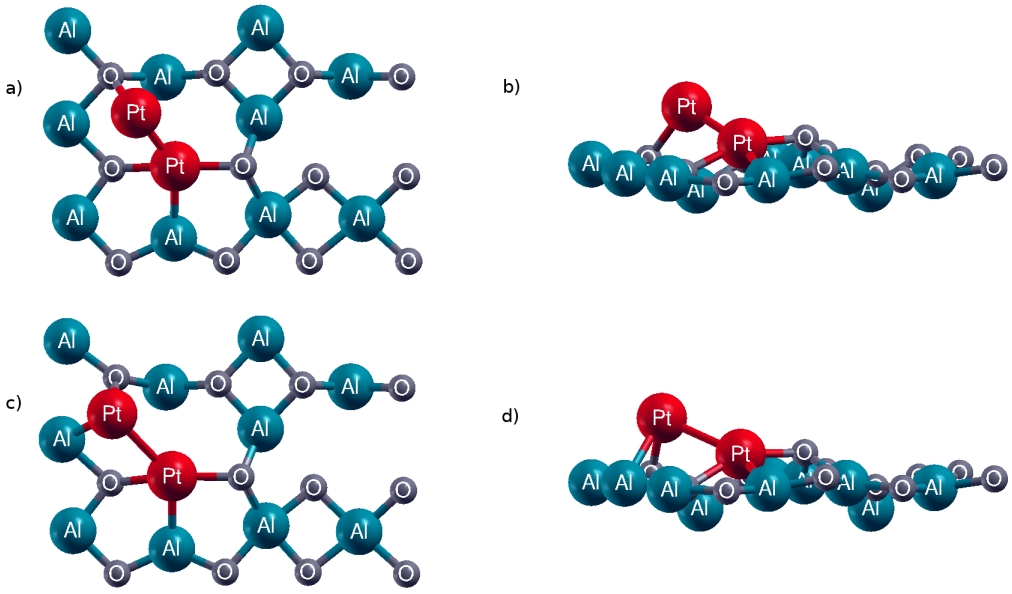

Figure 4.23: Adsorption of the second Pt atom adsorption in the 2Pt-Al(4)-E2(2) configuration, (a) and (b) are the initial , (c) and (d) are the final top and side views

In Table 4.4 and table 4.5, the final geometries, adsorption energies of the second Pt atom and the bond distances of the relaxed 2Pt/γ-Al_2O_3(100) configurations are given.

Table 4.4: The final geometries and adsorption energies of the relaxed 2Pt/γ-Al_2O_3(100) configurations

Configuration	Description	E_{ads}
2Pt-Al(1)-B1	Bridged to Al(2), O(B) and Pt	-3.44
2Pt-Al(1)-B2	Bridged to Al(2) and Pt	-3.45
2Pt-Al(2)-E(1)	Bridged to Al(7) and O(E)	-2.35
2Pt-Al(2)-E(2)	Bridged to Al(7) and O(F)	-1.95
2Pt-Al(3)-B(1)	Bridged to Al(4),O(E) and Pt	-4.03
2Pt-Al(3)-B(2)	Bridged to Al(3), Al(4) and Pt	-4.65
2Pt-Al(4)-E1	Bridged to Al(3), Al(4) and Pt	-2.21
2Pt-Al(4)-E2(1)	Bridged to Al(2), O(A) and Pt	-2.73
2Pt-Al(4)-E2(2)	Bridged to Al(2), O(A) and Pt	-2.73

Table 4.5: The bond distances (Å) of the relaxed 2Pt/γ-Al_2O_3(100) configurations

Configuration	Pt-Al	Pt-O	Pt-Pt
2Pt-Al(1)-B1	Pt-Al(2) 2.40	Pt-O(B) 2.09	2.55
2Pt-Al(1)-B2	Pt-Al(2) 2.56	-	2.49
2Pt-Al(2)-E(1)	Pt-Al(7) 2.50	Pt-O(E) 2.00	-
2Pt-Al(2)-E(2)	Pt-Al(7) 2.58	Pt-O(F) 2.05	-
2Pt-Al(3)-B(1)	Pt-Al(4) 2.39	Pt-O(E) 2.03	2.48
2Pt-Al(3)-B(2)	Pt-Al(3) 2.60 Pt-Al(4) 2.51	-	2.54
2Pt-Al(4)-E1	Pt-Al(3) 2.57 Pt-Al(4) 2.54	-	2.53
2Pt-Al(4)-E2(1)	Pt-Al(2) 2.53	Pt-O(A) 2.03	2.76
2Pt-Al(4)-E2(2)	Pt-Al(2) 2.53	Pt-O(A) 2.03	2.76

4.4.2 Adsorption of 2 Rh Atoms on the γ-Al_2O_3(100) Surface

Similar to the previous part, the second Rh atom was added on the single Rh atom configurations. Following the same method, the single Rh atom on the Al(1) atom was the starting point to arrange the configurations of the adsorption of the second Rh atom around of the Al(1) atom. There were three configurations, one of them derived from the Rh-Al(1)-B1 configuration and others derived from the Rh-Al(1)-B2 configuration. To begin with the Rh-Al(1)-B1 configuration (Fig. 4.24), the second Rh atom was bridged to Al(2) and O(A) atom forming a bond with the adsorbed Rh atom on the surface (2Rh-Al(1)-B1). After relaxation, the bonds between the previously adsorbed Rh and the Al atoms were broken and the second Rh atom mostly kept its initial geometry. The adsorption energy of this configuration was calculated to be -3.67 eV and the average bond distance of the second Rh atom was 2.32 Å. Based on the Rh-Al(1)-B2 configuration, the second Rh atom was located on the Al(2) atom and bonded to the previously adsorbed Rh atom (2Rh-Al(1)-B2(1)). After relaxation,the bond between the previously adsorbed Rh atom and the subsurface Al(5) atom was broken whereas the bond between the Al(2) atom and the O(C) atom was formed (Fig. 4.25). The second Rh atom was also bonded to the O(M) atom. The adsorption energy was the lowest among the all configuration around on Al(1), namely -2.85 eV and the average bond distance of the secondly adsorbed Rh atom was found to be 2.50 Å. In the last configuration, (2Rh-Al(1)-B2(2)), the second Rh atom was on the Al(6) atom while it bonded to the initially adsorbed Rh atom (Fig. 4.26). At the end of the calculation, the second Rh atom moved towards the region where the Al(4) atom and O(D) atom were located and it changed its initial position considerably. The adsorption energy for this configuration of -3.71 eV, was higher than the other two configurations. The average bond distance for the second Rh atom was calculated to be 2.31 Å.

Based on the adsorption of the single Rh atom on the Al(2) atom configuration, it was observed that both the bridging and embedded configurations had the same final geometry. Therefore, there was only one configuration in which the second Rh atom could be added in the configuration. Using the Rh-Al(2)-E configuration, the second Rh atom was added in three ways. First of all, the second Rh atom was placed on the Al(4) atom and bounded to previously adsorbed Rh atom on the surface (2Rh-Al(2)-E(1)). After calculation, a bond between the added Rh atom and the O(D) atom was formed whereas the bond between the

Al(4) atom and the O(D) atom disappeared as seen in Fig. 4.27. The adsorption energy of the second Rh atom was almost the same as the 2Rh-Al(1)-B2(2) configuration, namely -3.71 eV. The average bond distance was found to be 2.31 Å. Secondly, the Rh atom was added to the configuration such that it was bridged to Al(7) and O(E) atoms bonded the previous adsorbed Rh atom (2Rh-Al(2)-E(2)). After relaxation, there were not crucial changes in the configuration except that a bond formed between the previously adsorbed Rh atom and the subsurface atom Al(5) (Fig. 4.28). The adsorption energy of this configuration was considerably lower than the previous one, -2.40 eV and the average bond distance of the second Rh atom was found to be 2.41 Å. For the last configuration, the second Rh atom was located on the Al(1) atom bonded the adsorbed Rh atom as seen in Fig. 4.29 (2Rh-Al(2)-E(3)). Then the second Rh atom moved towards the O(A) atom and occupied a bridge position to Al(1), O(A) and the previously adsorbed Rh atoms. The bond between the Al(2) and the O(A) atom was broken and the O(A) atom became tetra-coordinated. The first adsorbed Rh atom moved out of the surface slightly thereby losing its property of being a part of the surface. The adsorption energy and the average bond distance of the second Rh atom were found to be -2.95 eV and 2.33 Å respectively.

Moving on the configurations based on the a single Rh atom adsorption on the Al(3) atom, the second Rh atom was added to configuration in two different ways. In the beginning, the second Rh atom was added on the Al(4) atom in the bridging configuration (2Rh-Al3-B(1)). After relaxation, the previosly adsorbed Rh atom broke its bond with the Al(2) atom and formed a bond with the O(B) atom. Furthermore the second Rh atom formed a bond with the O(E) atom while the bonds between the Al(4)-O(B) atoms and the Al(4)-O(E) atoms were broken (Fig. 4.30). The adsorption energy of the second Rh atom was found to be large (-3.44 eV) and the average bond distance of the second Rh atom was found to be 2.26 Å. Next, the second Rh atom was located on the O(A) atom bonded the previously adsorbed Rh atom (2Rh-Al3-B(2)). At the end of the relaxation, the second Rh atom kept its inial position while the bond between the Al(2) atom and O(A) atom was broken. The previously adsorbed Rh atom seperated from the Al(3) atom and then it moved towards to the O(B) atom (Fig. 4.31). The adsorption energy of this configuration, -3.36 eV, was found to be lower than the previous one. The average bond distance was calculated to be 2.21 Å.

Starting with the Rh-Al(4)-E configuration, the second Rh atom was added to the configuration in the bridging configurations on the Al(3), Al(4) and Al(7) atom respectively. Although

these configurations did not have the similar environment, the configurations on the Al(3) and Al(4) atoms (2Rh-Al(4)-E(1) and 2Rh-Al(4)-E(2)) gave very similar results after relaxation (Fig. 4.32). The second Rh atom which was bound to the Al(3) atom moved towards the Al(4) atom whereas the second Rh atom which was bound on the Al(3) atom moved towards the Al(3) atom during relaxations. None of the bonds was broken while only a bond between the second Rh atom and the Al(4) atom (or Al(3) atom) was formed. The adsorption energies of these two configuration were the same (-3.17 eV) and the average bond distance of the second Rh atom was also the same (2.55 Å). The second Rh atom was placed on the Al(7) atom attached the previously adsorbed one (2Rh-Al(4)-E(3)). After relaxation the second Rh atom became tetra-coordinated and two bonds were formed between the second Rh atom and the surface atoms (Fig. 4.33). The adsorption energy of this configuration was calculated to be -2.79 eV and the average bond distance of the second Rh atom was found to be 2.47 Å.

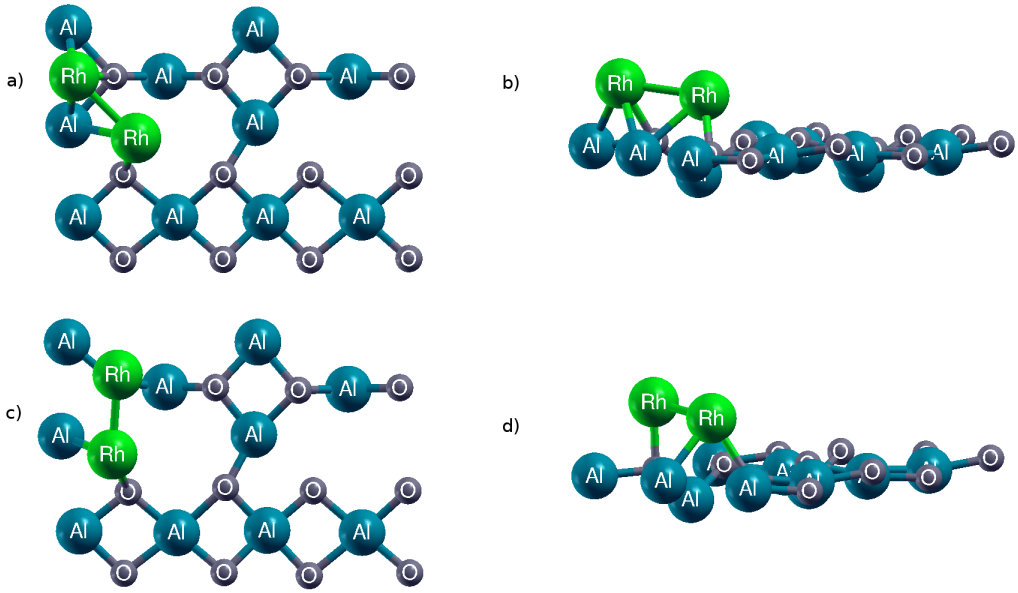

Figure 4.24: Adsorption of the second Rh atom adsorption in the 2Rh-Al(1)-B1 configuration, (a) and (b) are the initial , (c) and (d) are the final top and side views

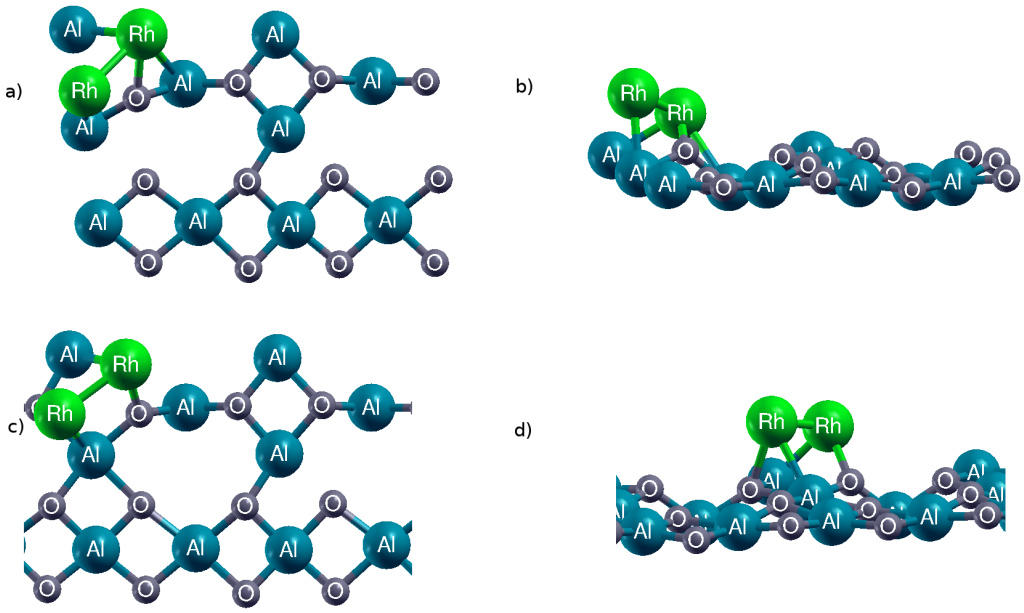

Figure 4.25: Adsorption of the second Rh atom adsorption in the 2Rh-Al(1)-B2(1) configuration, (a) and (b) are the initial , (c) and (d) are the final top and side views

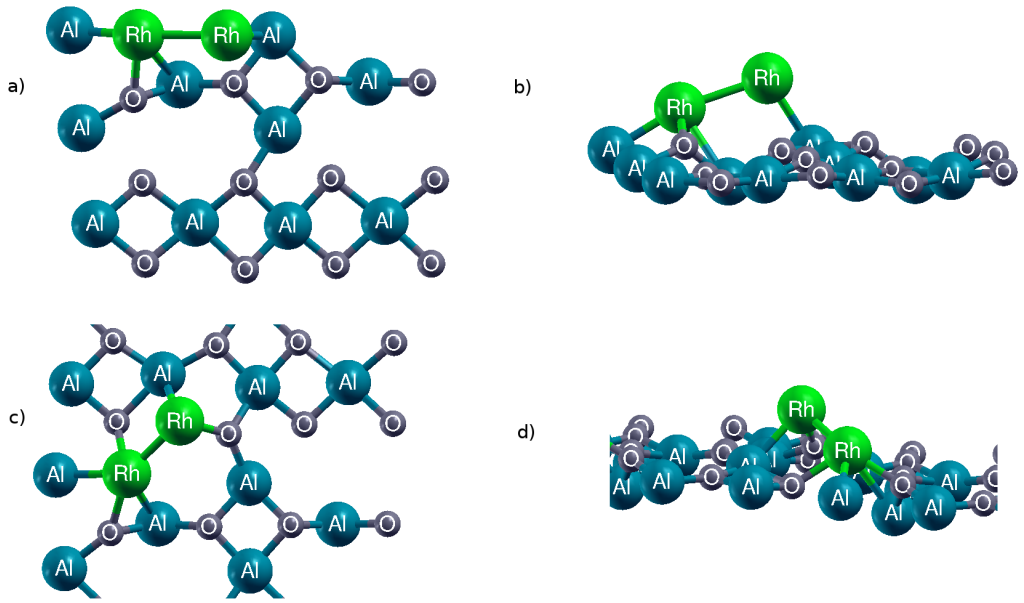

Figure 4.26: Adsorption of the second Rh atom adsorption in the 2Rh-Al(1)-B2(2) configuration, (a) and (b) are the initial , (c) and (d) are the final top and side views

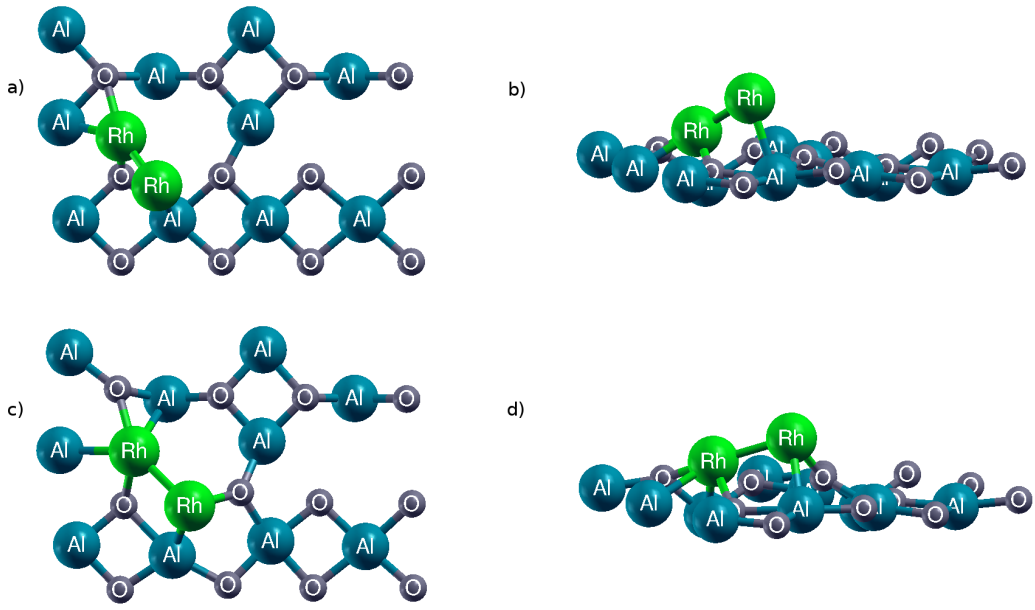

Figure 4.27: Adsorption of the second Rh atom adsorption in the 2Rh-Al(2)-E(1) configuration, (a) and (b) are the initial , (c) and (d) are the final top and side views

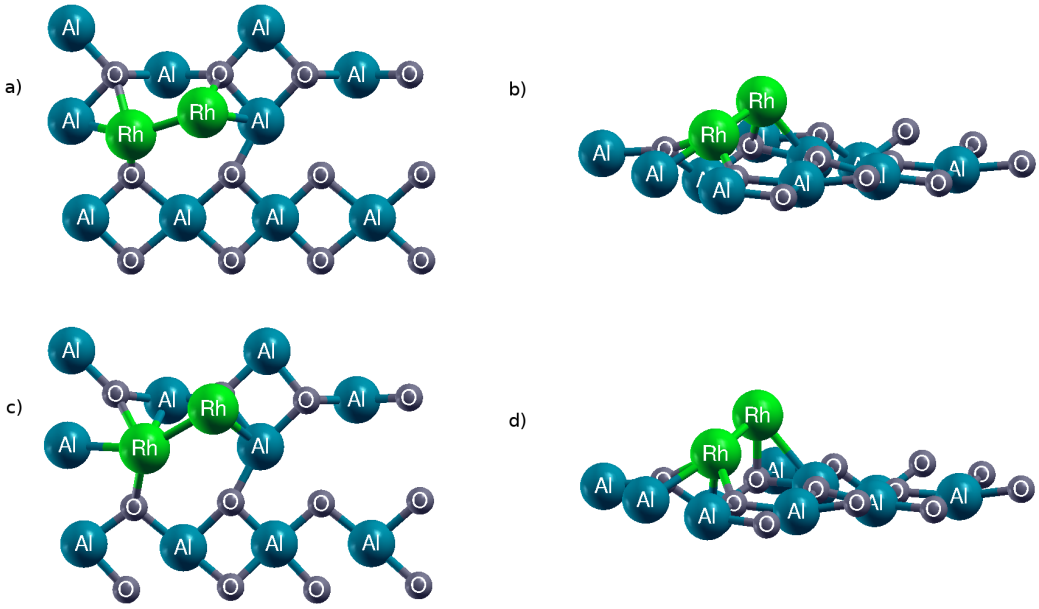

Figure 4.28: Adsorption of the second Rh atom adsorption in the 2Rh-Al(2)-E(2) configuration, (a) and (b) are the initial , (c) and (d) are the final top and side views

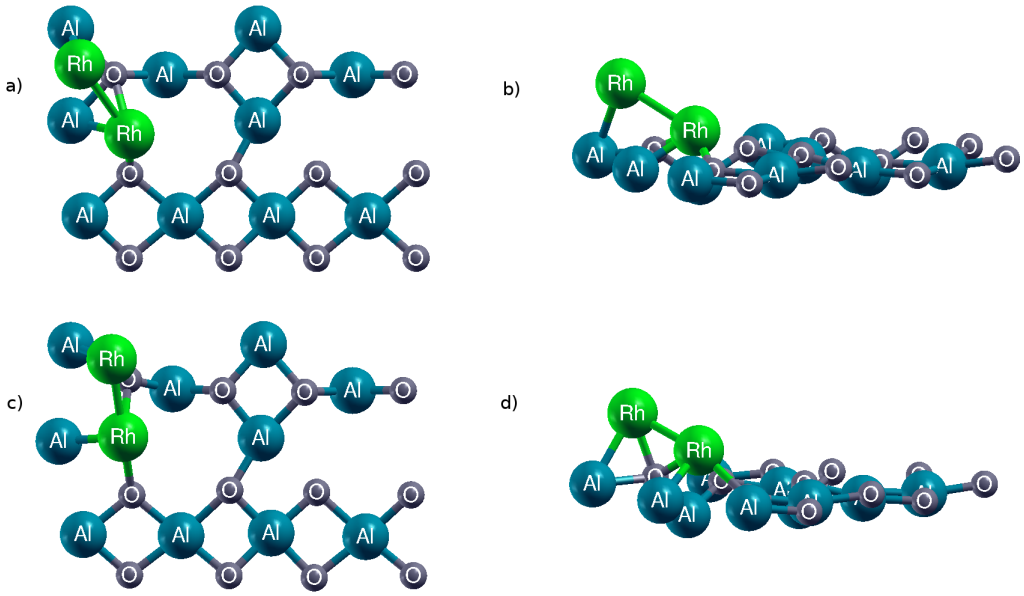

Figure 4.29: Adsorption of the second Rh atom adsorption in the 2Rh-Al(2)-E(3) configuration, (a) and (b) are the initial , (c) and (d) are the final top and side views

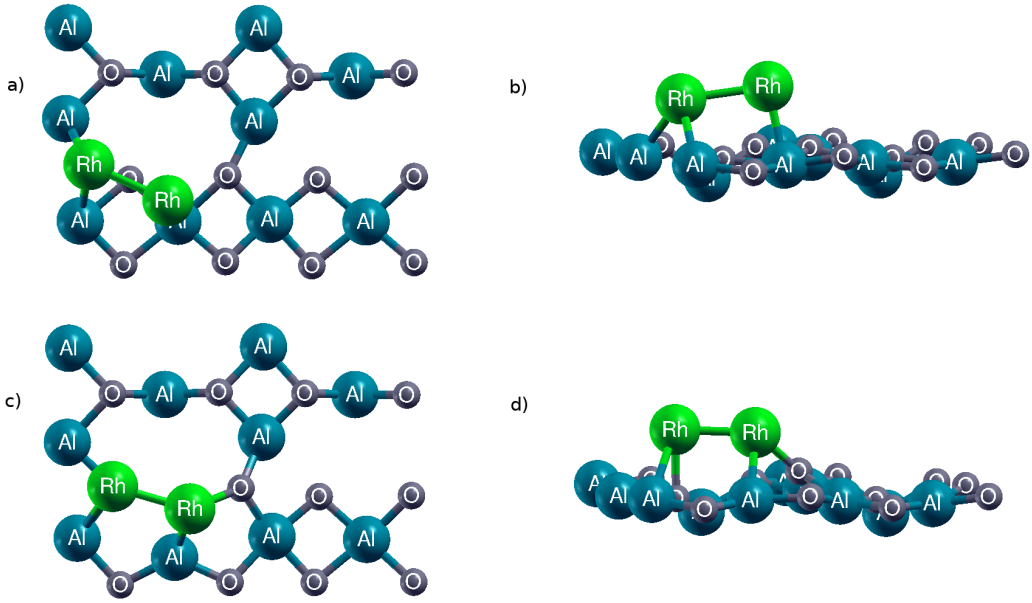

Figure 4.30: Adsorption of the second Rh atom adsorption in the 2Rh-Al(3)-B(1) configuration, (a) and (b) are the initial , (c) and (d) are the final top and side views

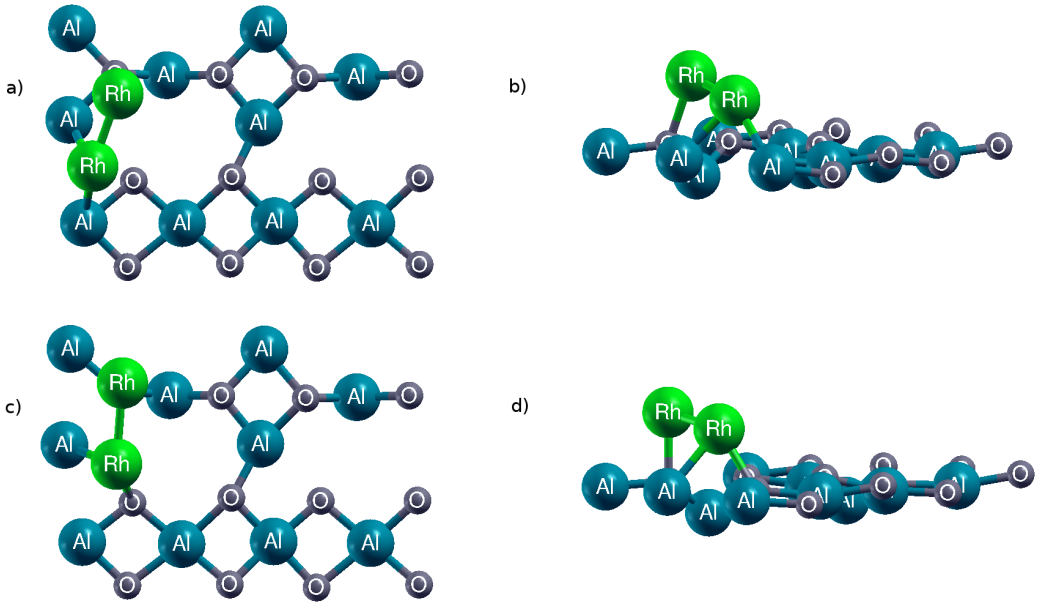

Figure 4.31: Adsorption of the second Rh atom adsorption in the 2Rh-Al(3)-B(2) configuration, (a) and (b) are the initial , (c) and (d) are the final top and side views

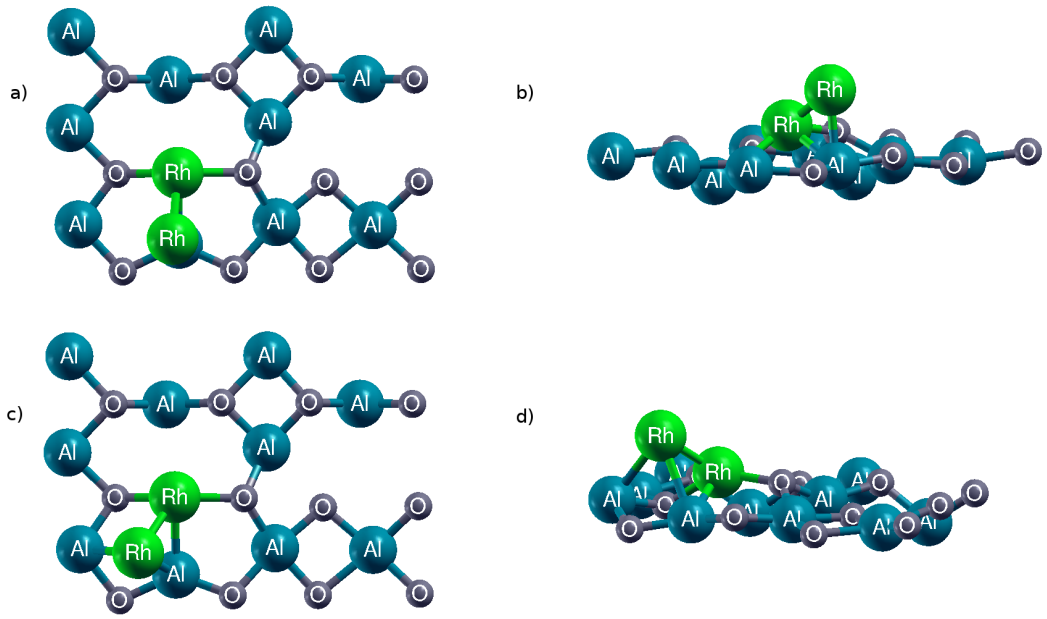

Figure 4.32: Adsorption of the second Rh atom adsorption in the 2Rh-Al(4)-E(1) configuration, (a) and (b) are the initial , (c) and (d) are the final top and side views

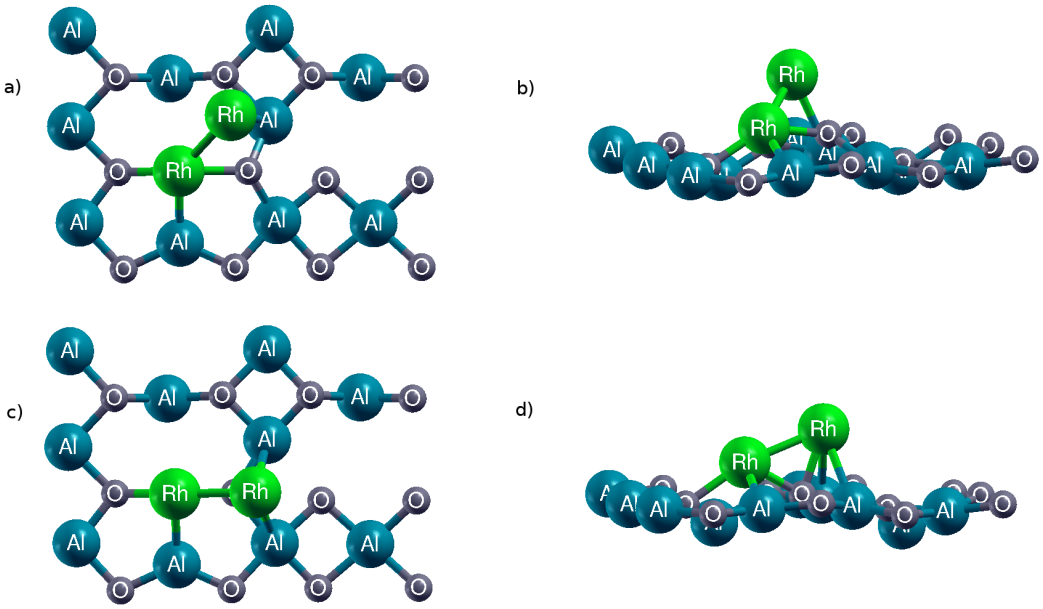

Figure 4.33: Adsorption of the second Rh atom adsorption in the 2Rh-Al(4)-E(3) configuration, (a) and (b) are the initial , (c) and (d) are the final top and side views

In Table 4.6 and table 4.7, the final geometries, adsorption energies of the second Rh atom and the bond distances of the relaxed 2Rh/γ-Al_2O_3(100) configurations are given.

Table 4.6: The final geometries and adsorption energies of the relaxed 2Rh/γ-Al_2O_3(100) configurations

Configuration	Description	E_{ads}
2Rh-Al(1)-B1	Bridge to Al(2),O(B) and Rh	-3.67
2Rh-Al(1)-B2(1)	Bridge to Al(2),O(M) and Rh	-2.85
2Rh-Al(1)-B2(2)	Bridge to Al(4),O(D) and Rh	-3.71
2Rh-Al(2)-E(1)	Bridge to Al(4),O(E) and Rh	-3.67
2Rh-Al(2)-E(2)	Bridge to Al(7),O(F) and Rh	-3.71
2Rh-Al(2)-E(3)	Bridge to Al(1),O(A) and Rh	-3.71
2Rh-Al(3)-B(1)	Bridge to Al(4),O(E) and Rh	-3.44
2Rh-Al(3)-B(2)	Bridge to O(A) and Rh	-3.36
2Rh-Al(4)-E(1) 2Rh-Al(4)-E(2)	Bridge to Al(3),Al(4) and Rh	-3.17
2Rh-Al(4)-E(3)	Bridge to Al(7), Al(8), O(E) and Rh	-3.71

Table 4.7: The bond distances (Å) of the relaxed 2Rh/γ-Al_2O_3(100) configurations

Configuration	Rh-Al		Rh-O		Rh-Rh
2Rh-Al(1)-B1	Rh-Al(2)	2.43	Rh-O(B)	2.13	2.39
2Rh-Al(1)-B2(1)	Rh-Al(2)	2.54	Rh-O(M)	2.15	2.47
2Rh-Al(1)-B2(2)	Rh-Al(4)	2.41	Rh-O(D)	2.04	2.40
2Rh-Al(2)-E(1)	Rh-Al(4)	2.41	Rh-O(E)	2.04	2.46
2Rh-Al(2)-E(2)	Rh-Al(7)	2.68	Rh-O(F)	2.09	2.46
2Rh-Al(2)-E(3)	Rh-Al(1)	2.47	Rh-O(A)	2.04	2.49
2Rh-Al(3)-B(1)	Rh-Al(4)	2.36	Rh-O(E)	2.04	2.37
2Rh-Al(3)-B(2)	-		Rh-O(A)	2.02	2.39
2Rh-Al(4)-E(1)	Rh-Al(3)	2.62	-		2.40
2Rh-Al(4)-E(2)	Rh-Al(4)	2.62			
2Rh-Al(4)-E(3)	Rh-Al(7)	2.72	Rh-O(E)	2.00	2.53
	Rh-Al(8)	2.62			

4.4.3 Simultaneous Adsorption of Pt and Rh Atoms on the γ-Al_2O_3(100) Surface

The simultaneous adsorptions of Pt and Rh atoms on the γ-Al_2O_3(100) surface were done based on the adsorptions of the single Pt atom and Rh atom configurations. In the first part of this section we discuss the addition of a Rh atom to the systems where the the Pt atom had been already adsorbed and these configurations are labeled as Rh+Pt/γ-Al_2O_3(100) configurations. In the second part, the Pt atom is added to the systems with an already adsorbed Rh atom, labeled Pt+Rh/γ-Al_2O_3(100) configurations.

Starting with adsorption of a single Pt configurations obtained previously, the Rh atom was added to configurations in similar configurations. Following the same precedure, Pt-Al(1) configurations were the starting point for the addition of the Rh atom. The Rh atom was added to the Pt-Al(1)-B1 and Pt-Al(1)-B2 configurations respectively. The Rh was first bridged to the O(B) atom and the Pt atom in the Pt-Al(1)-B1 configuration (Rh-Pt-Al(1)-B1). After relaxation, considerable changes were observed in atomic positions. The bonds of the Pt atom with Al(2) and O(A) atoms and that between Al(2) and O(A) atoms were broken. In addition, Rh remained bonded to Pt atom (Fig. 4.34). The Rh atom was found to be stable in this configuration since its adsortion energy was found to be -4.13 eV. The average bond distance of the Rh atom was found to be 2.29 Å. Placing the Rh atom close to Al(2) resulted in the

disintegration of the bond between the Pt and O(A) (Rh-Pt-Al(1)-B2). An additional bond with surface O(M) atom was formed (Fig. 4.35). The adsorption of the secondary atom (Rh) was found to be -3.40 eV and its average bond distance was calculated to be 2.29 Å.

For the Pt-Al(2)-E system, only one configuration for Rh was considered due to similar environments (Rh-Pt-Al(2)-E). The Rh atom was located on the Al(7) and the Pt atom in bridging position. The Rh atom became tetra-coordinated after relaxation and it formed two additional bonds with the surface O(E) and O(F) atoms (Fig. 4.36). Beyond this, no considerable changes on the surface were observed. This configuration gave lower adsorption energy than the Rh+Pt/γ-Al_2O_3(100) configurations around the Al(1) atom. The adsorption energy of the additional Rh atom was found to be -2.13 eV and the distance between the Pt and Rh atoms had the highest value, 2.79 Å, among all other Rh+Pt/γ-Al_2O_3(100) diatomic configurations. The average bond distance of the Rh atom was found to be 2.32 Å.

For the Pt-Al(3)-B configuration, the Rh atom was placed on the surface in two different configurations. At the begining, the Rh atom was placed on the O(E) atom and bonded to the Pt atom (Rh-Pt-Al(3)-B(1)). After relaxation, a bond between Rh and Al(4) atoms was formed. However, the bonds between Al(4)-O(E) atoms and Al(4)-O(B) atoms were broken. In addition, the Pt atom kept its coordination number while breaking its bond with the Al(2) atom and the O(E) atom moved out of the surface about 0.40 Å (Fig. 4.37). The adsorption energy and the average bond distance of the Rh atom were found to be -3.67 eV and 2.28 Å respectively. As a second geometry, the Rh atom was placed on the Al(4) atom (Rh-Pt-Al(3)-B(2)). The Rh atom caused a strong unexpected displacement of the Pt atom. The Pt atom separated from the surface Al atoms and repositioned itself on the O(B) atom, while the Rh atom moved towards the Al(3) atom. The Rh atom formed additional bonds with Al(3) and O(C) atoms, whereas the bond between Al(4) and O(C) atoms was broken (Fig.4.38). The adsorption energy of this configuration was calculated to be -3.35 eV and the average bond distance of the Rh atom was found to be 2.43 Å.

To add the Rh atom in the Pt-Al(4)-E1 and Pt-Al(4)-E2 configurations, three appropriate configurations were identified. One of the configurations was prepared according to the Pt-

Al(4)-E1 configuration and the others based on the Pt-Al(4)-E2 configuration. In the first configuration, Rh-Pt-Al(4)-E1, that was attempted formed a bridge between Pt and Al(4) atoms and the Rh atom became bridging to Al(3), Al(4) and the Pt atoms after relaxation (Fig. 4.39). The adsorption energy of the Rh atom for this configuration was calculated to be -2.45 eV and the average bond distance of the Rh atom was found to be 2.51 Å. Then, the Rh atom was placed between O(F) and the previosly adsorbed Pt atoms for the Rh-Pt-Al(4)-E2(1) configuration (Fig. 4.40). During the relaxation, the Rh atom did not exhibit any significant geometric changes and it kept its initial position as seen in Fig. 4.40. The most crucial point of this configuration was that it had the lowest adsorption energy among all the diatomic configurations studied in this work. The adsorption energy and the average bond distance of the Rh atom were found to be -1.83 eV and 2.38 Å respectively. The last calculation to add the Rh atom on the Pt/γ-Al_2O_3(100) systems was performed based on the Pt-Al(4)-E2 configuration. The Rh atom was placed on the O(A) atom in the bridging configuration to the Pt atom. Despite the final geometry of the previous configuration, the Rh atom moved towards the Al(2) atom and it became bridging to Al(2), O(A) and the Pt atoms. This might have happened because the Al(2) was penta-coordinated unlike the tetra-coordinated Al(7) atom and penta-coordinated Al atom readily accepts a larger coordination. The adsorption of the Rh atom for this geometry was found to be -2.46 eV and the average bond distance of the Rh atom was calculated to be 2.38 Å (Fig. 4.41).

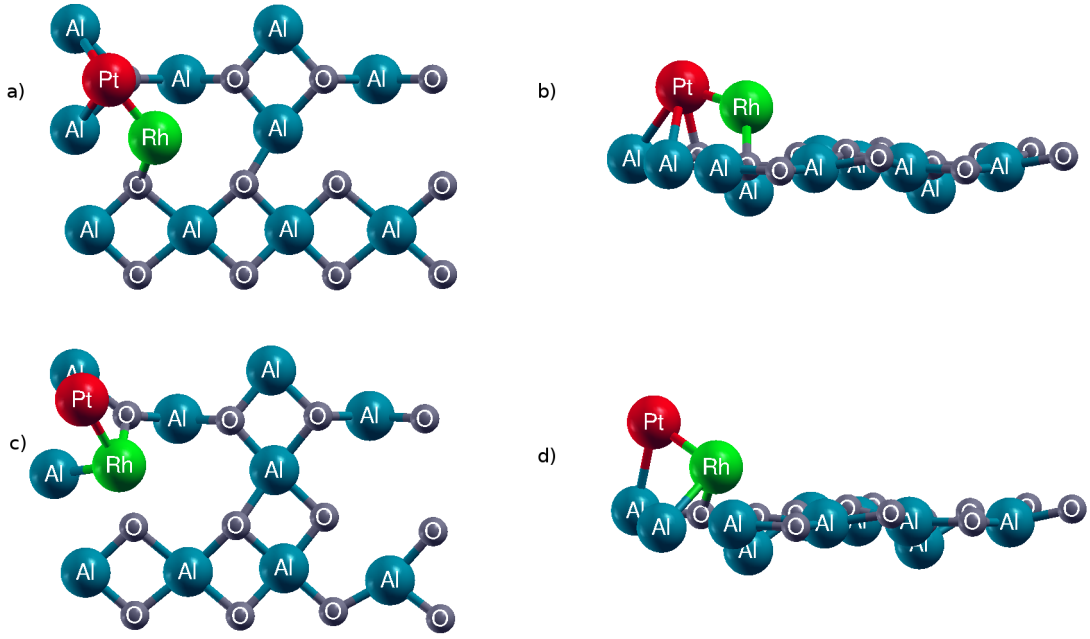

Figure 4.34: Adsorption of the Rh atom in the Rh-Pt-Al(1)-B1 configuration, (a) and (b) are the initial , (c) and (d) are the final top and side views

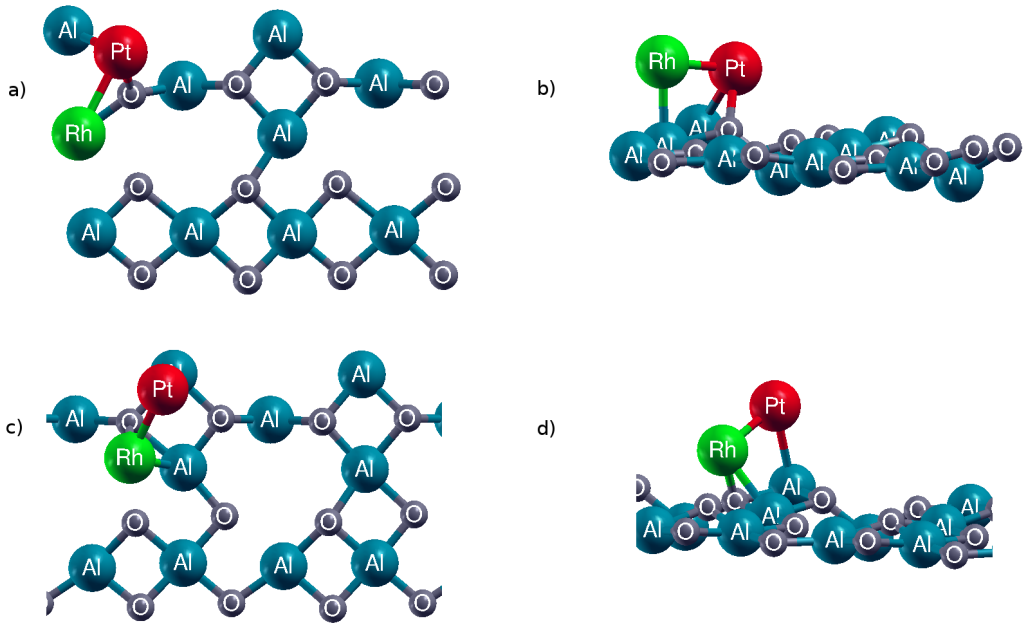

Figure 4.35: Adsorption of the Rh atom in the Rh-Pt-Al(1)-B2 configuration, (a) and (b) are the initial , (c) and (d) are the final top and side views

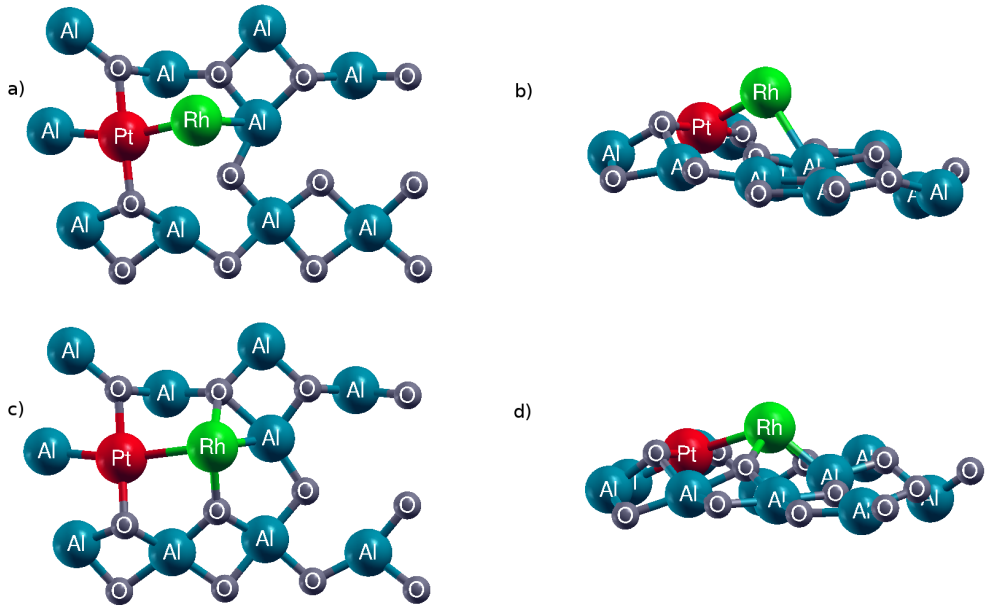

Figure 4.36: Adsorption of the Rh atom in the Rh-Pt-Al(2)-E configuration, (a) and (b) are the initial , (c) and (d) are the final top and side views

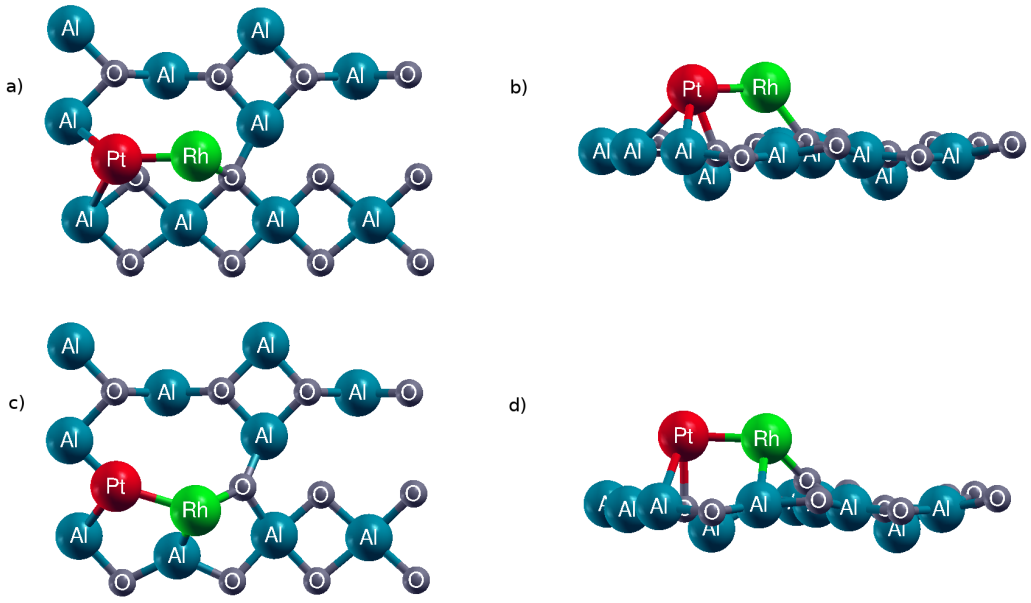

Figure 4.37: Adsorption of the Rh atom in the Rh-Pt-Al(3)-B(1) configuration, (a) and (b) are the initial , (c) and (d) are the final top and side views

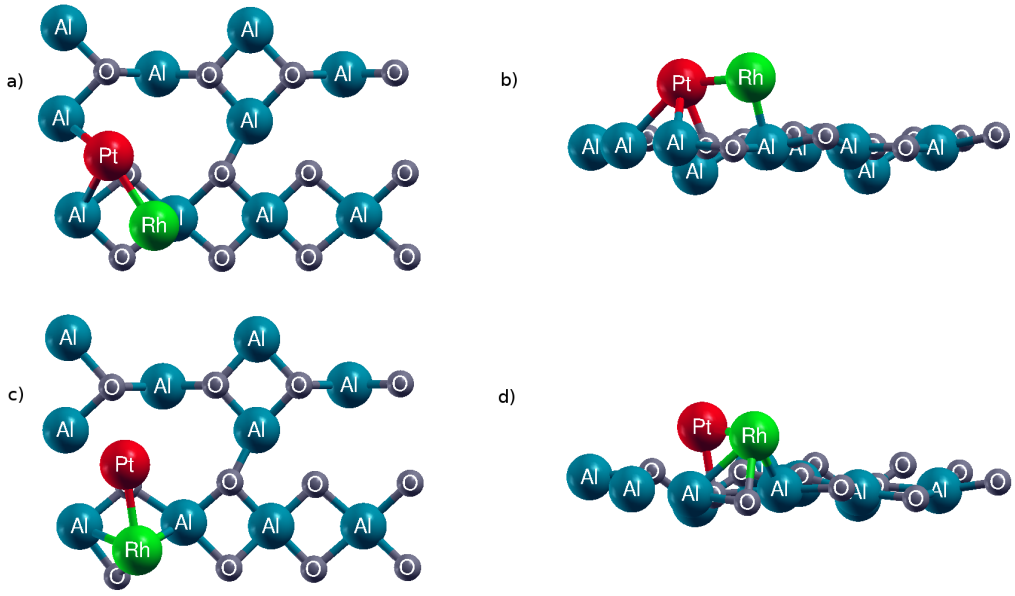

Figure 4.38: Adsorption of the Rh atom in the Rh-Pt-Al(3)-B(2) configuration, (a) and (b) are the initial , (c) and (d) are the final top and side views

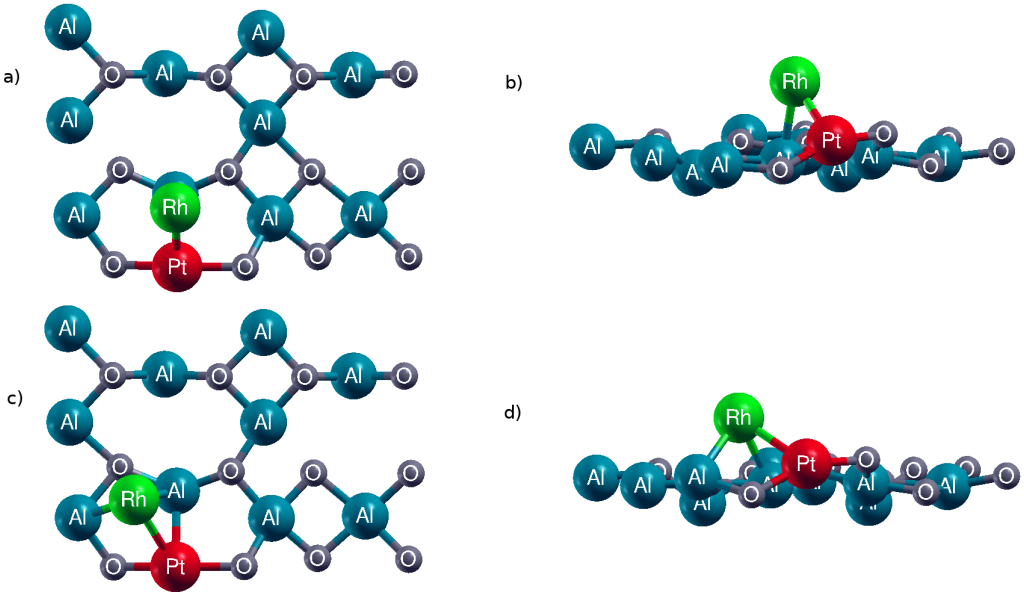

Figure 4.39: Adsorption of the Rh atom in the Rh-Pt-Al(4)-E1 configuration, (a) and (b) are the initial , (c) and (d) are the final top and side views

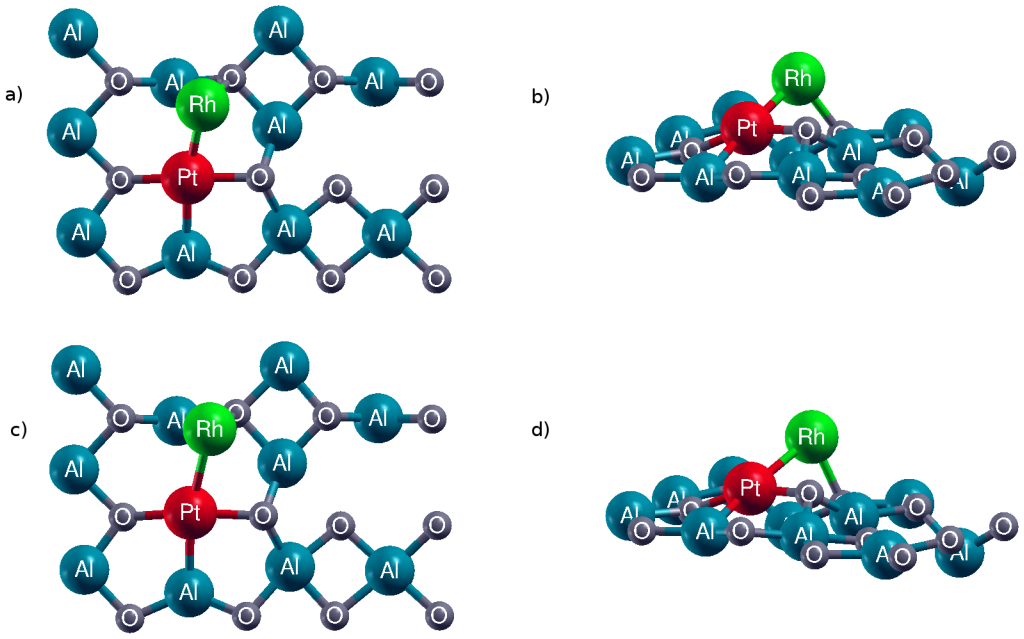

Figure 4.40: Adsorption of the Rh atom in the Rh-Pt-Al(4)-E2(1) configuration, (a) and (b) are the initial , (c) and (d) are the final top and side views

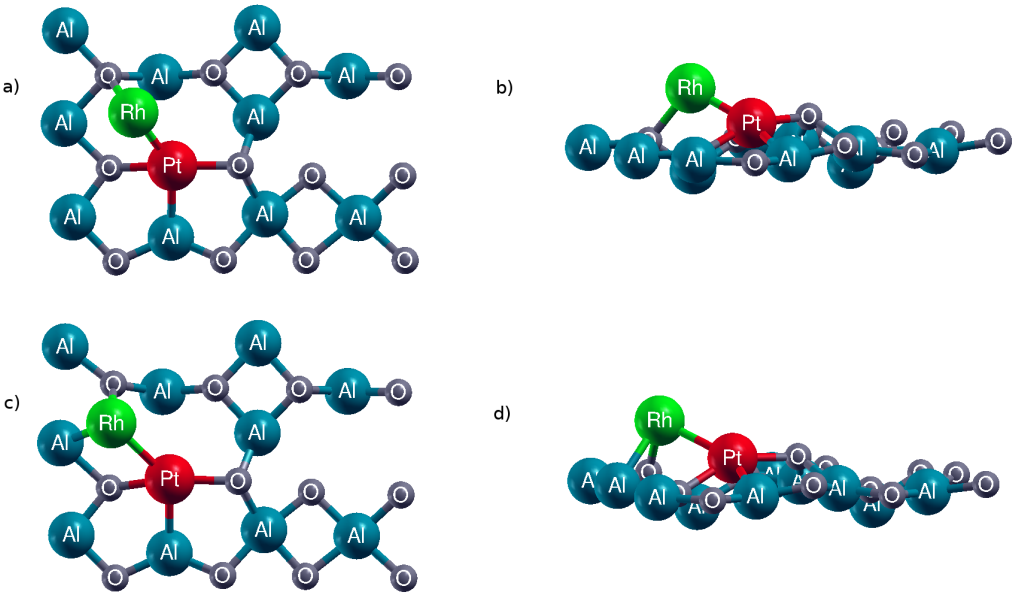

Figure 4.41: Adsorption of the Rh atom in the Rh-Pt-Al(4)-E2(2) configuration, (a) and (b) are the initial , (c) and (d) are the final top and side views

In Table 4.8 and table 4.9, the final geometries, adsorption energies of the Rh atom and the bond distances of the relaxed Rh+Pt/γ-Al_2O_3(100) configurations are given.

Table 4.8: The final geometries and the adsorption energies of the relaxed Rh+Pt/γ-Al_2O_3(100) configurations

Configuration	Description	E_{ads}
Rh-Pt-Al(1)-B1	Bridged to Al(2), O(A) and Pt	-4.13
Rh-Pt-Al(1)-B2	Bridged to Al(2), O(M) and Pt	-3.40
Rh-Pt-Al(2)-E	Bridged to Al(7), O(E), O(F) and Pt	-2.13
Rh-Pt-Al(3)-B(1)	Bridged to Al(4), O(E) and Pt	-3.35
Rh-Pt-Al(3)-B(2)	Bridged to Al(3), Al(4),O(C) and Pt	-3.35
Rh-Pt-Al(4)-E1	Bridged to Al(3), Al(4) and Pt	-2.45
Rh-Pt-Al(4)-E2(1)	Bridged to O(F) and Pt	-1.83
Rh-Pt-Al(4)-E2(2)	Bridged to Al(2), O(A) and Pt	-2.46

Table 4.9: The bond distances (Å) of the relaxed Rh+Pt/γ-Al_2O_3(100) configurations

Configuration	Rh-Al	Rh-O	Rh-Pt
Rh-Pt-Al(1)-B1	Rh-Al(2) 2.46	Rh-O(A) 1.99	2.42
Rh-Pt-Al(1)-B2	Rh-Al(2) 2.42	Rh-O(A) 2.04	2.41
Rh-Pt-Al(2)-E	Rh-Al(7) 2.03	Rh-O(E) 2.02 Rh-O(E) 2.18	2.79
Rh-Pt-Al(3)-B(1)	Rh-Al(4) 2.41	Rh-O(E) 2.03	2.45
Rh-Pt-Al(3)-B(2)	Rh-Al(3) 2.58 Rh-Al(4) 2.41	Rh-O(C) 2.12	2.59
Rh-Pt-Al(4)-E1	Rh-Al(3) 2.44 Rh-Al(4) 2.44	-	2.65
Rh-Pt-Al(4)-E2(1)	-	Rh-O(F) 2.13	2.63
Rh-Pt-Al(4)-E2(2)	Rh-Al(2) 2.47	Rh-O(A) 2.06	2.62

The Pt atom was added to the Rh/γ-Al_2O_3(100) configurations following the same order. Starting with the Rh atom was around the Al(1) atom, the Rh-Al(1)-B2 configuration was used initially (Pt+Rh-Al(1)-B2(1)). After relaxation, no important changes were observed on the surface except that one of the Rh bonds. A new bond was formed between Rh and O(C) atoms while a former Rh-Al(5) bond was broken (Fig. 4.42). The adsorption energy of the Pt atom was found to be -3.48 eV and the average bond distance of the Pt atom was calculated to be 2.53 Å. After that, the Rh was placed on the Al(1) atom while it was bonded to the adsorbed Pt atom (Pt-Rh-Al(1)-B2(2)). Similar to the previous adsorption, the Pt atom was separated from the subsurface atom Al(5) but it broke its bond with the O(C) atom and became tri-coordinated (Fig. 4.43). Even though both configurations seemed to have similar environ-

ment, the Al(2) atom was tetra-coordinated whereas the Al(3) atom was penta-coordinated. Possibly because of that, the bond between the Rh atom and the Al(2) atom was stronger and thus this configuration was more stable than previous one. The final geometry of this configuration gave the considerably high adsorption energy, with -4.12 eV. The average bond distance of the Rh atom was found to be 2.52 Å. The Rh-Al(1)-B1 configuration was not considered since the final geometry of the Pt-Rh-Al(1)-B2(2) configuration gave a possible configuration which was in the similar environment with the Rh-Al(1)-B1 configuration.

As a second configuration, the Pt atom was placed on the Al(2) atom in the Rh-Al(2)-E configuration in the bridging configuration. After calculation, the Pt atom had a bridging position to the Al(3) and Rh atoms and the bond between Al(2) and O(A) atoms disappeared (Fig. 4.44). The adsorption energy of this geometry was the same as the Rh-Pt-Al(1)-B2(2) configuration, -4.12 eV, and the average bond distance of the Rh atom was found to be 2.53 Å.

Only one configuration was considered for addition of the Pt atom to the Rh-Al(3)-B configuration (Rh-Pt-Al(3)-B). The Rh atom was placed on the Al(4) atom bonded to the Pt atom. It was observed that the bond between Al(4) and the O(C) atoms disappeared as seen in Fig. 4.45. The adsorption energy and the average bond distance of the Pt atom were calculated to be -4.07 eV and 2.45 Å respectively.

For the Rh-Al(4)-E configuration was considered and two possible configurations were attemped. For two configurations considered the Pt atom was placed on Al(3) and Al(7) atoms in the initial configurations respectively. For the first configuration (Pt-Rh-Al(4)-E(1)), the Pt atom formed an additional bond with the Al(4) atom after relaxation and the surface atoms mostly kept their initial positions (Fig. 4.46). The adsorption energy of this configuration was found to be -3.94 eV and the average bond distance of the Pt atom was calculated to be 2.57 Å. For the second configuration (Pt-Rh-Al(4)-E(2)), the Pt atom moved towards the Al(8) atom keeping the bond with the Rh atom (Fig. 4.47). The most crucial change on the surface was that the lifted O(E) atom moved into the surface by about 1 Å going back to its position in the clean surface. The Pt atom was not adsorbed as strongly as the with an adsorption energy of -2.87 eV. The average bond distance value was found to be 2.58 Å.

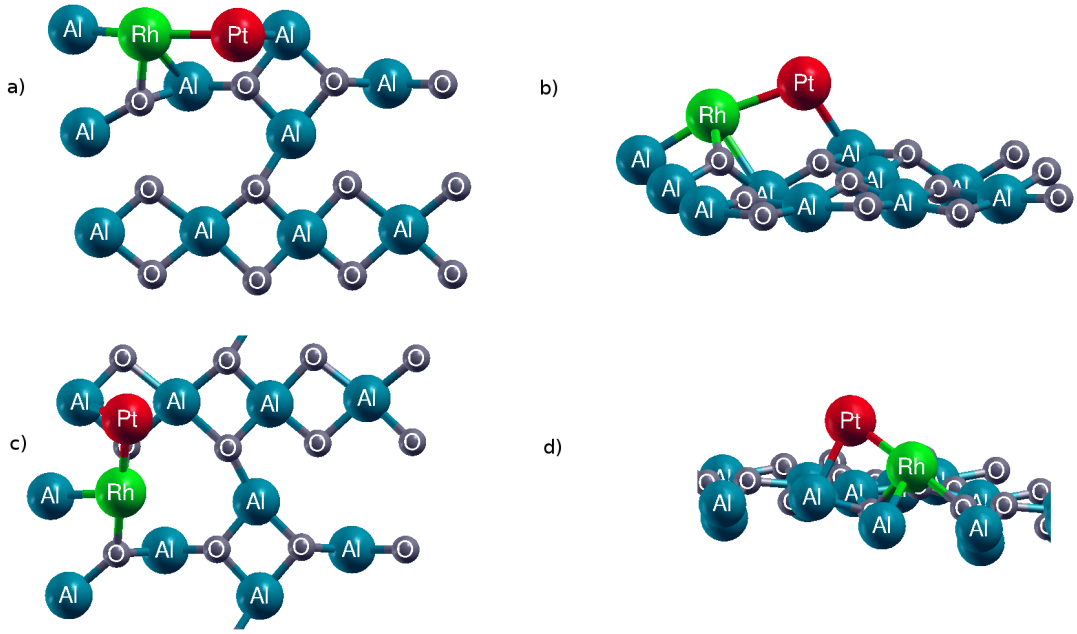

Figure 4.42: Adsorption of the Pt atom in the Pt-Rh-Al(1)-B2(1) configuration, (a) and (b) are the initial , (c) and (d) are the final top and side views

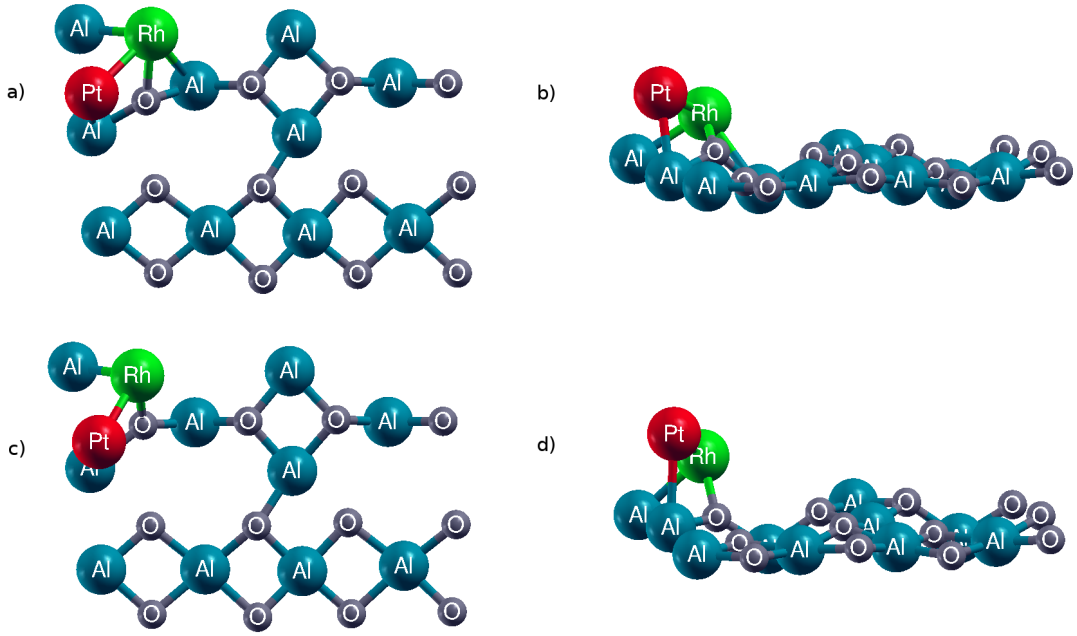

Figure 4.43: Adsorption of the Pt atom in the the Pt-Rh-Al(1)-B2(2) configuration, (a) and (b) are the initial , (c) and (d) are the final top and side views

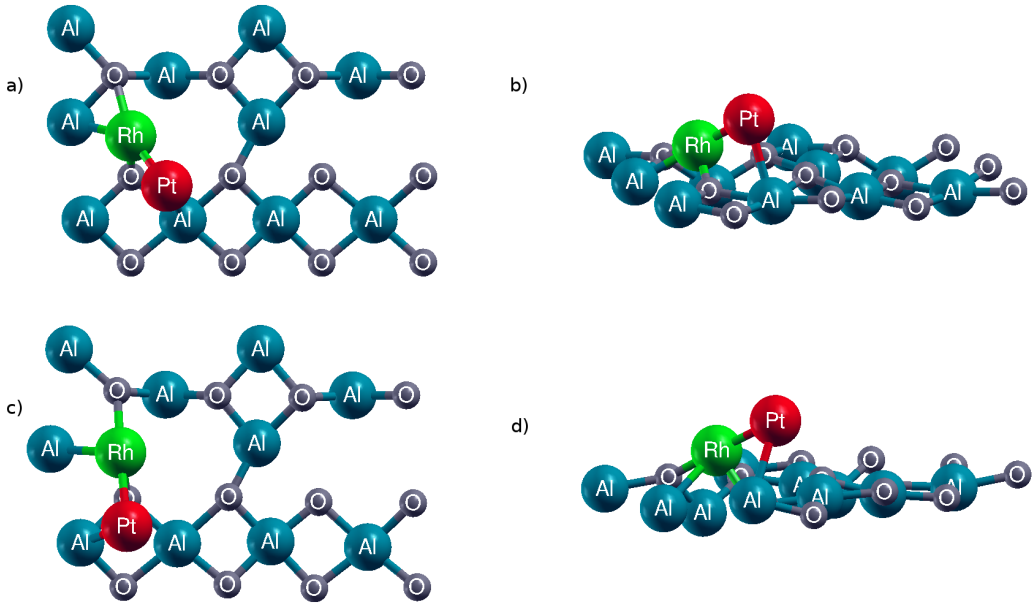

Figure 4.44: Adsorption of the Pt atom in the the Pt-Rh-Al(2)-E configuration, (a) and (b) are the initial , (c) and (d) are the final top and side views

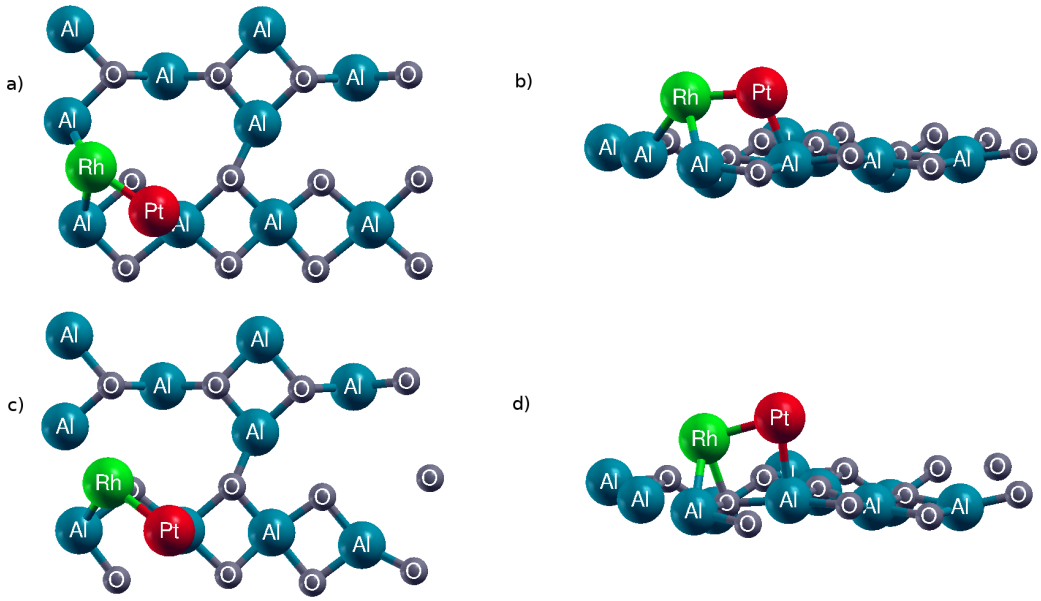

Figure 4.45: Adsorption of the Pt atom in the Pt-Rh-Al(3)-B configuration, (a) and (b) are the initial , (c) and (d) are the final top and side views

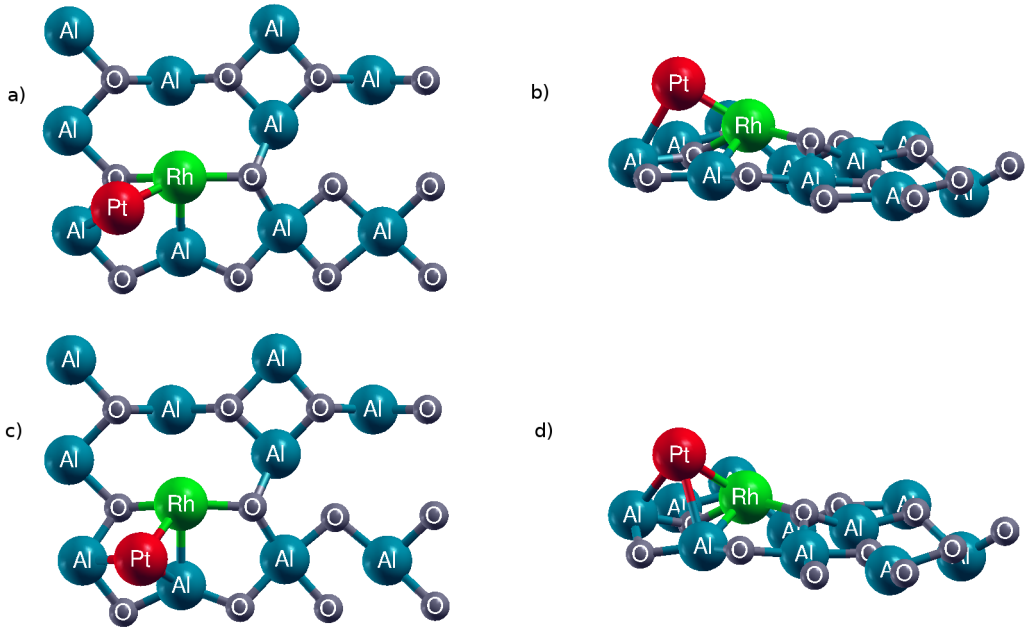

Figure 4.46: Adsorption of the Pt atom in the Pt-Rh-Al(4)-E1(1) configuration, (a) and (b) are the initial , (c) and (d) are the final top and side views

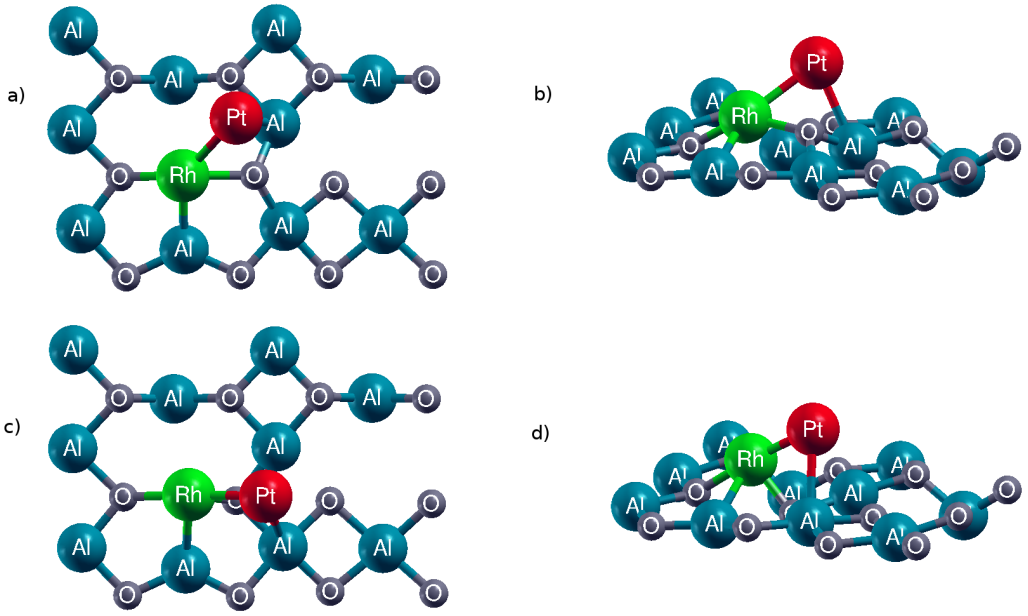

Figure 4.47: Adsorption of the Pt atom in the Pt-Rh-Al(4)-E1(2) configuration, (a) and (b) are the initial , (c) and (d) are the final top and side views

In Table 4.10 and table 4.11 the final geometries, adsorption energies of the Pt atom and the bond distances of the relaxed Pt+Rh/γ-Al_2O_3(100) configurations are given.

Table 4.10: The final geometries and adsorption energies of the relaxed Rh+Pt/γ-Al_2O_3(100) configurations

Configuration	Description	E_{ads}
Pt-Rh-Al(1)-B2(1)	Bridged to Al(3) and Rh	-3.48
Pt-Rh-Al(1)-B2(2)	Bridged to Al(2) and Rh	-4.12
Pt-Rh-Al(2)-E	Bridged to Al(3) and Rh	-4.12
Pt-Rh-Al(3)-B	Bridged to Al(4) and Rh	-4.07
Pt-Rh-Al(4)-E(1)	Bridged to Al(3), Al(4) and Rh	-3.94
Pt-Rh-Al(4)-E(2)	Bridged to Al(8) and Rh	-2.87

Table 4.11: The bond distances (Å) of the relaxed Rh+Pt/γ-Al_2O_3(100) configurations

Configuration	Pt-Al		Pt-O	Pt-Rh
Pt-Rh-Al(1)-B2(1)	Rh-Al(3)	2.62	-	2.45
Pt-Rh-Al(1)-B2(2)	Rh-Al(2)	2.61	-	2.42
Pt-Rh-Al(2)-E	Rh-Al(2)	2.60	-	2.46
Pt-Rh-Al(3)-B	Rh-Al(3)	2.50	-	2.40
Pt-Rh-Al(4)-E(1)	Rh-Al(3) Rh-Al(4)	2.55 2.57	-	2.46
Pt-Rh-Al(4)-E(2)	Rh-Al(8)	2.69	-	2.46

4.5 NO_2 Adsorption on the γ-Al_2O_3(100) Surface

The adsorption of the NO_2 molecule on the γ-Al_2O_3(100) surface was investigated for all configurations mentioned in the previous sections. The NO_2 molecule was studied both in the bridging and monodentate configuraions. The adsorption of the NO_2 molecule on the surface was examined beginning with configurations where the single noble metal was adsorbed following by the diatomic clusters. In the gas phase the NO_2 molecule has an N-O distance of 1.19 Å and an O-N-O angle of 134^o. The adsorption energies, E_{ads}, were defined

$$E_{ads} = E_{slab+metal(s)+NO_2} - E_{slab+metal(s)} - E_{NO_2} \tag{4.5}$$

where $E_{slab+metal(s)+NO_2}$ is the energy of the surface with NO_2 adsorbed, $E_{slab+metal(s)}$ is the

surface energy with one or two metals and E_{NO_2} is the energy of the NO_2 in the gas-phase.

4.5.1 Adsorption of NO_2 on a Single Metal and the γ-Al_2O_3(100) Surface

The NO_2 molecule was placed on the surface in the bridging (B1 and B2 types bridging geometries) and monodentate configurations (M type geometry) on the surface for the single metal adsorbed configurations as shown in Fig. 4.48. All the initial configuration of the NO_2 molecule on the γ-Al_2O_3(100) surface was identified with these configurations, therefore, for this section, only final geometries of the configurations were shown in figures.

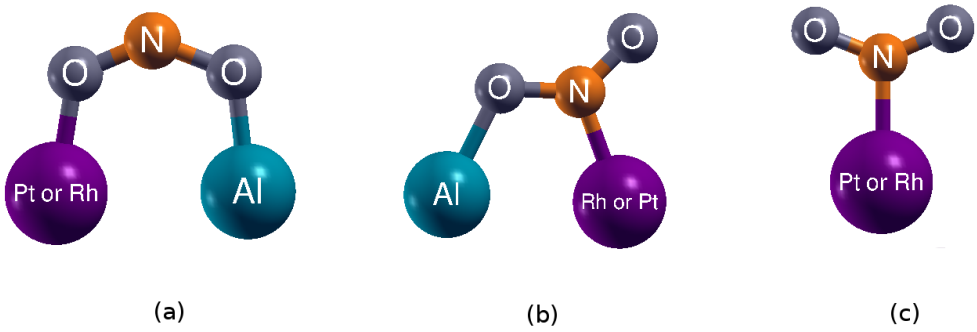

Figure 4.48: The configurations of the NO_2 molecule on the γ-Al_2O_3(100) surface, (a) B1 type and (b)B2 type bridging and (c) M type configurations

For the NO_2+Pt/γ-Al_2O_3(100) and the NO_2+Rh/γ-Al_2O_3(100) configurations, the NO_2 molecule was added to configurations shown in Table 4.2 and table 4.3 in both B1 type and M type geometries for calculations. The other type bridging configuration (B2 type) shown in Fig. 4.48 was formed by some configurations after calculations and it was not used as an initial configuration for calculations of this section.

For the calculations of the NO_2-Pt/γ-Al_2O_3(100) configurations, unfortunately, some of the calculations failed to be stabilized configurations. It was seen that the configurations in which the NO_2 molecule left the surface or separeted from the Pt atom and then bonded to the surface directly failed to be stable. However, we succedded to obtain six stable NO_2-Pt/γ-Al_2O_3(100) configurations (Table 4.12). According to Tab. 4.12, the most remarkable dislocations were observed for the NO_2-Pt-Al(1)-B2 and NO_2-Pt-Al(4)-E2 configurations (Fig. 4.49 and Fig.

4.53). The NO_2 molecules were placed on the Pt atom as monodentate geometry initially, however, after calculation the NO_2 molecule collapsed on the surface and the O_{NO_2} atom bonded to the surface Al(3) atom. In other word, M type configurations became B2 type bridging configurations. The adsorption energies of these configurations were found to be -3.76 eV and -2.40 eV respectively. Although the NO_2 molecule exhibited similar manner on the surface during the calculation for both configurations, a remarkable difference between the NO_2 adsorption energies was observed. This difference could be caused by the location of the Pt atom on the surface. In the NO_2+Pt-Al(1)-B2 configuration, the Pt atom was bridging to the surface whereas the Pt atom was embedded into the surface in the NO_2+Pt-Al(4)-E2 configuration. Another bridging configuration obtained was B1 type and it was around the Al(3) atom (NO_2-Pt-Al(3)-B(1)). This configuration did not exhibit significant changes and it kept its initial geometry during the calculation (Fig. 4.51) the NO_2-Pt-Al(2)-E and the NO_2+Pt-Al(3)-B(2) configurations (Fig. 4.50 and Fig. 4.52). It was observed that the NO_2 molecule was adsorbed more strongly in the NO_2-Pt-Al(3)-B(2) configuration since the adsorption energies of the NO_2 molecules were found to be -0.69 eV and -2.68 eV for the NO_2-Pt-Al(2)-E and NO_2-Pt-Al(3)-B(2) configurations respectively. Similar to the B2 type bridging configuration mentioned above, this noticable difference between the adsorption energies could arise from the location of the Pt atom on the surface. The Pt atom had a bridging geometry in the NO_2-Pt-Al(3)-B(2) configuration but it had an embedded geometry in the NO_2-Pt-Al(2)-E configuration.

The bond distance analysis shown in Table 4.13 gave a remarkable bond distance difference between N-O_{NO_2} atoms for B2 type bridging geometry. It was clearly seen, the bond distance between N-O_{NO_2} atoms was larger when the same O_{NO_2} bonded to the surface Al atoms. For all other configurations (B1 type and M type configurations), the bond distance between N-O_{NO_2} atoms were close to each other. The largest bond distance between N-Pt atoms was found to be 2.20 Å and it was observed in the NO_2-Pt-Al(2)-E configuration which had the lowest adsorption energy of the NO_2 molecule on the surface among all the NO_2+Pt/γ-Al_2O_3(100) configurations.

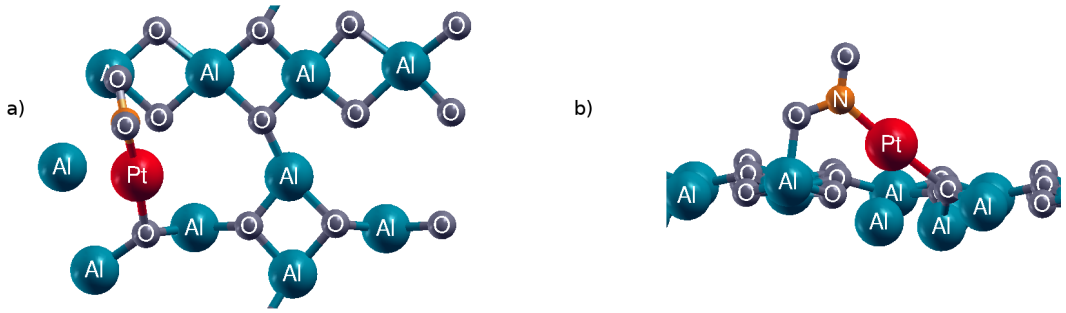

Figure 4.49: The B2 type bridging adsorption of the NO_2 molecule in the NO_2-Pt-Al(1)-B2 configuration, (a) top and (b) side views of the final geometry

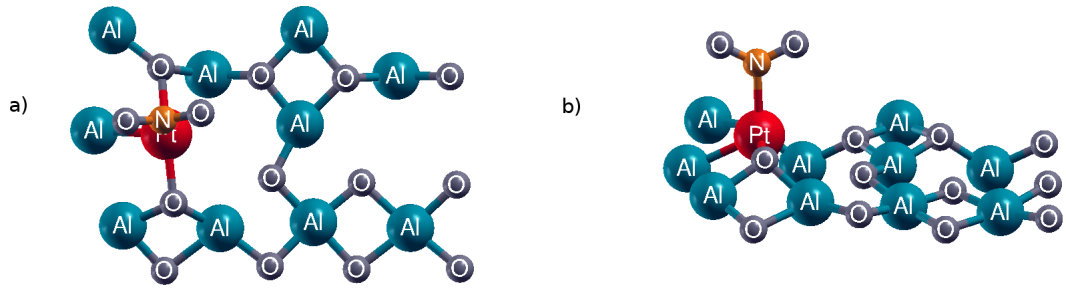

Figure 4.50: The M type adsorption of the NO_2 molecule in the NO_2-Pt-Al(2)-E configuration, (a) top and (b) side views of the final geometry

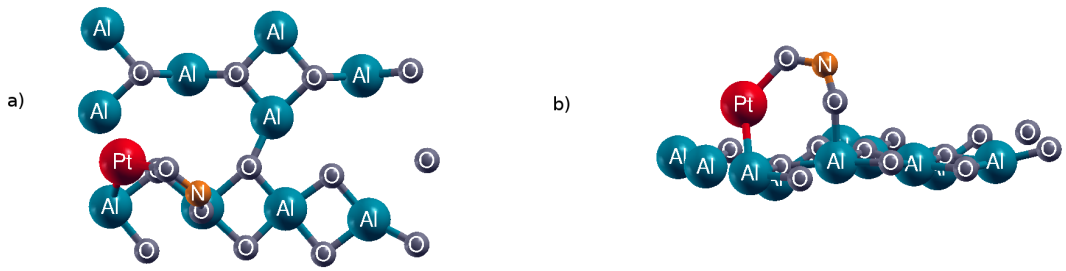

Figure 4.51: The B1 type bridging adsorption of the NO_2 molecule in the NO_2-Pt-Al(3)-B(1) configuration, (a) top and (b) side views of the final geometry

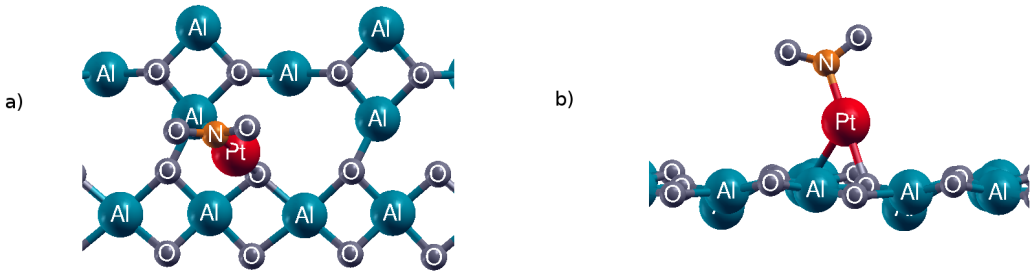

Figure 4.52: The M type adsorption of the NO_2 molecule in the NO_2-Pt-Al(3)-B(2) configuration, (a) top and (b) side views of the final geometry

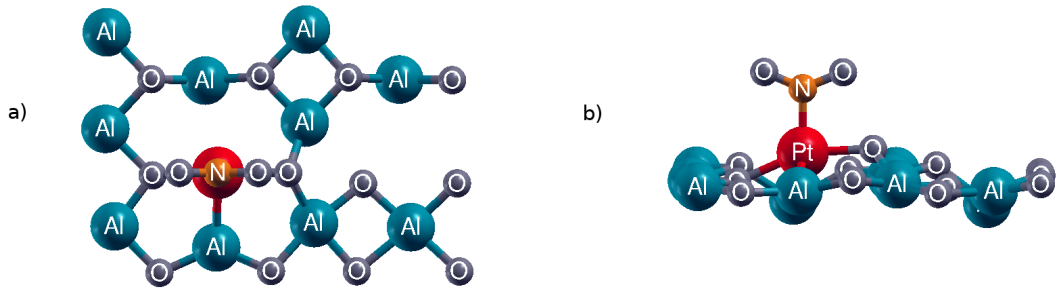

Figure 4.53: The M type adsorption of the NO_2 molecule in the NO_2-Pt-Al(4)-E2 configuration, (a) top and (b) side views of the final geometry

In Table 4.12 and table 4.13, the final geometries, adsorption energies of the NO_2 molecule and the bond distances of the relaxed NO_2+Pt/γ-Al_2O_3(100) configurations are given.

Table 4.12: The final geometries and the adsorption energies of the relaxed NO_2+Pt/γ-Al_2O_3(100) configurations

Configuration	Description	Angle of NO_2	E_{ads}
NO_2-Pt-Al(1)-B1	Bridged to Al(3) and Pt	116.5^o	-3.76
NO_2-Pt-Al(2)-E	monodentate on Pt	126^o	-0.69
NO_2-Pt-Al(3)-B(1)	Bridged to Al(4) and Pt	117^o	-2.62
NO_2-Pt-Al(3)-B(2)	monodentate on Pt	126^o	-2.68
NO_2-Pt-Al(4)-E1	Bridged to Al(3) and Pt	118.5^o	-2.40

Table 4.13: The bond distances (Å) of the relaxed NO_2+Pt/γ-Al_2O_3(100) configurations

Configuration	N-Pt	N-O_{NO_2}	Pt-O_{NO_2}	Al-O_{NO_2}
NO_2-Pt-Al(1)-B1	1.96	1.22 and 1.33	-	Al(3)-O_{NO_2} 1.89
NO_2-Pt-Al(2)-E	2.20	1.23 and 1.24	-	-
NO_2-Pt-Al(3)-B(1)	-	1.29 and 1.27	2.01	Al(3)-O_{NO_2} 1.97
NO_2-Pt-Al(3)-B(2)	1.95	1.23 and 1.26	-	-
NO_2-Pt-Al(4)-E1	1.99	1.22 and 1.30	-	Al(3)-O_{NO_2} 1.92

Although some of the NO_2+Rh/γ-Al_2O_3(100) configurations could not be stabilized, fortunetely, NO_2+Rh/γ-Al_2O_3(100) configurations provided a greater number of stable configurations than NO_2+Pt/γ-Al_2O_3(100) configurations. There were nine stable configurations including two number of the B2 type bridging, six number of the B1 type bridging configurations and one monodentate configuration.

Similar to the NO_2-Pt-Al(1)-B2 and NO_2-Pt-Al(4)-E2 configurations, the most remarkable changes in the initial geometries were observed for NO_2-Rh-Al(1)-B2(2) and NO_2-Rh-Al(2)-E(3) configurations. At the beginning of the calculations these two configurations were M type configurations, however at the end of the calculations they collapsed on the surface and formed the B2 type bridging configurations on the surface (Fig. 4.55 and Fig. 4.58). The adsorption energies were the same for both configurations, with -3.66 eV and these configurations had the strongest NO_2 molecule adsorption among all the NO_2-Rh/γ-Al_2O_3(100) configurations. The B1 types configurations were achieved to be stabilize around Al(1), Al(2), Al(3) and Al(4) atoms as shown in Table 4.14 and they mostly kept their initial geometries. The adsorption energy range of the NO_2 molecule on these six number of the B1 type bridging configurations was between -2.65 eV and -3.20 eV. The lowest adsorption energy of the NO_2 molecule, -2.65 eV, belonged to the NO_2-Rh-Al(4)-E(1) configuration (Fig. 4.60) and the highest energy of the NO_2 molecule, -3.20 eV, belonged to the NO_2-Rh-Al(2)-E(2) configuration (Fig. 4.57). The monodentate configuration of the NO_2 molecule was obtained only succesfully on the Rh-Al(4)-E configuration (Fig. 4.62). The adsorption energy of this unique configuration was found to be -2.55 eV and it was the lowest adsorption energy among all the NO_2+Rh/γ-Al_2O_3(100) configurations.

Considering the bond distance analysis shown in Table 4.15, similar results with the NO_2+Pt/γ-Al_2O_3(100) configurations were seen. The bond distance differences between N-O_{NO_2} atoms was larger when the same O_{NO_2} bonded to the surface Al atoms and the largest bond distance between N-Rh atoms was found to be 1.95 Å belonging to the configuration having the lowest the NO_2 molecule adsorption energy, NO_2-Rh-Al(4)-E(3) configuration (Fig. 4.62).

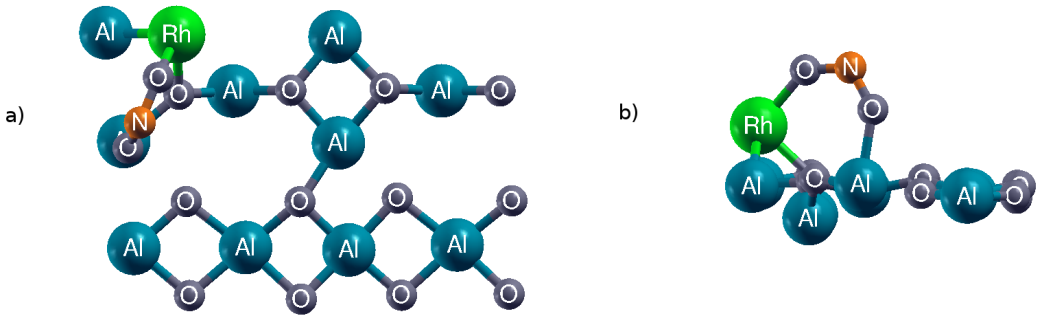

Figure 4.54: The B1 type bridging type adsorption of the NO_2 molecule in the NO_2-Rh-Al(1)-B1(1) configuration, (a) top and (b) side views of the final geometry

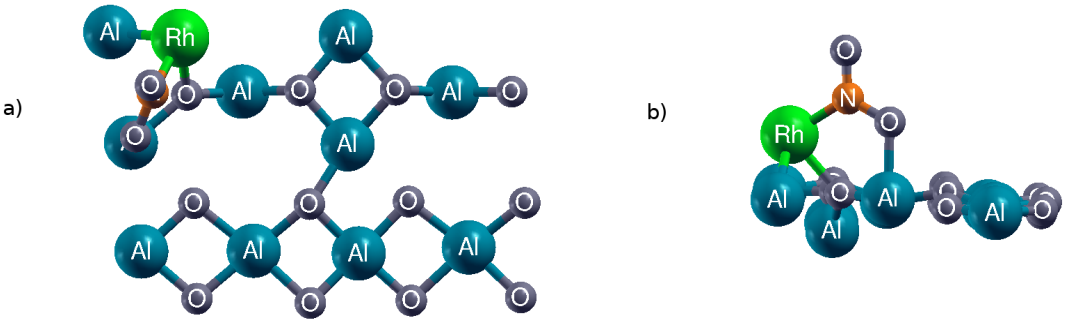

Figure 4.55: The B2 type bridging type adsorption of the NO_2 molecule in the NO_2-Rh-Al(1)-B1(2) configuration, (a) top and (b) side views of the final geometry

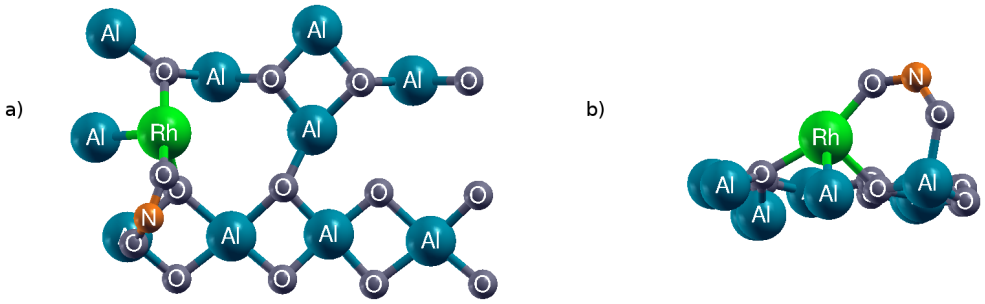

Figure 4.56: The B1 type bridging type NO_2 molecule adsorption in the NO_2-Rh-Al(2)-E(1) configuration, (a) top and (b) side views of the final geometry

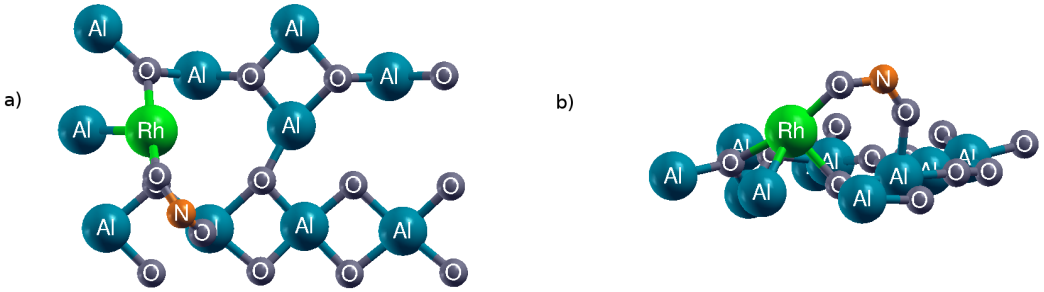

Figure 4.57: The B1 type bridging type NO_2 molecule adsorption in the NO_2-Rh-Al(2)-E(2) configuration, (a) top and (b) side views of the final geometry

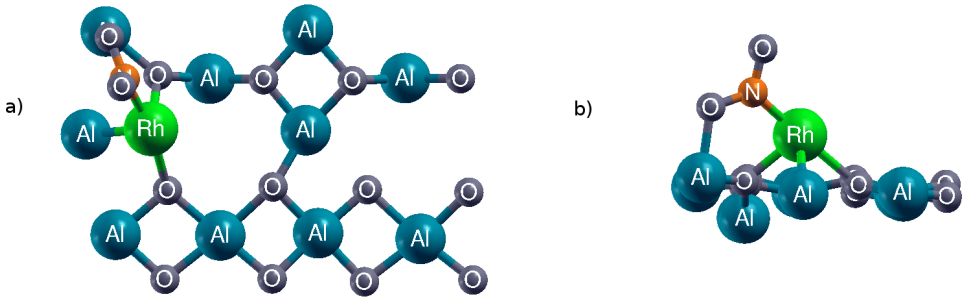

Figure 4.58: The B2 type bridging type NO_2 molecule adsorption in the NO_2-Rh-Al(2)-E(3) configuration, (a) top and (b) side views of the final geometry

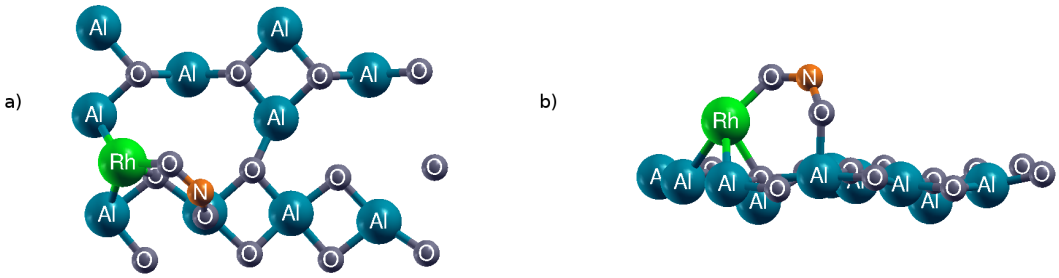

Figure 4.59: The B1 type bridging type NO_2 molecule adsorption in the NO_2-Rh-Al(3)-B configuration, (a) top and (b) side views of the final geometry

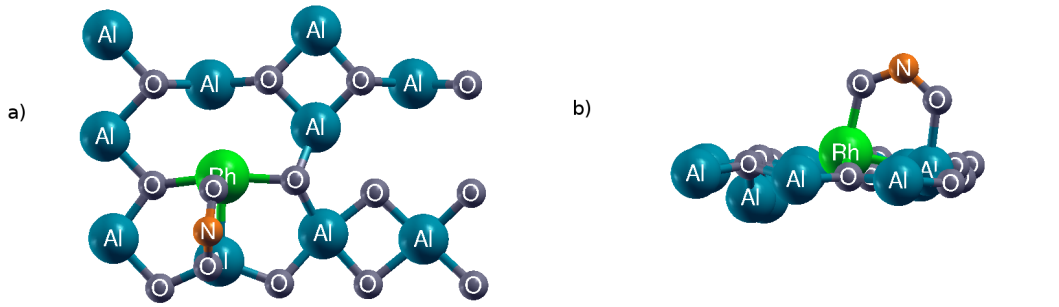

Figure 4.60: The B1 type bridging type NO_2 molecule adsorption in the NO_2-Rh-Al(4)-E(1) configuration, (a) top and (b) side views of the final geometry

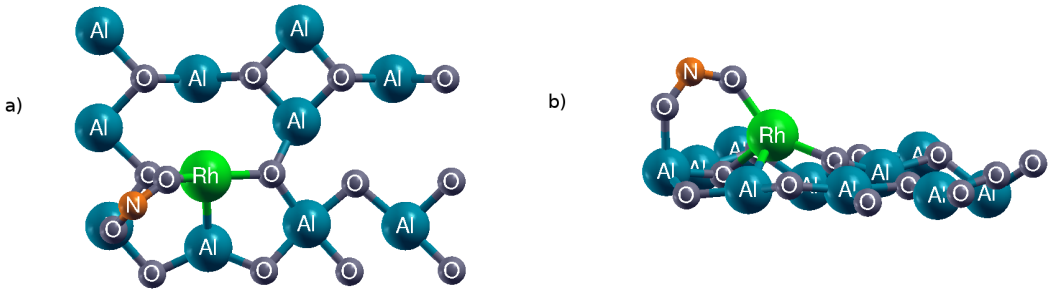

Figure 4.61: The B1 type bridging type NO_2 molecule adsorption in the NO_2-Rh-Al(4)-E(2) configuration, (a) top and (b) side views of the final geometry

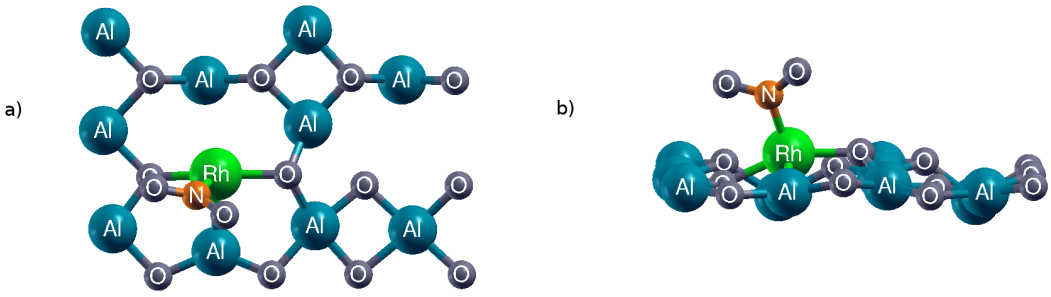

Figure 4.62: The M type NO_2 molecule adsorption in the NO_2-Rh-Al(4)-E(3) configuration, (a) top and (b) side views of the final geometry

In Table 4.14 and Tab. 4.15, the final geometries, adsorption energies of the NO_2 molecule and the bond distances of the relaxed NO_2+Rh/γ-Al_2O_3(100) configurations are given.

Table 4.14: The final geometries and the adsorption energies of the relaxed NO_2+Rh/γ-Al_2O_3(100) configurations

Configuration	Description	Angle of NO_2	E_{ads}
NO_2-Rh-Al(1)-B1(1)	Bridged to Al(2) and Rh	118^o	-2.88
NO_2-Rh-Al(1)-B1(2)	Bridged to Al(2) and Rh	119^o	-3.66
NO_2-Rh-Al(2)-E(1)	Bridged to Al(3) and Rh	117^o	-3.15
NO_2-Rh-Al(2)-E(2)	Bridged to Al(4) and Rh	118.5^o	-3.20
NO_2-Rh-Al(2)-E(3)	Bridged to Al(1) and Rh	119^o	-3.66
NO_2-Rh-Al(3)-B	Bridged to Al(4) and Rh	117^o	-3.15
NO_2-Rh-Al(4)-E(1)	Bridged to Al(4) and Rh	117^o	-2.65
NO_2-Rh-Al(4)-E(2)	Bridged to Al(3) and Rh	117^o	-2.74
NO_2-Rh-Al(4)-E(3)	monodentate on Rh	125^o	-2.55

Table 4.15: The bond distances (Å) of the relaxed NO_2+Rh/γ-Al_2O_3(100) configurations

Configuration	N-Rh	N-O_{NO_2}	Rh-O_{NO_2}	Al-O_{NO_2}
NO_2-Rh-Al(1)-B1(1)	-	1.28 and 1.27	1.97	Al(2)-O_{NO_2} 1.98
NO_2-Rh-Al(1)-B1(2)	1.92	1.23 and 1.31	-	Al(2)-O_{NO_2} 1.96
NO_2-Rh-Al(2)-E(1)	-	1.28 and 1.28	1.99	Al(3)-O_{NO_2} 1.92
NO_2-Rh-Al(2)-E(2)	-	1.28 and 1.28	1.99	Al(4)-O_{NO_2} 1.93
NO_2-Rh-Al(2)-E(3)	1.92	1.23 and 1.31	-	Al(1)-O_{NO_2} 1.97
NO_2-Rh-Al(3)-B	-	1.28 and 1.28	1.98	Al(4)-O_{NO_2} 1.95
NO_2-Rh-Al(4)-E(1)	-	1.28 and 1.28	1.98	Al(4)-O_{NO_2} 1.99
NO_2-Rh-Al(4)-E(2)	-	1.27 and 1.28	1.98	Al(3)-O_{NO_2} 1.93
NO_2-Rh-Al(4)-E(3)	1.95	1.24 and 1.25	-	-

4.5.2 Adsorption of NO_2 on Diatomic Clusters/γ-Al_2O_3(100) Surface

To examine the NO_2 adsorptions for the NO_2+2Pt/γ-Al_2O_3(100) and NO_2+2Rh/γ-Al_2O_3(100) bimetallic configurations, there were calculated three different configurations including two bridging (B1 and B2 type) and one monodentate (M type) configurations (Fig. 4.63). All of these geometries were used as initial geometries for the calculations of this section.

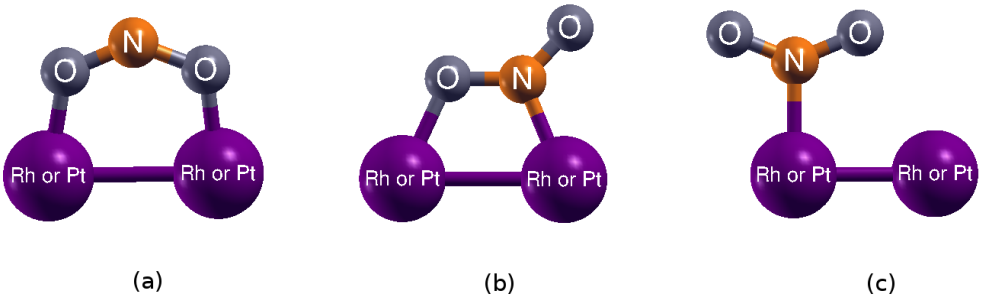

Figure 4.63: The adsorption configurations of the NO_2 molecule on the γ-Al_2O_3(100) surface, (a) B1 type and (b)B2 type bridging and (c) M type configurations

For the NO_2-2Pt/γ-Al_2O_3(100) and NO_2-2Rh/γ-Al_2O_3(100) configurations, the NO_2 molecule was added to configurations shown in Tables 4.4 and 4.6 in both bridging and monodentate configurations as shown in Fig. 4.63. Likely to previous section, some of the calculations could not be reach stable conditions and the most probable reason of this could be caused by disappearing the bonds between the NO_2 molecule and the adsorbed diatomic clusters. Furthermore, the first adsorbed metal atoms on the surface were labeled as Pt(1), Rh(1) and the secondly adsorbed metal atoms on the surface were labeled as Pt(2), Rh(2) in tables of this section.

The calculations of the NO_2-2Pt/γ-Al_2O_3(100) configurations gave twelve number of stable configurations. Five number of these configurations were the B2 type bridging and the M type configurations and rest of two configurations were the B1 type bridging configurations. Most of the configurations could keep their initial geometry during the calculations except the NO_2-Pt-Al(1)-B2-(1), NO_2-2Pt-Al(3)-B(2)-(1) and NO_2-2Pt-Al(3)-B(2)-(2) configurations. The NO_2-2Pt-Al(1)-B2-(1) and NO_2-2Pt-Al(3)-B(2)-(2) configurations exhibited distinguishable different final geometry among all NO_2-2Pt/γ-Al_2O_3(100) configurations. The NO_2 molecule

was placed on the surface in the B2 type bridging configuration for both configurations and the NO_2 molecule kept its B2 type bridging configurations after fully relaxation while the Pt(2) atoms seperated from the surface and they bonded to the only Pt(1) and N atoms as shown the Fig. 4.67 and Fig. 4.70. Due to the seperation of the Pt(2) atom from the surface, the adsorption energies of the NO_2 molecule for these configurations was relatively lower than other the B2 type bridging configurations as shown in Table 4.16. It could be pointed out for these configurations that they could not be accepted as a cluster model on the surface. The NO_2-2Pt-Al(3)-B(2)-(2) configuration had the lowest adsorption energy, -2.13 eV, among all the NO_2-2Pt/γ-Al_2O_3(100) configurations. In addition, the highest adsorption energy of the NO_2 molecule was -4.00 eV and it belonged to another B2 type bridging configuration (NO_2-2Pt-Al(1)-B2-(2)) as shown in Fig. 4.65. The other configuration showed a distinguishable change in its initial geometry was the NO_2-2Pt-Al(3)-B(2)-(1) configuration. According to the previous section results, it was observed that monodandate configurations exhibited tendency to become the B2 type bridging geometry, nevertheless, the NO_2-2Pt-Al(3)-B(2)-(1) configuration exhibited an opposite manner. This sytem had the B2 type bridging geometry initially and after the calculation it became monodante geometry on the Pt(1) atom (Fig. 4.68). Among the other M type configurations, this configuration did not seem to be different and its adsorption energy of the NO_2 molecule was found to be -2.39 eV which was in the range of the adsorption energies of the NO_2 molecule for monodentate configurations as shown in Table 4.16. The B1 type bridging configurations were obtained from the NO_2-2Pt-Al(1)-B1-(1) and NO_2-2Pt-Al(4)-E2-(1) configurations (Fig. 4.64 and Fig. 4.73). The adsorption energies of these two configurations was found to be -3.83 eV and -2.88 eV for NO_2-2Pt-Al(1)-B1-(1) and NO_2-2Pt-Al(4)-E2-(1) configurations respectively.

The bond distance analysis agreed with the observations of the previous section and the bond distance differences between N-O_{NO_2} atoms was larger when the same O_{NO_2} bonded to the Pt atoms and the range of the bond distances of the N-Pt atoms was between 1.94 Å and 2.20 Å. The smallest bond distance between the N and Pt atoms, 1.94 Å, belonged to the NO_2-2Pt-Al(1)-B2-(2) configuration (Fig. 4.68) and the largest bond distance, 2.20 Å, belonged to NO_2-2Pt-Al(3)-B(2)-(2) configuration (Fig. 4.70). Furthermore, the bond distances of Pt-O_{NO_2} atoms were changed between 2.02 Å and 2.09 Å.

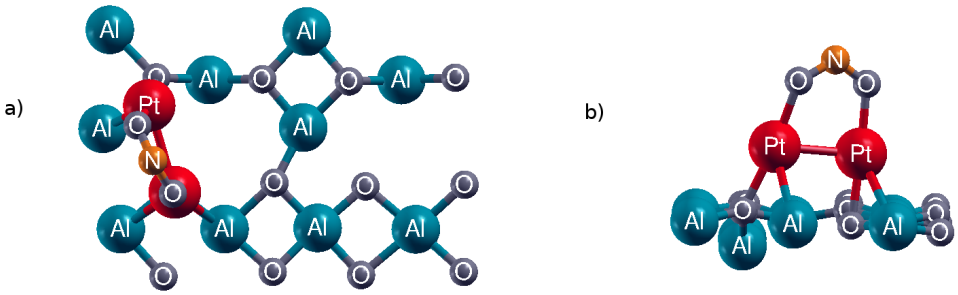

Figure 4.64: The B1 type bridging type NO_2 molecule adsorption in the NO_2-2Pt-Al(1)-B-(1) configuration, (a) top and (b) side views of the final geometry

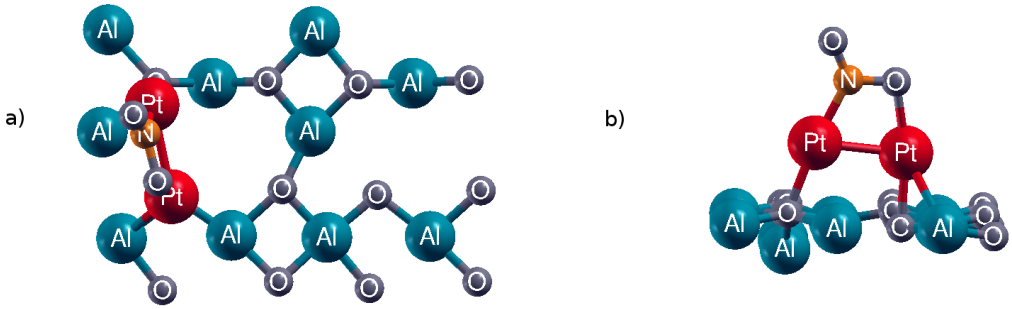

Figure 4.65: The B2 type bridging type NO_2 molecule adsorption in the NO_2-2Pt-Al(1)-B-(2) configuration, (a) top and (b) side views of the final geometry

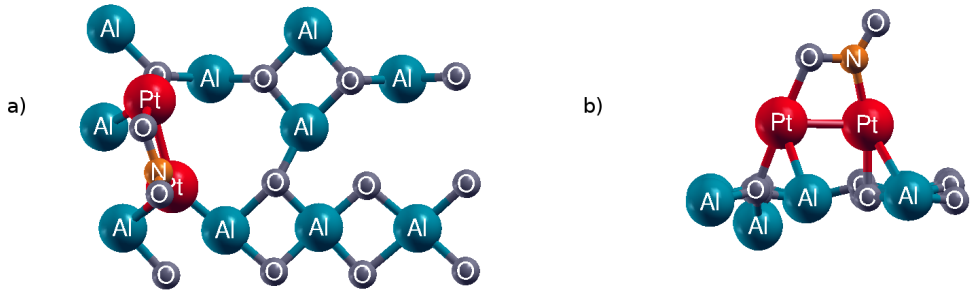

Figure 4.66: The B2 type bridging type NO_2 molecule adsorption in the NO_2-2Pt-Al(1)-B-(3) configuration, (a) top and (b) side views of the final geometry

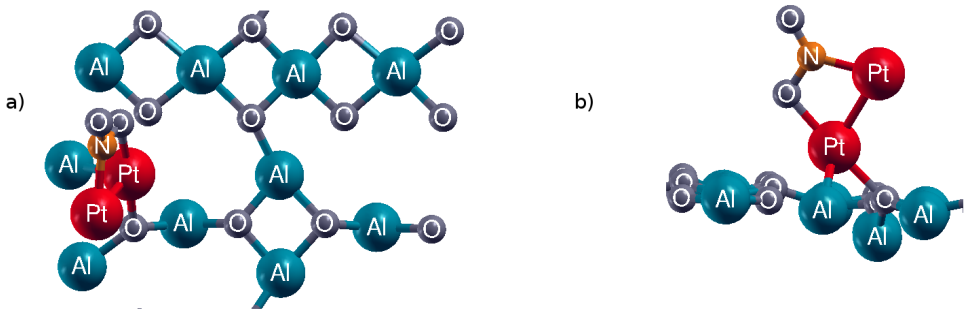

Figure 4.67: The B2 type bridging type NO_2 molecule adsorption in the NO_2-2Pt-Al(1)-B1-(1) configuration, (a) top and (b) side views of the final geometry

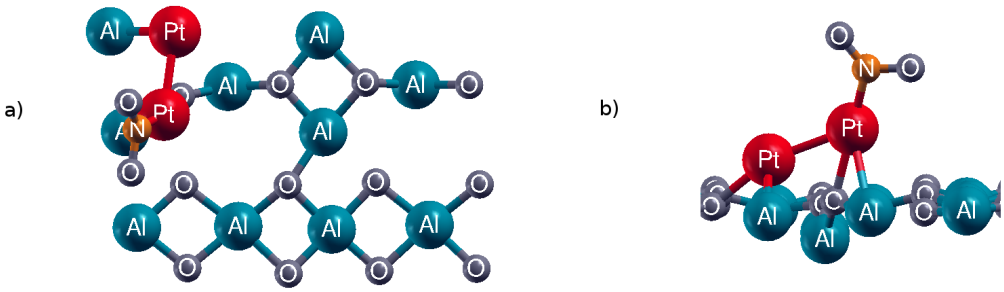

Figure 4.68: The M type NO_2 molecule adsorption in the NO_2-2Pt-Al(1)-B1-(2) configuration, (a) top and (b) side views of the final geometry

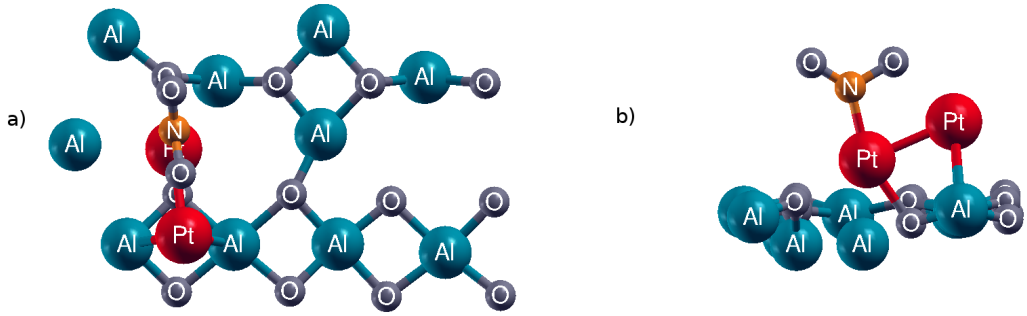

Figure 4.69: The B2 type bridging type NO_2 molecule adsorption in the NO_2-2Pt-Al(3)-B(2)-(1) configuration, (a) top and (b) side views of the final geometry

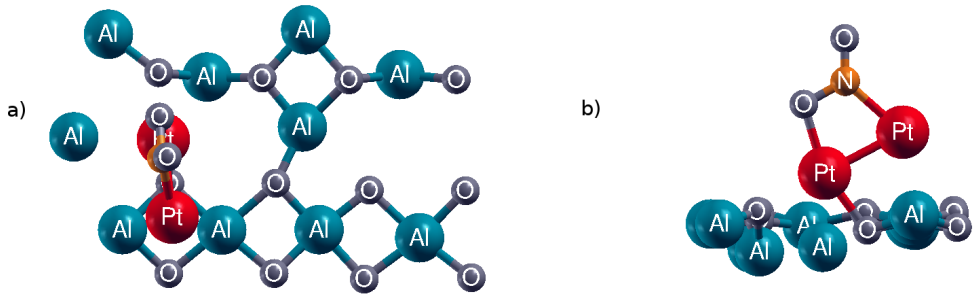

Figure 4.70: The B2 type bridging type NO_2 molecule adsorption in the NO_2-2Pt-Al(3)-B(2)-(2) configuration, (a) top and (b) side views of the final geometry

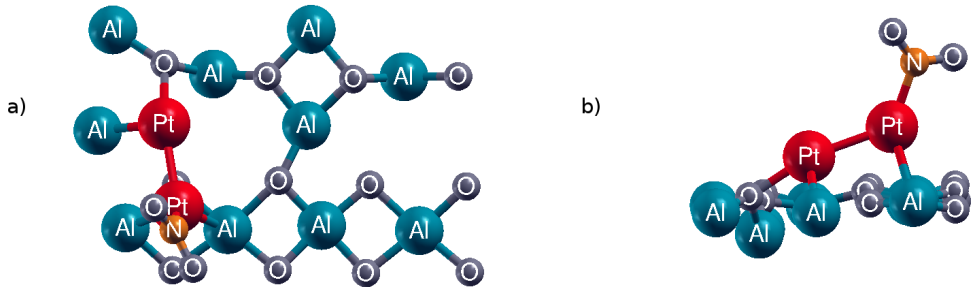

Figure 4.71: The M type type NO_2 molecule adsorption in the NO_2-2Pt-Al(3)-B(2)-(3) configuration, (a) top and (b) side views of the final geometry

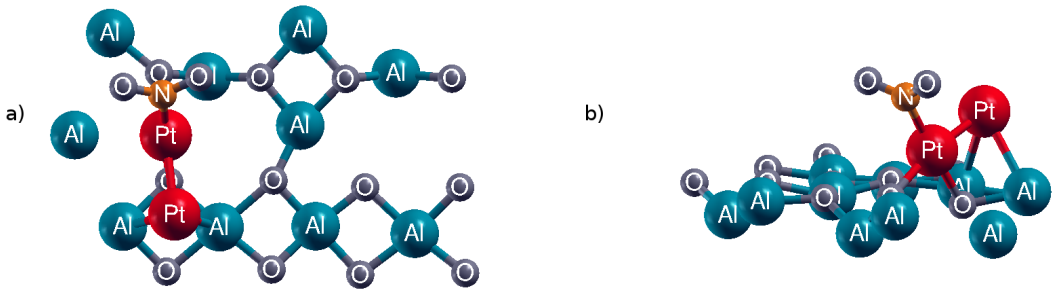

Figure 4.72: The M type type NO_2 molecule adsorption in the NO_2-2Pt-Al(3)-B(2)-(4) configuration, (a) top and (b) side views of the final geometry

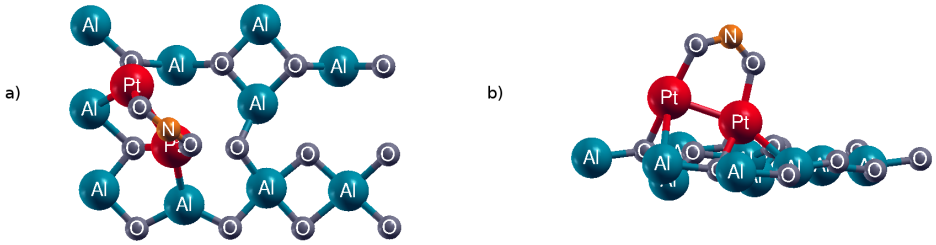

Figure 4.73: The B1 type bridging type NO_2 molecule adsorption in the NO_2-2Pt-Al(4)-E1-(1) configuration, (a) top and (b) side views of the final geometry

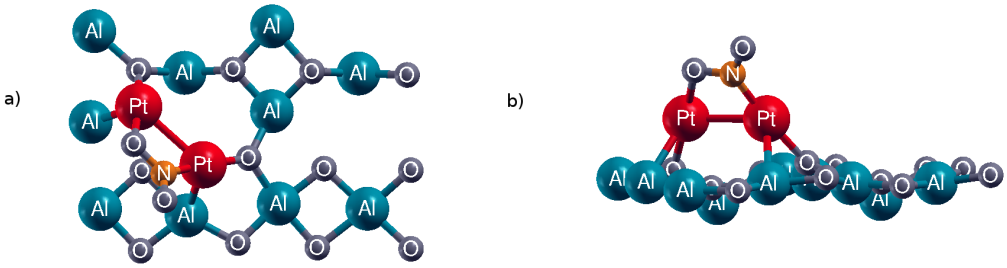

Figure 4.74: The B2 type bridging type NO_2 molecule adsorption in the NO_2-2Pt-Al(4)-E1-(2) configuration, (a) top and (b) side views of the final geometry

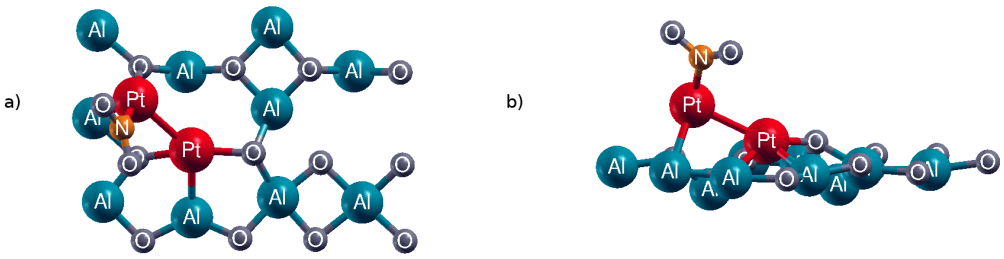

Figure 4.75: The M type NO_2 molecule adsorption in the NO_2-2Pt-Al(4)-E1-(3) configuration, (a) top and (b) side views of the final geometry

Table 4.16: The final geometries and the adsorption energies of the relaxed NO_2+2Pt/γ-Al_2O_3(100) configurations

Configuration	Description	Angle of NO_2	E_{ads}
NO_2-2Pt-Al(1)-B1-(1)	Bridged to Pt atoms	119^o	-3.83
NO_2-2Pt-Al(1)-B1-(2)	Bridged to Pt atoms	117^o	-4.00
NO_2-2Pt-Al(1)-B1-(3)	Bridged to Pt atoms	119^o	-3.99
NO_2-2Pt-Al(1)-B2-(1)	Bridged to Pt atoms	117^o	-2.84
NO_2-2Pt-Al(1)-B2-(2)	monodentate on Pt(2)	125^o	-2.85
NO_2-2Pt-Al(3)-B(2)-(1)	monodentate on Pt(1)	118^o	-2.39
NO_2-2Pt-Al(3)-B(2)-(2)	Bridged to Pt atoms	119^o	-2.13
NO_2-2Pt-Al(3)-B(2)-(3)	monodentate on Pt(2)	126^o	-1.94
NO_2-2Pt-Al(3)-B(2)-(4)	monodentate on Pt(1)	126^o	-2.18
NO_2-2Pt-Al(4)-E2-(1)	Bridged to Pt atoms	120^o	-2.88
NO_2-2Pt-Al(4)-E2-(2)	Bridged to Pt atoms	118^o	-3.51
NO_2-2Pt-Al(4)-E2-(3)	monodentate on Pt(2)	124^o	-2.85

Table 4.17: The bond distances (Å) of fully relaxed NO_2+2Pt/γ-Al_2O_3(100) configurations

Configuration	N-Pt	N-O_{NO_2}	Pt-O_{NO_2}	Pt-Pt
NO_2-2Pt-Al(1)-B1-(1)	-	1.28 and 1.29	Pt(1)-O_{NO_2} 2.05 Pt(2)-O_{NO_2} 2.02	2.59
NO_2-2Pt-Al(1)-B1-(2)	Pt(1)-N 1.97	1.21 and 1.36	Pt(2)-O_{NO_2} 2.03	2.58
NO_2-2Pt-Al(1)-B1-(3)	Pt(2)-N 1.97	1.21 and 1.35	Pt(1)-O_{NO_2} 2.05	2.56
NO_2-2Pt-Al(1)-B2-(1)	Pt(2)-N 1.96	1.21 and 1.36	Pt(1)-O_{NO_2} 2.04	2.61
NO_2-2Pt-Al(1)-B2-(2)	Pt(2)-N 1.94	1.27 and 1.23	-	2.56
NO_2-2Pt-Al(3)-B(2)-(1)	Pt(1)-N 1.96	1.22 and 1.33	-	2.52
NO_2-2Pt-Al(3)-B(2)-(2)	Pt(2)-N 2.20	1.21 and 1.31	Pt(1)-O_{NO_2} 2.04	2.51
NO_2-2Pt-Al(3)-B(2)-(3)	Pt(2)-N 1.97	1.23 and 1.25	-	2.56
NO_2-2Pt-Al(3)-B(2)-(4)	Pt(1)-N 2.01	1.24 and 1.24	-	2.49
NO_2-2Pt-Al(4)-E2-(1)	-	1.28 and 1.29	Pt(1)-O_{NO_2} 2.04 Pt(2)-O_{NO_2} 2.09	2.58
NO_2-2Pt-Al(4)-E2-(2)	Pt(2)-N 1.97	1.22 and 1.34	Pt(1)-O_{NO_2} 2.02	2.77
NO_2-2Pt-Al(4)-E2-(3)	Pt(1)-N 1.97	1.24 and 1.25	-	2.72

We had nearly twenty number of the stable NO_2+2Rh/γ-Al_2O_3(100) configurations shown in Table 4.18. The most remarkable observation of the calculations of all the NO_2-2Rh/γ-Al_2O_3(100) configurations belonged to a configuration which became to the B2 type bridging geometry from a monodentate geometry after calculations. There were five monodentate calculations that became the B2 type bridging geometry and these configurations were specified with the star sign (*) in Table 4.18 and Table 4.19. By this geometric changes, the total number of configurations which had the B2 type bridging geometry after relaxation increased to eight numbers of configurations, by this way, the B2 type bridging configurations became the

dominant geometry among all the NO_2-2Rh/γ-Al_2O_3(100) calculations. In addition, other configurations managed to keep their initial geometries except the NO_2-2Rh-Al(4)-E(3)-2 configuration which was the B1 type bridging configuration (Fig. 4.93). Similar to the NO_2-2Pt-Al(1)-B2-(1) and NO_2-2Pt-Al(3)-B(2)-(2) configurations, in the NO_2-2Rh-Al(4)-E(3)-(1) configuration, the Rh(2) atom left the surface and kept the bonds with the Rh(1) and O_{NO_2} atoms (Fig. 4.92). The adsorption energy of the NO_2 molecule was found to be -3.18 eV and it was the lowest among all the bridging types (B1 and B2 types) configurations. The strongest adsorption of the NO_2 molecule belonged to the B2 type bridging configuration, the NO_2-2Rh-Al(3)-B(2)-(2) configuration (Fig. 4.80), with -4.25 eV and the weakest adsorption of the NO_2 molecule belonged to the NO_2-2Rh-Al(2)-E(3) configuration (Fig. 4.86) having M type geometry, with -2.74 eV.

According to the bond distance analysis, similar the NO_2+2Pt/γ-Al_2O_3(100) configurations, the bond distance between the N atom and O_{NO_2} atom which also bonded to Rh atom was larger than the distance of the N-O_{NO_2} for the B2 type bridging geometries. The largest bond formed between the N and Rh atom was found to be 1.96 Å and it belonged to the NO_2-2Rh-Al(3)-B(1)-(2) configuration which was the one of the B2 type configurations (Fig. 4.88). The shortest bond distance of N-Rh atoms was 1.90 Å and it was observed at a monodentate configuration, the NO_2-2Rh-Al(2)-E(2)-(2) configuration (Fig. 4.85). Furthermore, the range of the bond distances of the Rh-Rh atoms was between 2.33 Å and 2.50 Å.

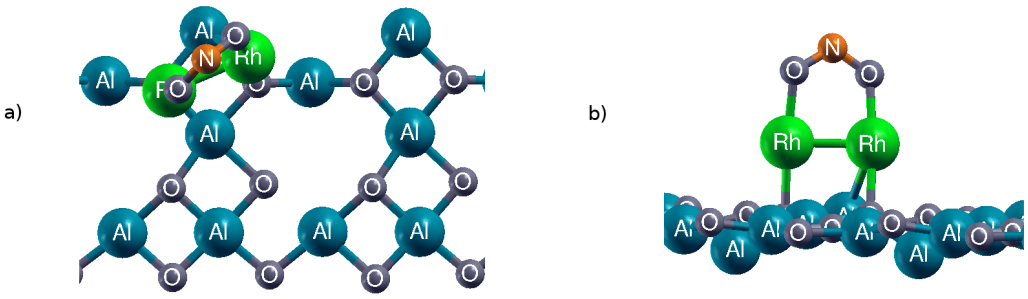

Figure 4.76: The bridging type NO_2 molecule adsorption in the NO_2-2Rh-Al(1)-B(1)-(1) configuration, (a) top and (b) side views of the final geometry

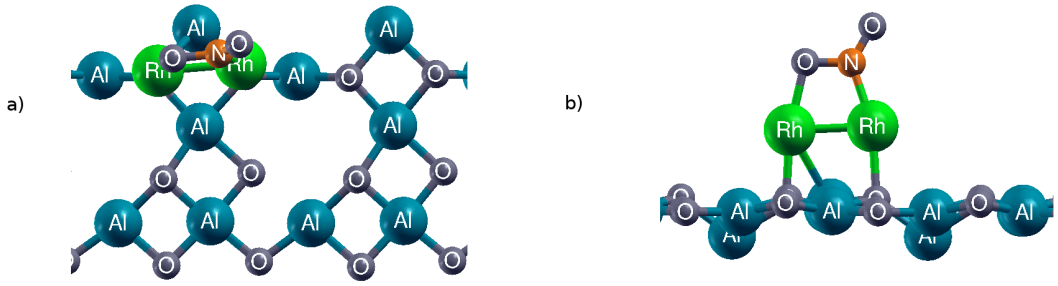

Figure 4.77: The bridging type NO_2 molecule adsorption in the NO_2-2Rh-Al(1)-B(1)-(2) configuration, (a) top and (b) side views of the final geometry

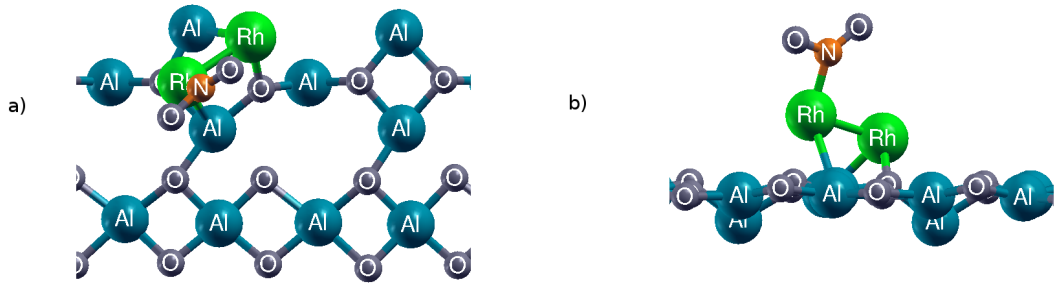

Figure 4.78: The bridging type NO_2 molecule adsorption in the NO_2-2Rh-Al(1)-B(1)-(3) configuration, (a) top and (b) side views of the final geometry

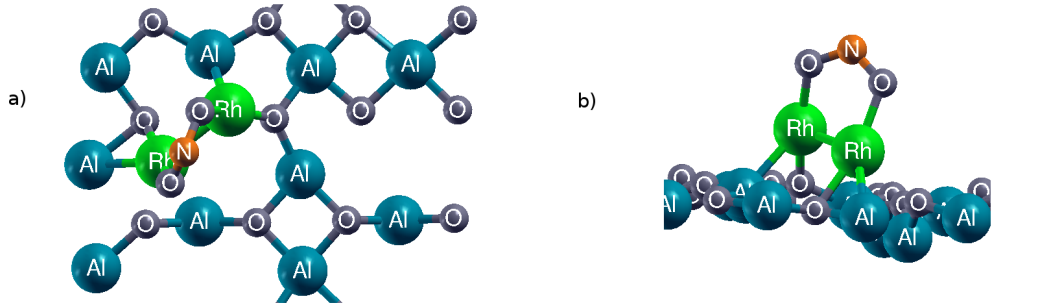

Figure 4.79: The bridging type NO_2 molecule adsorption in the NO_2-2Rh-Al(1)-B(2)-(1) configuration, (a) top and (b) side views of the final geometry

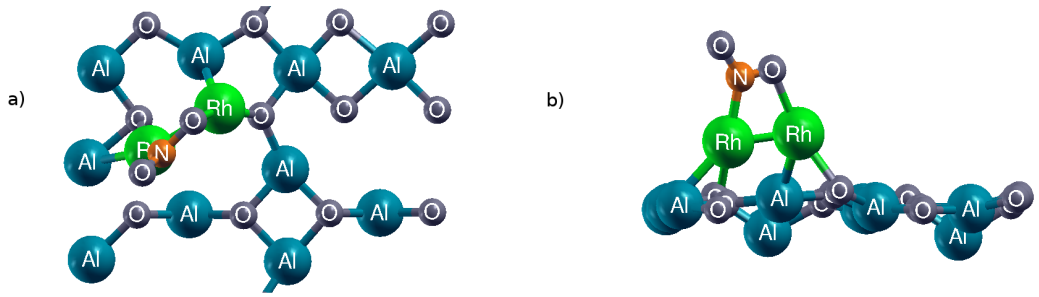

Figure 4.80: The bridging type NO_2 molecule adsorption in the NO_2-2Rh-Al(1)-B(2)-(2) configuration, (a) top and (b) side views of the final geometry

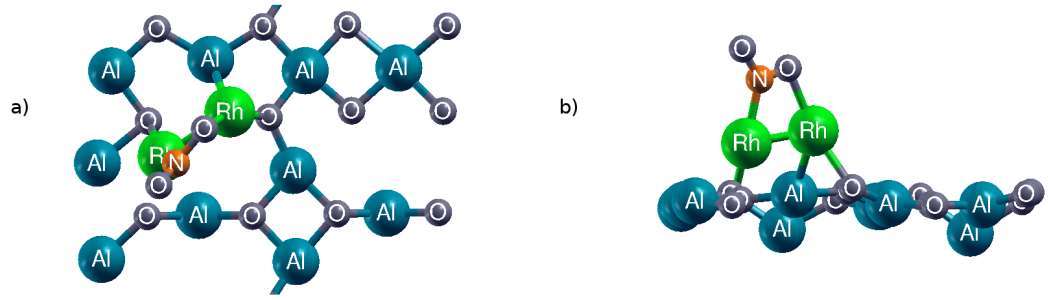

Figure 4.81: The bridging type NO_2 molecule adsorption in the NO_2-2Rh-Al(1)-B(2)-(3) configuration, (a) top and (b) side views of the final geometry

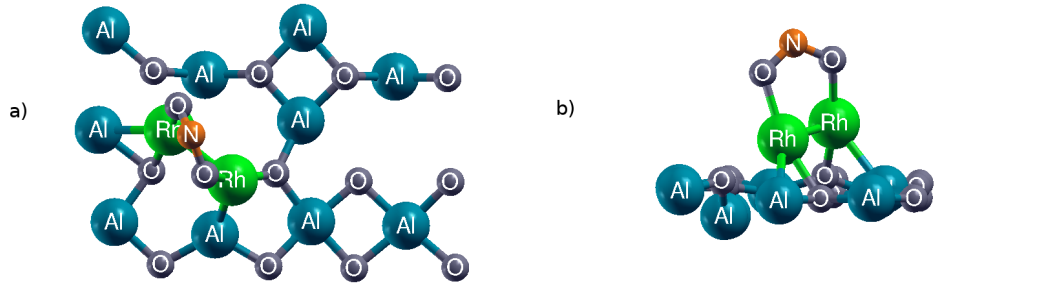

Figure 4.82: The bridging type NO_2 molecule adsorption in the NO_2-2Rh-Al(2)-E(1)-(1) configuration, (a) top and (b) side views of the final geometry

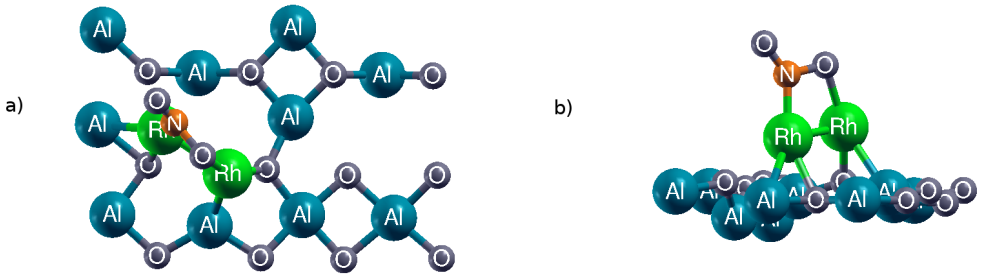

Figure 4.83: The bridging type NO_2 molecule adsorption in the NO_2-2Rh-Al(2)-E(1)-(2) configuration, (a) top and (b) side views of the final geometry

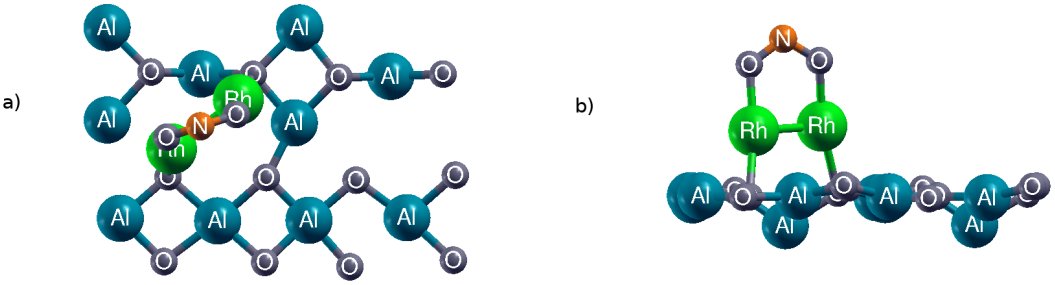

Figure 4.84: The bridging type NO_2 molecule adsorption in the NO_2-2Rh-Al(2)-E(2)-(1) configuration, (a) top and (b) side views of the final geometry

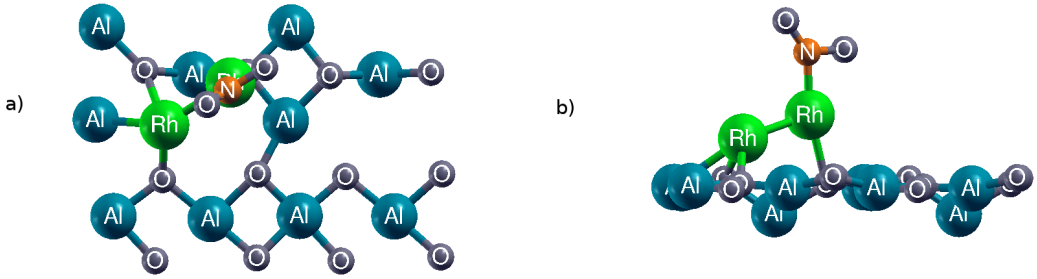

Figure 4.85: The bridging type NO_2 molecule adsorption in the NO_2-2Rh-Al(2)-E(2)-(2) configuration, (a) top and (b) side views of the final geometry

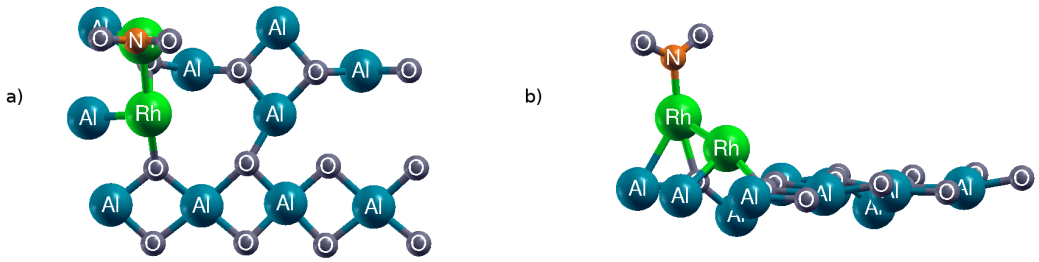

Figure 4.86: The bridging type NO_2 molecule adsorption in the NO_2-2Rh-Al(2)-E(3) configuration, (a) top and (b) side views of the final geometry

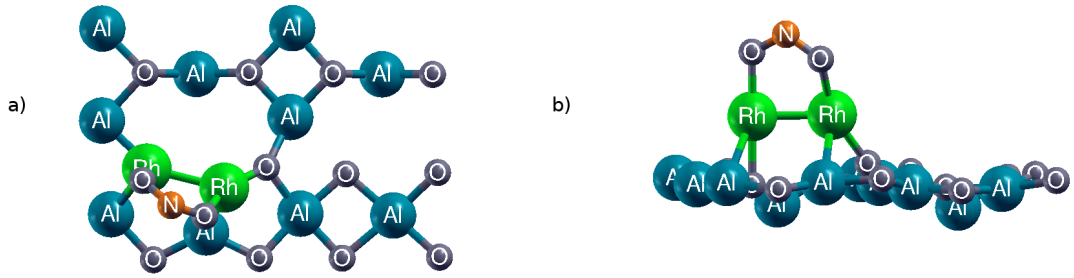

Figure 4.87: The bridging type NO_2 molecule adsorption in the NO_2-2Rh-Al(3)-B(1)-(1) configuration, (a) top and (b) side views of the final geometry

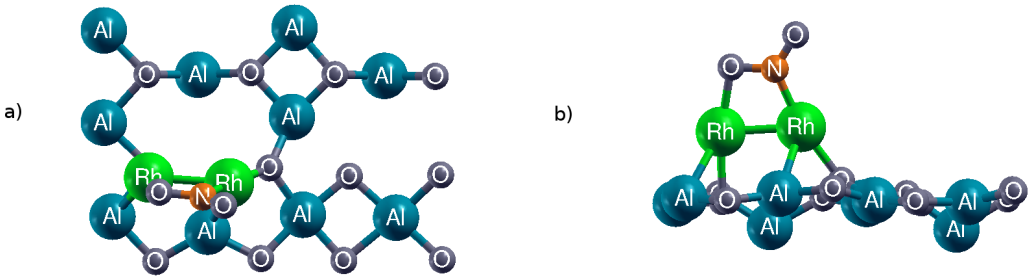

Figure 4.88: The bridging type NO_2 molecule adsorption in the NO_2-2Rh-Al(3)-B(1)-(2) configuration, (a) top and (b) side views of the final geometry

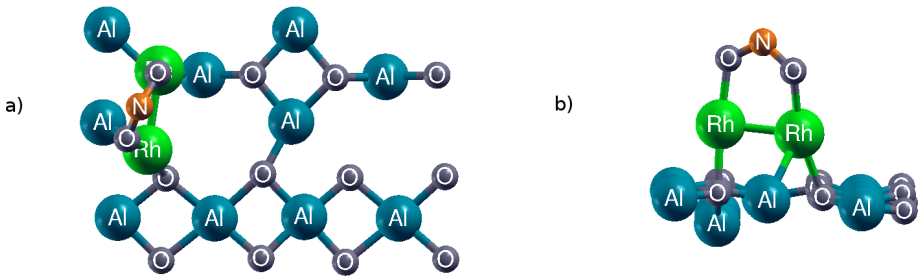

Figure 4.89: The bridging type NO_2 molecule adsorption in the NO_2-2Rh-Al(3)-B(2)-(1) configuration, (a) top and (b) side views of the final geometry

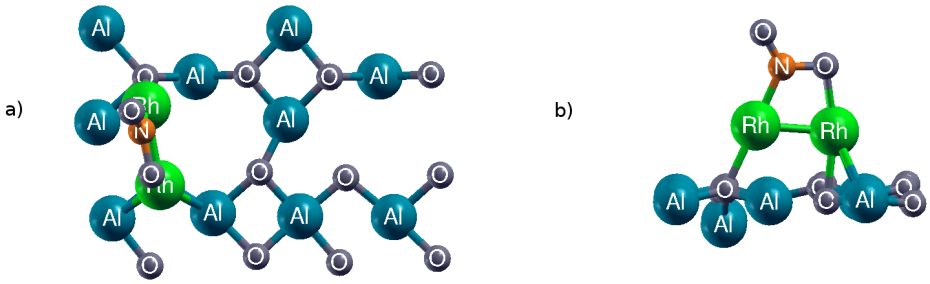

Figure 4.90: The bridging type NO_2 molecule adsorption in the NO_2-2Rh-Al(3)-B(2)-(2) configuration, (a) top and (b) side views of the final geometry

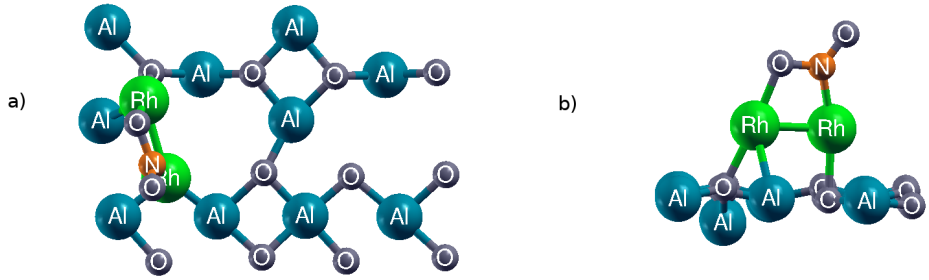

Figure 4.91: The bridging type NO_2 molecule adsorption in the NO_2-2Rh-Al(3)-B(2)-(3) configuration, (a) top and (b) side views of the final geometry

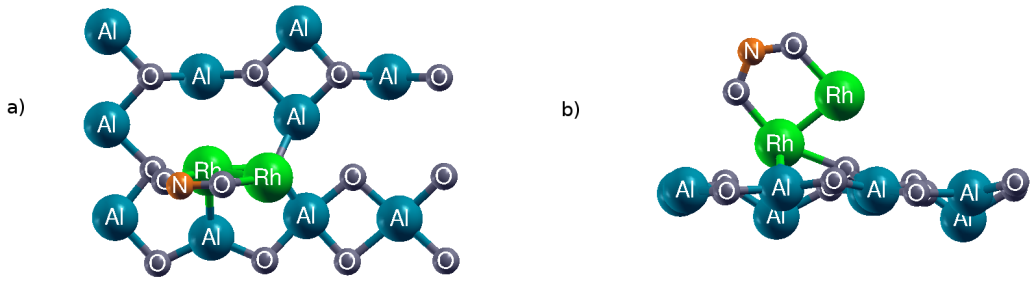

Figure 4.92: The bridging type NO_2 molecule adsorption in the NO_2-2Rh-Al(3)-E(3)-1 configuration, (a) top and (b) side views of the final geometry

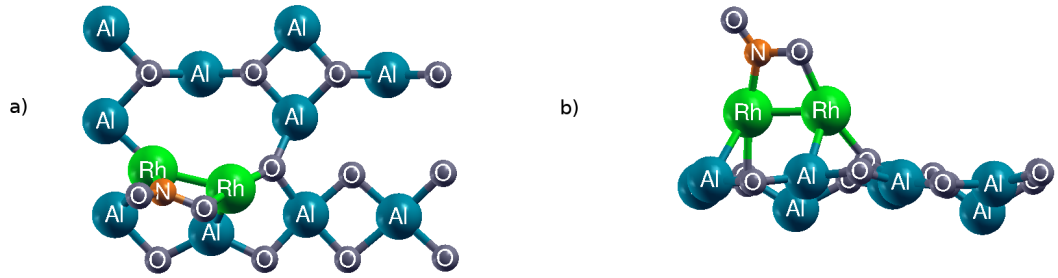

Figure 4.93: The bridging type NO_2 molecule adsorption inthe NO_2-2Rh-Al(3)-E(3)-2 configuration, (a) top and (b) side views of the final geometry

Table 4.18: The final geometries and the adsorption energies of the relaxed NO_2+2Rh/γ-Al_2O_3(100) configurations

Configuration	Description	Angle of NO_2	E_{ads}
NO_2-2Rh-Al(1)-B(1)-(1)	Bridged to Rh atoms	116^o	-3.87
NO_2-2Rh-Al(1)-B(1)-(2)*	Bridged to Rh atoms	119^o	-4.13
NO_2-2Rh-Al(1)-B(1)-(3)	monodentate on Rh(2)	125^o	-3.27
NO_2-2Rh-Al(1)-B(2)-(1)	Bridged to Rh atoms	116^o	-3.28
NO_2-2Rh-Al(1)-B(2)-(2)	Bridged to Rh atoms	119^o	-3.42
NO_2-2Rh-Al(1)-B(2)-(3)*	Bridged to Rh atoms	119^o	-3.40
NO_2-2Rh-Al(2)-E(1)-(1)	Bridged to Rh atoms	116^o	-3.28
NO_2-2Rh-Al(2)-E(1)-(2)*	Bridged to Rh atoms	119^o	-3.40
NO_2-2Rh-Al(2)-E(2)-(1)	Bridged to Rh atoms	114^o	-3.66
NO_2-2Rh-Al(2)-E(2)-(2)	monodentate on Rh(2)	119^o	-3.17
NO_2-2Rh-Al(2)-E(3)	monodentate on Rh(2)	125^o	-2.74
NO_2-2Rh-Al(3)-B(1)-(1)	Bridged to Rh atoms	115^o	-3.66
NO_2-2Rh-Al(3)-B(1)-(2)*	Bridged to Rh atoms	120^o	-3.91
NO_2-2Rh-Al(3)-B(2)-(1)	Bridged to Rh atoms	115^o	-3.72
NO_2-2Rh-Al(3)-B(2)-(2)	Bridged to Rh atoms	119^o	-4.35
NO_2-2Rh-Al(3)-B(2)-(3)*	Bridged to Rh atoms	120^o	-4.24
NO_2-2Rh-Al(4)-E(3)-(1)	Bridged to Rh atoms	118^o	-3.18
NO_2-2Rh-Al(4)-E(3)-(2)	Bridged to Rh atoms	120^o	-3.87

Table 4.19: The bond distances (Å) of the relaxed NO_2+2Rh/γ-Al_2O_3(100) configurations

Configuration	N-Rh	N-O_{NO_2}	Rh-O_{NO_2}	Rh-Rh
NO_2-2Rh-Al(1)-B(1)-(1)	-	1.29 and 1.29	Rh(1)-O_{NO_2} 2.02 Rh(2)-O_{NO_2} 2.02	2.39
NO_2-2Rh-Al(1)-B(1)-(2)*	Rh(1)-N 1.94	1.23 and 1.34	Rh(2)-O_{NO_2} 2.02	2.40
NO_2-2Rh-Al(1)-B(1)-(3)	Rh(2)-N 1.91	1.23 and 1.28	-	2.47
NO_2-2Rh-Al(1)-B(2)-(1)	-	1.29 and 1.30	Rh(1)-O_{NO_2} 2.03 Rh(2)-O_{NO_2} 2.03	2.39
NO_2-2Rh-Al(1)-B(2)-(2)	Rh(1)-N 1.93	1.22 and 1.35	Rh(2)-O_{NO_2} 2.06	2.41
NO_2-2Rh-Al(1)-B(2)-(3)*	Rh(1)-N 1.94	1.22 and 1.36	Rh(2)-O_{NO_2} 2.06	2.41
NO_2-2Rh-Al(2)-E(1)-(1)	-	1.29 and 1.31	Rh(1)-O_{NO_2} 2.03 Rh(2)-O_{NO_2} 2.03	2.39
NO_2-2Rh-Al(2)-E(1)-(2)*	Rh(1)-N 1.94	1.22 and 1.36	Rh(2)-O_{NO_2} 2.06	2.41
NO_2-2Rh-Al(2)-E(2)-(1)	-	1.29 and 1.31	Rh(1)-O_{NO_2} 1.99 Rh(2)-O_{NO_2} 1.99	2.46
NO_2-2Rh-Al(2)-E(2)-(2)	Rh(2)-N 1.90	1.22 and 1.30	-	2.47
NO_2-2Rh-Al(2)-E(3)-(1)	Rh(2)-N 1.94	1.25 and 1.25	-	2.50
NO_2-2Rh-Al(3)-B(1)-(1)	-	1.28 and 1.29	Rh(1)-O_{NO_2} 2.00 Rh(2)-O_{NO_2} 2.02	2.41
NO_2-2Rh-Al(3)-B(1)-(2)*	Rh(2)-N 1.96	1.22 and 1.33	Rh(1)-O_{NO_2} 2.01	2.43
NO_2-2Rh-Al(3)-B(2)-(1)	-	1.28 and 1.30	Rh(1)-O_{NO_2} 2.01 Rh(2)-O_{NO_2} 2.00	2.42
NO_2-2Rh-Al(3)-B(2)-(2)	Rh(2)-N 1.95	1.22 and 1.35	Rh(1)-O_{NO_2} 2.01	2.42
NO_2-2Rh-Al(3)-B(2)-(3)*	Rh(1)-N 1.95	1.22 and 1.34	Rh(2)-O_{NO_2} 2.03	2.41
NO_2-2Rh-Al(4)-E(3)-(1)	-	1.28 and 1.30	Rh(1)-O_{NO_2} 2.05 Rh(2)-O_{NO_2} 2.05	2.33
NO_2-2Rh-Al(4)-E(3)-(2)	Rh(1)-N 1.94	1.22 and 1.34	Rh(1)-O_{NO_2} 2.03	2.40

For the NO_2 adsorption on the Rh+Pt/γ-Al_2O_3(100) and Pt+Rh/γ-Al_2O_3(100) configurations, only bridging configurations were calculated since most of the monodentate configurations mentioned previously show a tendency to become bridging configurations. For this reason, only the bridging types configurations (B1 and B2 types) were used for calculations in this section.

Based on the configurations in Table 4.8, the NO_2 molecule was added to these configurations. Most of the these configurations exhibited no considerable changes during calculations, however, distinguishable changes were observed for three of NO_2-Rh+Pt-Al(1)-B1 configurations and NO_2-Rh+Pt-Al(4)-E1-(1) configurations. The NO_2-Rh+Pt-Al(1)-B1-(1) and NO_2-Rh+Pt-Al(1)-B1-(3) configurations exhibited similar change, although they were different types bridging configuration initially. After the calculation, the Pt atom on the sur-

face broke its bonds with the surface but the NO_2 molecules managed to keep their bridging configurations on Rh and Pt atoms (Fig. 4.94 and Fig. 4.96). The adsorption energies of these configurations were found to be -2.62 eV and -3.10 eV for the NO_2-Rh+Pt-Al(1)-B1-(1) and NO_2-Rh+Pt-Al(1)-B1-(3) configurations respectively and the NO_2-Rh+Pt-Al(1)-B1-(1) configuration showed the weakest adsorption among all the NO_2-Rh+Pt/γ-Al_2O_3(100) configurations. The changes in the NO_2-Rh+Pt-Al(4)-E1-(1) configuration was observed previously for the NO_2-2Pt-Al(3)-B(2)-(1) configuration. The NO_2 molecules was placed on the surface in the B2 type bridging configuration but at the end of the calculation the configuration had a monodandate configuration on the Rh atom and the Rh atom broke its bonds with the surface atoms while it kept its bonds with the Pt and N atoms (Fig. 4.106). Eventhough the final geometry of this configuration was seemed to be different, the NO_2 molecule was adsorbed well on the surface since the adsorption energy of the NO_2 molecule was found to be -3.17 eV. The last configuration, for the NO_2-Rh+Pt-Al(1)-B1-(2) configuration, unexpected changes in the geometry was observed. The NO_2 molecule was placed in the configuration in the B2 type bridging configuration initially but after relaxation the configuration became a completely different geometry. The Pt atom left the surface and due to the attraction between the O_{NO_2} and the Al(3) atom, the NO_2 molecule moved towards the Al(3) atom and finally a bond between O_{NO_2}-Al(3) atoms was formed. the bond distance of the O_{NO_2}-Al(3) atoms was found to be 2.02 Å (Fig. 4.95). This configuration could not be taken account as a bridging geometry on the bimetalics but the adsorption energy of the NO_2 molecule was -3.58 eV which was seemed to be reasonable. The highest adsorption energy of the NO_2 molecule belonged to the NO_2-Rh+Pt-Al(3)-B(2)-(3) configuration, named -4.74 eV.

According to Table 4.21, the range of the bond distances between Rh-N atoms was between 1.88 Å and 1.93 Å and the range of the bond distances between Pt-N atoms was between 1.92 Å and 2.03 Å. It was seen obviously in Table 4.21 that the bond distances of the Rh and N atoms were shorter than the bond distances of the Pt and N atoms. Moreover, the bond distances of the O_{NO_2} atom with the Rh and Pt atoms were close to each other. The most important observation in the bond distances claimed that the bond distances between the N and O_{NO_2} atom were larger when the same O_{NO_2} atom also bonded to the Pt atom in the B2 type bridging configurations. The range of the bond distances of the Rh-Pt atoms was between the 2.46 Å and 2.67 Å and the longest bond between the Rh and Pt atom was observed in the

NO_2-Rh+Pt-Al(4)-E1-(1) configuration which was the only one monodentate configuration.

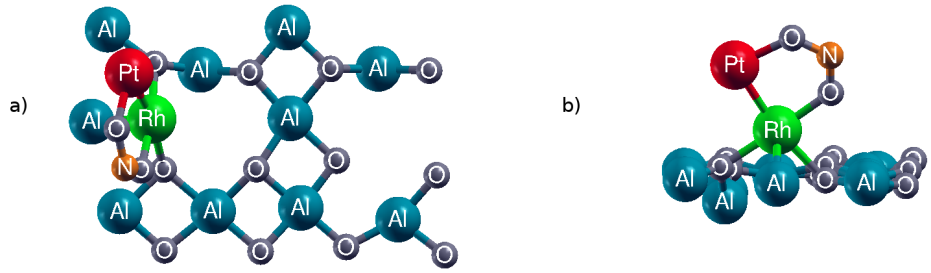

Figure 4.94: The B1 type bridging adsorption of the NO_2 molecule in the NO_2-Rh+Pt-Al(1)-B-(1) configuration, (a) top and (b) side views of the final geometry

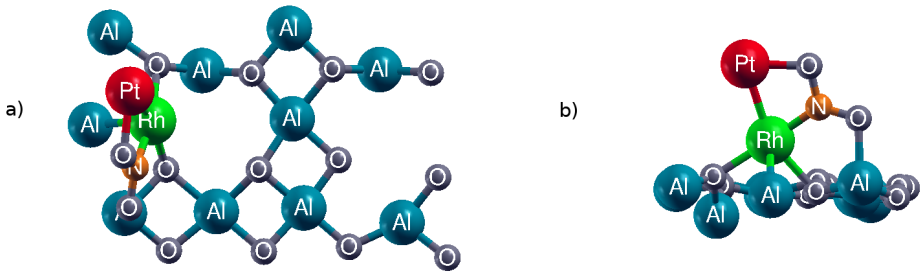

Figure 4.95: The B2 type bridging adsorption of the NO_2 molecule in the NO_2-Rh+Pt-Al(1)-B-(2) configuration, (a) top and (b) side views of the final geometry

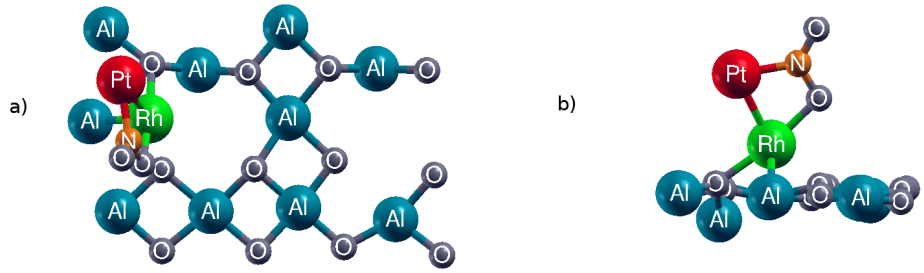

Figure 4.96: The B2 type bridging adsorption of the NO_2 molecule in the NO_2-Rh+Pt-Al(1)-B-(3) configuration, (a) top and (b) side views of the final geometry

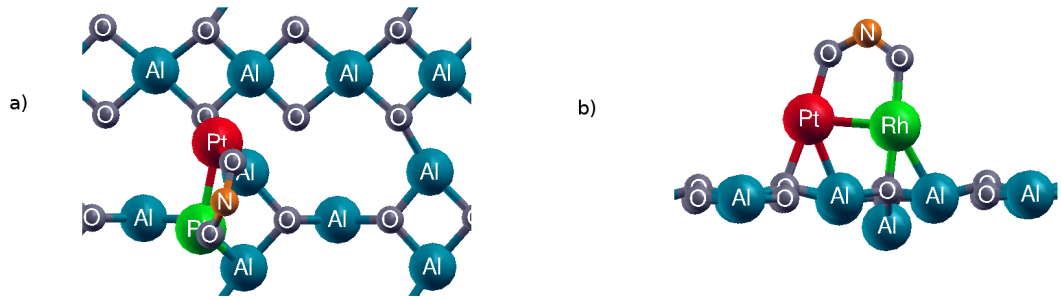

Figure 4.97: The B1 type bridging adsorption of the NO_2 molecule in the NO_2-Rh+Pt-Al(1)-B1-(1) configuration, (a) top and (b) side views of the final geometry

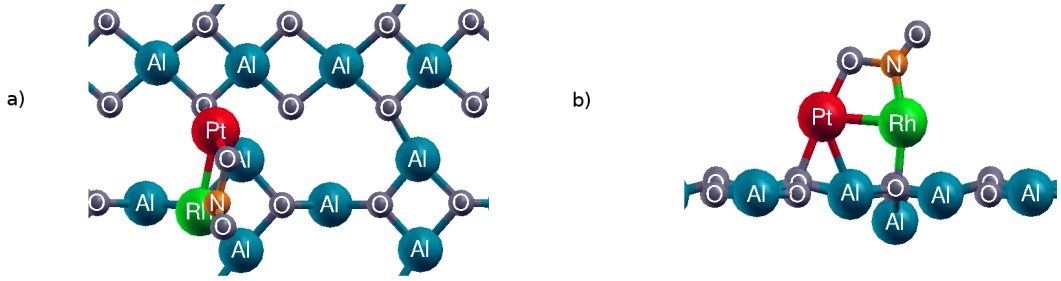

Figure 4.98: The B2 type bridging adsorption of the NO_2 molecule in the NO_2-Rh+Pt-Al(1)-B1-(2) configuration, (a) top and (b) side views of the final geometry

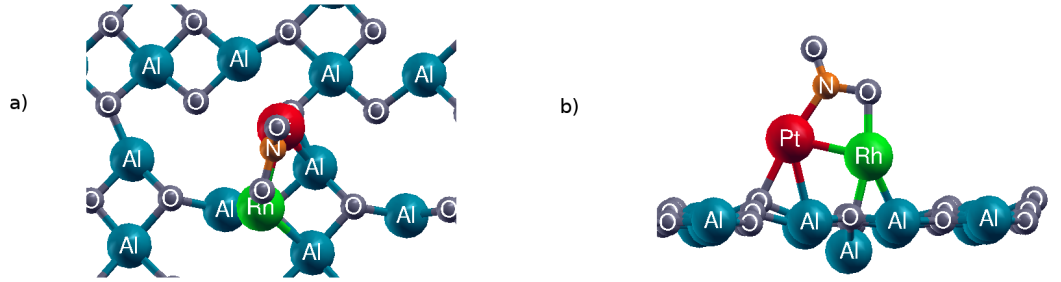

Figure 4.99: The B2 type bridging adsorption of the NO_2 molecule in the NO_2-Rh+Pt-Al(1)-B1-(3) configuration, (a) top and (b) side views of the final geometry

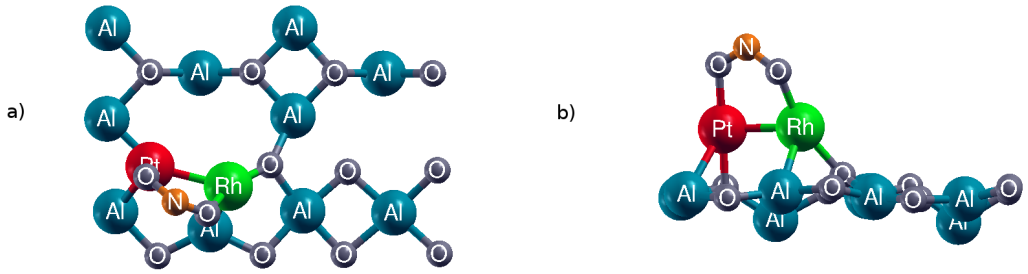

Figure 4.100: The B1 type bridging adsorption of the NO_2 molecule in the NO_2-Rh+Pt-Al(3)-B(1)-(1) configuration, (a) top and (b) side views of the final geometry

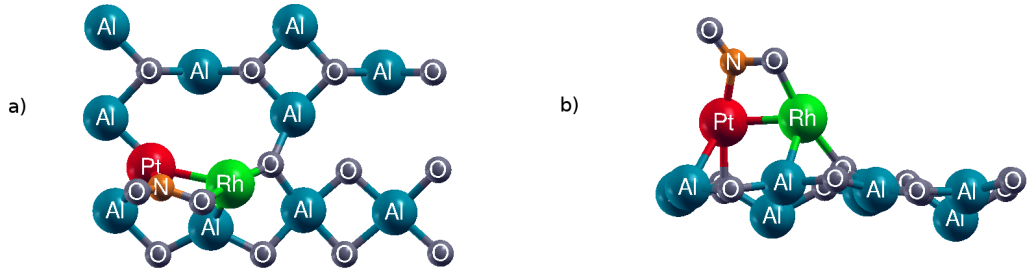

Figure 4.101: The B2 type bridging adsorption of the NO_2 molecule in the NO_2-Rh+Pt-Al(3)-B(1)-(2) configuration, (a) top and (b) side views of the final geometry

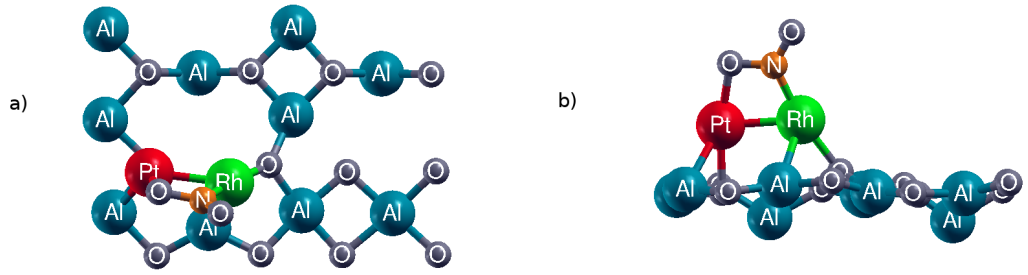

Figure 4.102: The B2 type bridging adsorption of the NO_2 molecule in the NO_2-Rh+Pt-Al(3)-B(1)-(3) configuration, (a) top and (b) side views of the final geometry

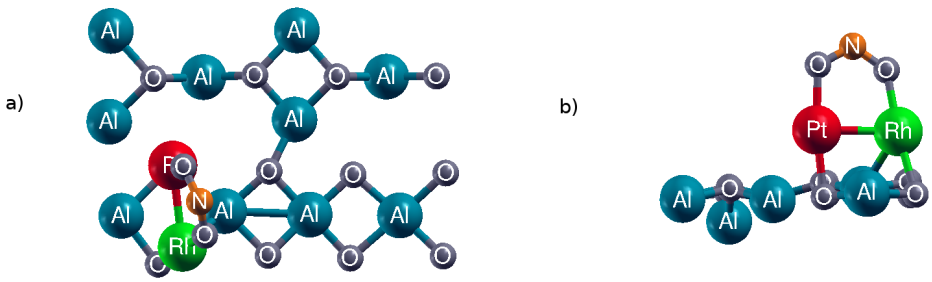

Figure 4.103: The B1 type bridging adsorption of the NO_2 molecule in the NO_2-Rh+Pt-Al(3)-B(1)-(1) configuration, (a) top and (b) side views of the final geometry

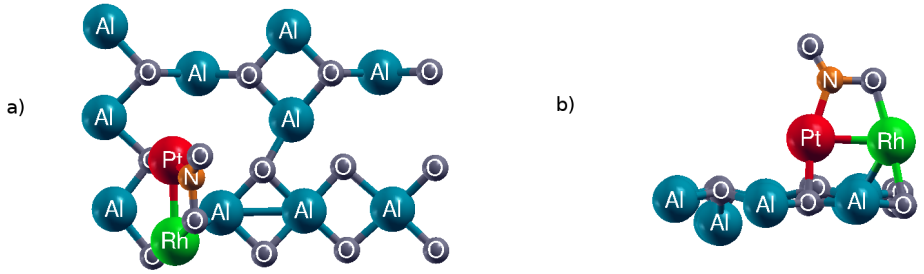

Figure 4.104: The B2 type bridging adsorption of the NO_2 molecule in the NO_2-Rh+Pt-Al(3)-B(2)-(2) configuration, (a) top and (b) side views of the final geometry

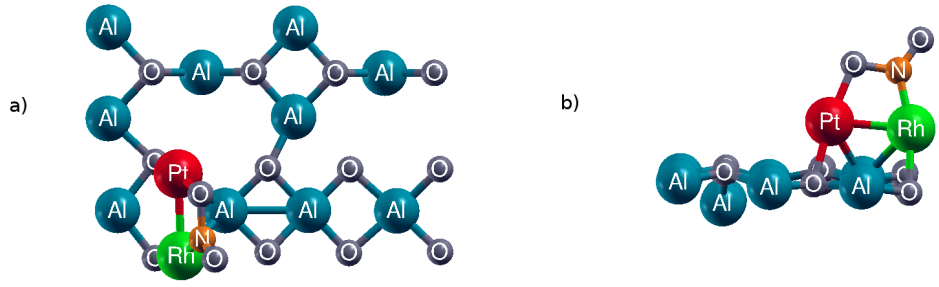

Figure 4.105: The B2 type bridging adsorption of the NO_2 molecule in the NO_2-Rh+Pt-Al(3)-B(2)-(3) configuration, (a) top and (b) side views of the final geometry

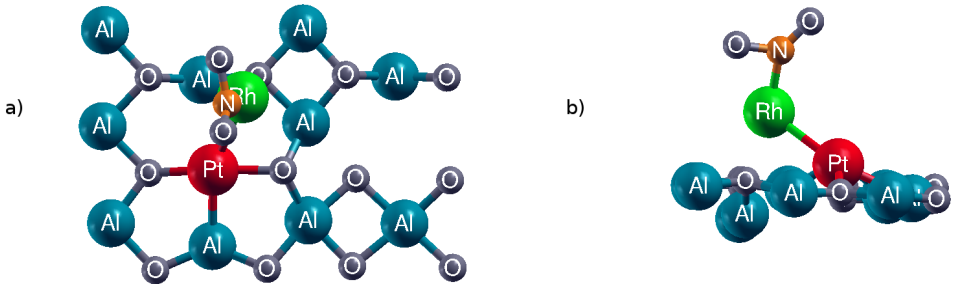

Figure 4.106: The M type adsorption of the NO_2 molecule in the NO_2-Rh+Pt-Al(4)-E(1)-(1) configuration, (a) top and (b) side views of the final geometry

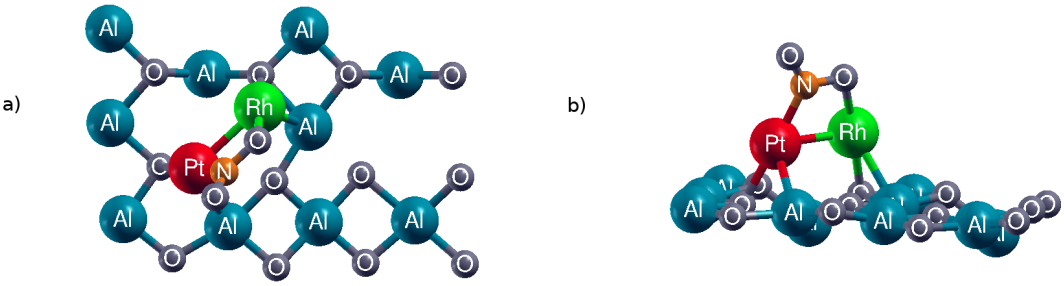

Figure 4.107: The B2 type bridging adsorption of the NO_2 molecule in the NO_2-Rh+Pt-Al(4)-E(1)-(2) configuration, (a) top and (b) side views of the final geometry

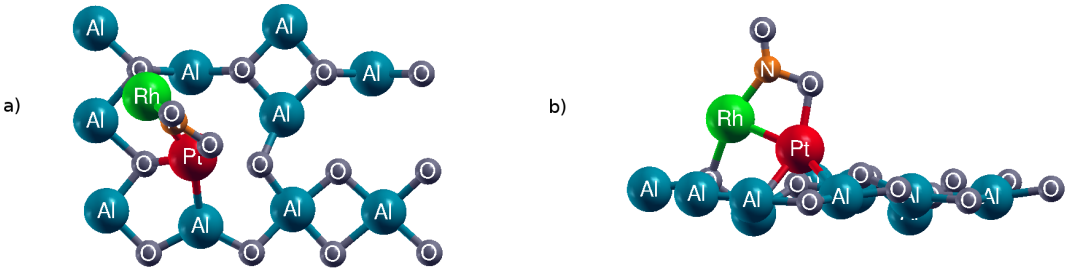

Figure 4.108: The B2 type bridging adsorption of the NO_2 molecule in the NO_2-Rh+Pt-Al(4)-E(2)-(1) configuration, (a) top and (b) side views of the final geometry

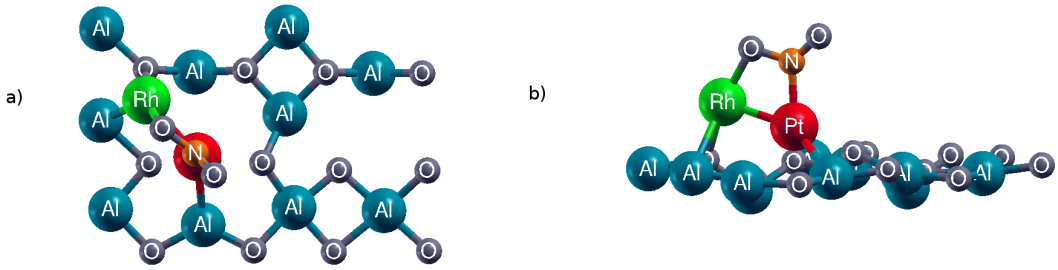

Figure 4.109: The B2 type bridging adsorption of the NO_2 molecule in the NO_2-Rh+Pt-Al(4)-E(2)-(2) configuration, (a) top and (b) side views of the final geometry

Table 4.20: The final geometries and the adsorption energies of the relaxed NO_2+Rh-Pt/γ-Al_2O_3(100) configurations

Configuration	Description	Angle of NO_2	E_{ads}
NO_2-Rh+Pt-Al(1)-B1-(1)	Bridged to Rh and Pt	118^o	-2.62
NO_2-Rh+Pt-Al(1)-B1-(2)	Bridged to Rh, Pt and Al(3)	115^o	-3.58
NO_2-Rh+Pt-Al(1)-B1-(3)	Bridged to Rh and Pt	122^o	-3.10
NO_2-Rh+Pt-Al(1)-B2-(1)	Bridged to Rh and Pt	117^o	-3.36
NO_2-Rh+Pt-Al(1)-B2-(2)	Bridged to Rh and Pt	117^o	-3.88
NO_2-Rh+Pt-Al(1)-B2-(3)	Bridged to Rh and Pt	119^o	-3.62
NO_2-Rh+Pt-Al(3)-B(1)-(1)	Bridged to Rh and Pt	116^o	-4.02
NO_2-Rh+Pt-Al(3)-B(1)-(2)	Bridged to Rh and Pt	120^o	-4.25
NO_2-Rh+Pt-Al(3)-B(1)-(3)	Bridged to Rh and Pt	116^o	-4.25
NO_2-Rh+Pt-Al(3)-B(2)-(1)	Bridged to Rh and Pt	117.5^o	-4.23
NO_2-Rh+Pt-Al(3)-B(2)-(2)	Bridged to Rh and Pt	119^o	-4.49
NO_2-Rh+Pt-Al(3)-B(2)-(3)	Bridged to Rh and Pt	117^o	-4.74
NO_2-Rh+Pt-Al(4)-E1-(1)	Monodentate on Rh	127^o	-3.17
NO_2-Rh+Pt-Al(4)-E1-(2)	Bridged to Rh and Pt	119.5^o	-3.94
NO_2-Rh+Pt-Al(4)-E2-(1)	Bridged to Rh and Pt	116^o	-3.07
NO_2-Rh+Pt-Al(4)-E2-(2)	Bridged to Rh and Pt	120^o	-2.96

Table 4.21: The bond distances (Å) of the the relaxed NO_2-Rh+Pt/γ-Al_2O_3(100) configurations

Configuration	N-Rh	N-Pt	N-O_{NO_2}
NO_2-Rh+Pt-Al(1)-B-(1)	-	-	1.26 and 1.31
NO_2-Rh+Pt-Al(1)-B-(2)	1.88	-	1.28 and 1.34
Rh+Pt-Al(1)-B-(3)	-	1.92	1.22 and 1.31
NO_2-Rh+Pt-Al(1)-B1-(1)	-	-	1.27 and 1.31
NO_2-Rh+Pt-Al(1)-B1-(2)	1.89	-	1.22 and 1.39
NO_2-Rh+Pt-Al(1)-B1-(3)	-	1.97	1.22 and 1.33
NO_2-Rh+Pt-Al(3)-B(1)-(1)	-	-	1.28 and 1.31
NO_2-Rh+Pt-Al(3)-B(1)-(2)	-	1.96	1.22 and 1.33
NO_2-Rh+Pt-Al(3)-B(1)-(3)	1.93	-	1.22 and 1.37
NO_2-Rh+Pt-Al(3)-B(2)-(1)	-	-	1.27 and 1.30
NO_2-Rh+Pt-Al(3)-B(2)-(2)	-	1.96	1.22 and 1.34
NO_2-Rh+Pt-Al(3)-B(2)-(3)	1.91	-	1.22 and 1.39
NO_2-Rh+Pt-Al(4)-E(1)-(1)	1.87	-	1.22 and 1.30
NO_2-Rh+Pt-Al(4)-E(1)-(2)	-	1.97	1.22 and 1.33
NO_2-Rh+Pt-Al(4)-E(2)-(1)	1.93	-	1.22 and 1.39
NO_2-Rh+Pt-Al(4)-E(2)-(2)	-	2.03	1.22 and 1.33

Configuration	Rh-O_{NO_2}	Pt-O_{NO_2}	Rh-Pt
NO_2-Rh+Pt-Al(1)-B-(1)	Rh-O_{NO_2} 2.03	Pt-O_{NO_2} 1.99	2.50
NO_2-Rh+Pt-Al(1)-B-(2)	-	Pt-O_{NO_2} 1.98	2.55
Rh+Pt-Al(1)-B-(3)	Rh-O_{NO_2} 2.04	-	2.55
NO_2-Rh+Pt-Al(1)-B1-(1)	Rh-O_{NO_2} 1.98	Pt-O_{NO_2} 2.02	2.57
NO_2-Rh+Pt-Al(1)-B1-(2)	-	Pt-O_{NO_2} 2.00	2.52
NO_2-Rh+Pt-Al(1)-B1-(3)	Rh-O_{NO_2} 2.00	-	2.52
NO_2-Rh+Pt-Al(3)-B(1)-(1)	Rh-O_{NO_2} 2.02	Pt-O_{NO_2} 2.00	2.48
NO_2-Rh+Pt-Al(3)-B(1)-(2)	Rh-O_{NO_2} 2.03	-	2.48
NO_2-Rh+Pt-Al(3)-B(1)-(3)	-	Pt-O_{NO_2} 2.00	2.48
NO_2-Rh+Pt-Al(3)-B(2)-(1)	Rh-O_{NO_2} 2.02	Pt-O_{NO_2} 2.00	2.51
NO_2-Rh+Pt-Al(3)-B(2)-(2)	Rh-O_{NO_2} 2.03	-	2.48
NO_2-Rh+Pt-Al(3)-B(2)-(3)	-	Pt-O_{NO_2} 2.01	2.51
NO_2-Rh+Pt-Al(4)-E(1)-(1)	-	-	2.67
NO_2-Rh+Pt-Al(4)-E(1)-(2)	Rh-O_{NO_2} 1.98	-	2.61
NO_2-Rh+Pt-Al(4)-E(2)-(1)	-	Pt-O_{NO_2} 2.06	2.46
NO_2-Rh+Pt-Al(4)-E(2)-(2)	Rh-O_{NO_2} 2.01	-	2.47

According to the configurations in Table 4.8, the NO_2 molecule was added to these configurations. Most of the these configurations exhibited no considerable changes during calculations, however, distinguishable changes were observed for some configurations similar to the NO_2-Rh+Pt/γ-Al_2O_3(100) configurations. The NO_2-Pt+Rh-Al(1)-B2(2)-(1), NO_2-Pt+Rh-Al(2)-E, and NO_2-Pt+Rh-Al(3)-B(1)/B(2) configurations did not exhibit remarkable changes during the calculations, however, important changes were observed in the NO_2-Pt+Rh-Al(1)-B2(2)-(2)/(3) and NO_2-Pt+Rh-Al(4)-E(1)/E(2) configurations. Same with the the NO_2-Rh+Pt-Al(1)-B1-(2) configuration, the NO_2-Pt+Rh-Al(1)-B2(2)-(2) configuration exhibited the same manner (Fig. 4.114). The Pt atom left the surface and the NO_2 molecule moved towards to the Al(3) atom and the bond between O_{NO_2}-Al(3) atoms was formed at the end of the calculation. The bond distance of the O_{NO_2}-Al(3) atoms was found to be 2.02 Å which was exactly the same in the NO_2-Rh+Pt-Al(1)-B1-(2) configuration. Different from the NO_2-Rh+Pt-Al(1)-B1-(2) configuration, the adsorption energy of this configuration was found to be -2.89 eV which was lower 0.28 eV than the NO_2-Rh+Pt-Al(1)-B1-(2) configuration's. For the NO_2-Pt+Rh-Al(1)-B1(2)-(3) configuration, the Pt atom broke its bond with the surface and it managed to keep its bonds with the Rh and N atoms. The adsorption energy of this configuration was found to be -3.10 eV. The NO_2-Pt+Rh-Al(4)-E configurations exhibited quite distinguishable changes, especially the NO_2-Pt+Rh-Al(4)-E(1)-(1) and NO_2+Pt+Rh-Al(4)-E(1)-(2) configurations (Fig. 4.119 and Fig. 4.120). They showed an unique change and it did not be observed in any NO_2 adsorption on the diatomic clusters. The bond between Pt and Rh atom disappeared after relaxation in both configurations eventhough the NO_2 molecule kept its bridging geometry on the surface. The absence of the Pt-Rh bonds caused very weak adsorption of the NO_2 molecule on the surface since the adsorption energies were found to be -1.66 eV and -1.83 eV for the NO_2-Pt+Rh-Al(4)-E(1)-(1) and NO_2-Pt+Rh-Al(4)-E(1)-(2) configurations respectively and they were the lowest adsorption energies among all the NO_2-Pt+Rh/γ-Al_2O_3(100) configurations. For the last important observation about the adsorption energy of the NO_2 molecule was related to the NO_2-Pt+Rh-Al(4)-E(2)-(2) and NO_2+Pt+Rh-Al(4)-E(2)-(3) configurations. It was seen that relaxation caused a dislocation of the embedded Rh atoms. After relaxation, the embedded Rh atom moved out of the surface and became in the bridging geometry on the surface (Fig. 4.122 and Fig. 4.123). The adsorption energies were -3.01 eV and -3.03 eV for the NO_2-Pt+Rh-Al(4)-E(2)-(2) and NO_2-Pt+Rh-Al(4)-E(2)-(3) configurations respectively. The highest adsorption energy of the the NO_2 molecule was -3.54 eV and it belonged to the NO_2-Pt+Rh-Al(3)-B-(2)

configuration (Fig. 4.118).

According to Table 4.23, the range of the bond distances between Pt-N atoms was between 1.92 Å and 2.00 Å and the range of the bond distances between Rh-N atoms was between 1.88Å and 1.94Å. It was seen obviously in Table 4.23 that the bond distances of the Rh and N atoms were mostly shorther than the bond distances of the Pt and N atoms similar to the NO_2-Rh+Pt/γ-Al_2O_3(100) configurations. Moreover, the range of the bond distances of the O_{NO_2} atom with the Pt atoms (1.99-2.07 Å) was wider than the he range of the bond distances of the O_{NO_2} atom with the Rh atoms (2.00-2.03 Å) as seen in Table 4.23. The range of the bond distances of the Pt-Rh atoms was between the 2.49 Å and 2.60 Å.

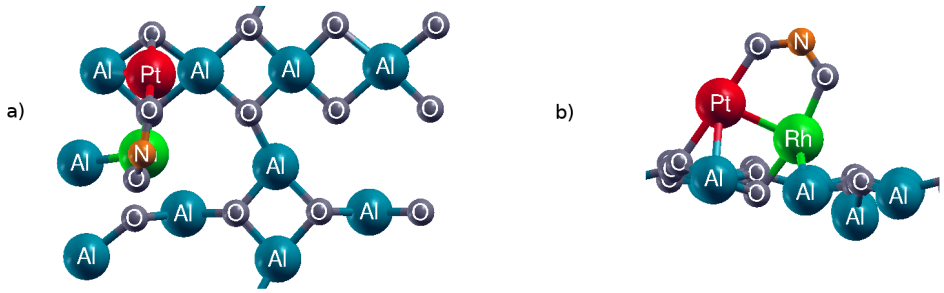

Figure 4.110: The B1 type bridging adsorption of the NO_2 molecule in the NO_2-Pt+Rh-Al(1)-B2(1)-(1) configuration, (a) top and (b) side views of the final geometry

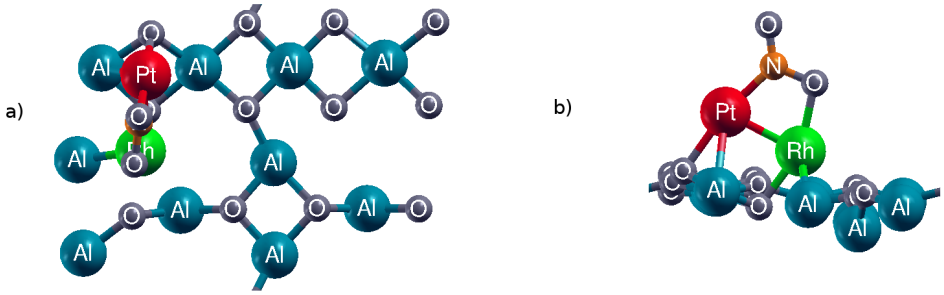

Figure 4.111: The B2 type bridging adsorption of the NO_2 molecule in the NO_2-Pt+Rh-Al(1)-B2(1)-(2) configuration, (a) top and (b) side views of the final geometry

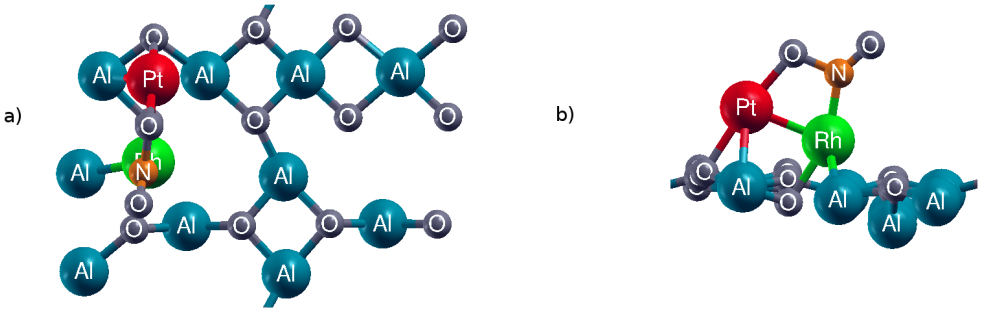

Figure 4.112: The B2 type bridging adsorption of the NO_2 molecule in the NO_2-Pt+Rh-Al(1)-B2(1)-(3) configuration, (a) top and (b) side views of the final geometry

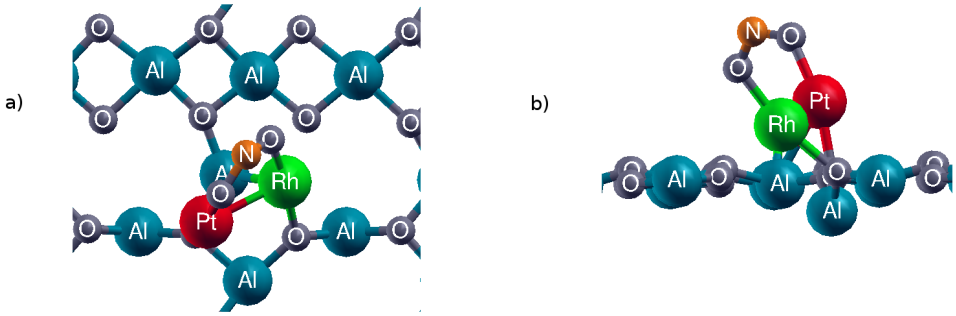

Figure 4.113: The B1 type bridging adsorption of the NO_2 molecule in the NO_2-Pt+Rh-Al(1)-B2(2)-(1) configuration, (a) top and (b) side views of the final geometry

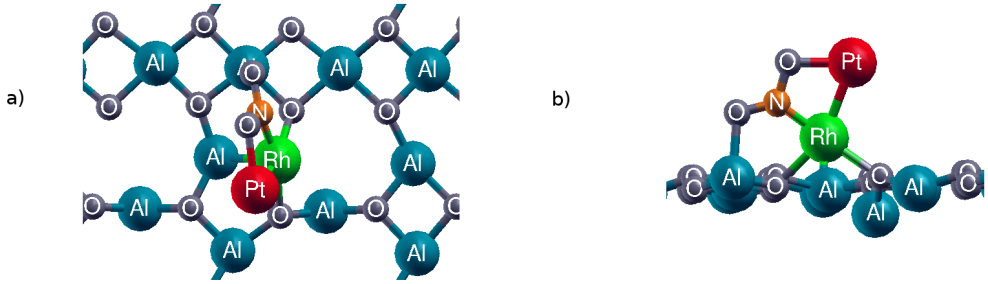

Figure 4.114: The B2 type bridging adsorption of the NO_2 molecule in the NO_2-Pt+Rh-Al(1)-B2(2)-(2) configuration, (a) top and (b) side views of the final geometry

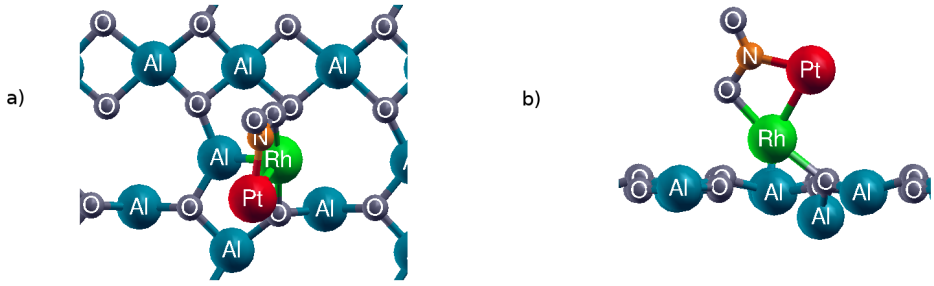

Figure 4.115: The B2 type bridging adsorption of the NO_2 molecule in the NO_2-Pt+Rh-Al(1)-B2(2)-(3) configuration, (a) top and (b) side views of the final geometry

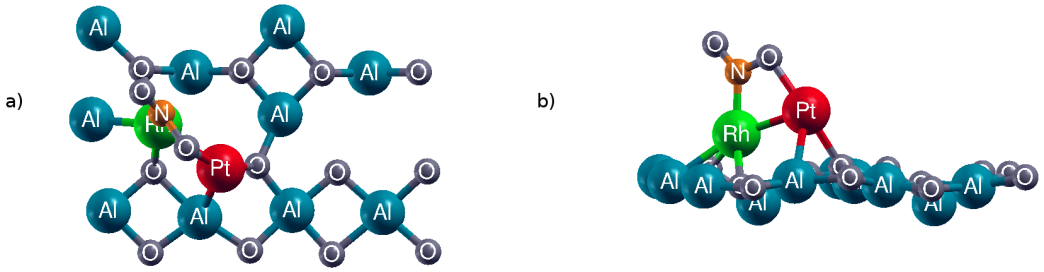

Figure 4.116: The B2 type bridging adsorption of the NO_2 molecule in the NO_2-Pt+Rh-Al(2)-E configuration, (a) top and (b) side views of the final geometry

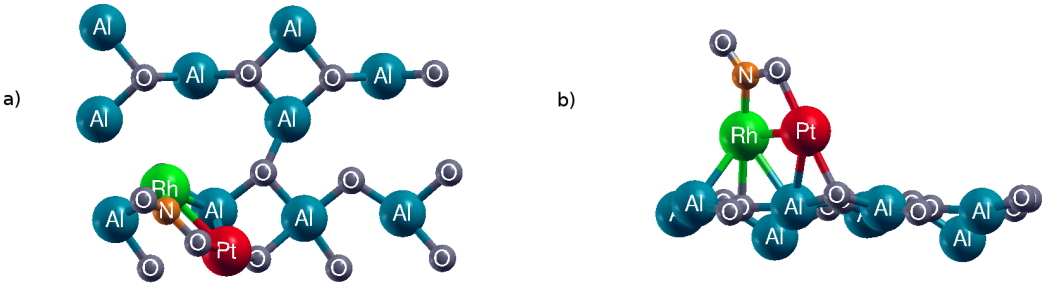

Figure 4.117: The B2 type bridging adsorption of the NO_2 molecule in the NO_2-Pt+Rh-Al(3)-B-(1) configuration, (a) top and (b) side views of the final geometry

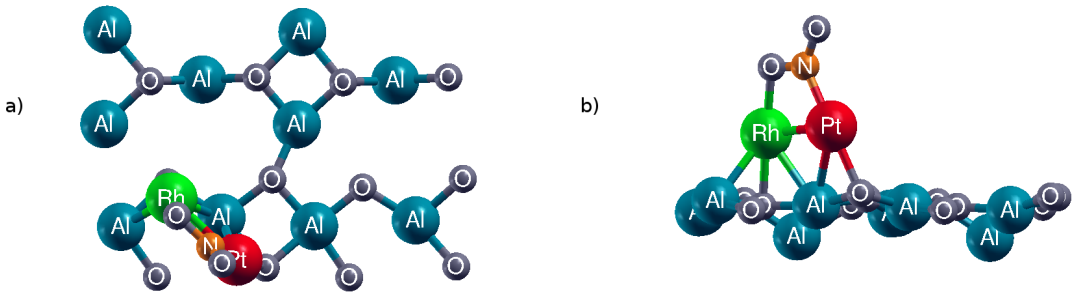

Figure 4.118: The B2 type bridging adsorption of the NO_2 molecule in the NO_2-Pt+Rh-Al(3)-B-(2) configuration, (a) top and (b) side views of the final geometry

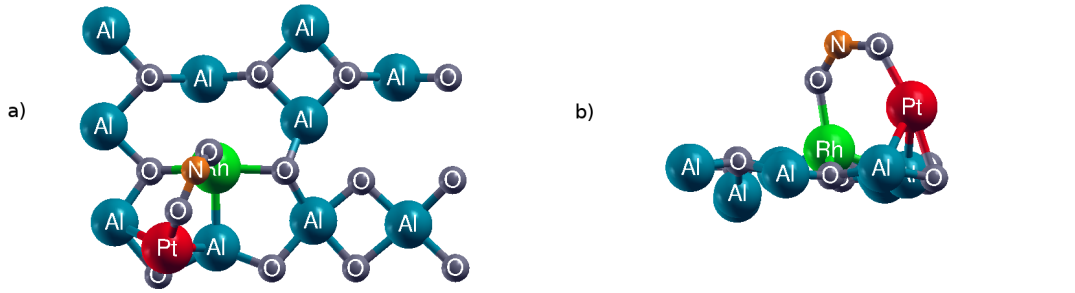

Figure 4.119: The B1 type bridging adsorption of the NO_2 molecule in the NO_2-Pt+Rh-Al(4)-E(1)-(1) configuration, (a) top and (b) side views of the final geometry

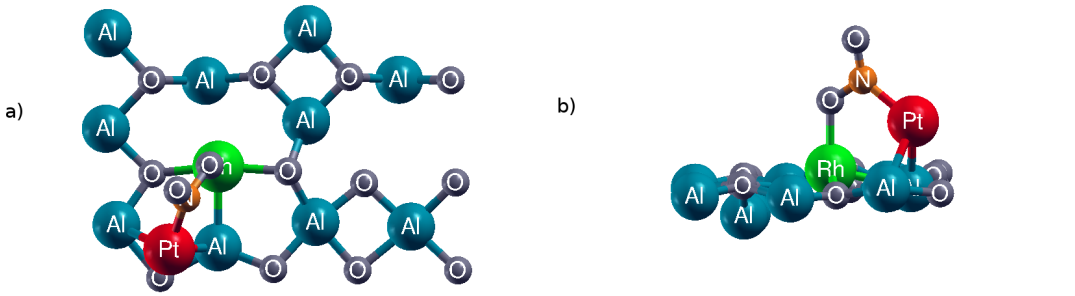

Figure 4.120: The B2 type bridging adsorption of the NO_2 molecule in the NO_2-Pt+Rh-Al(4)-E(1)-(2) configuration, (a) top and (b) side views of the final geometry

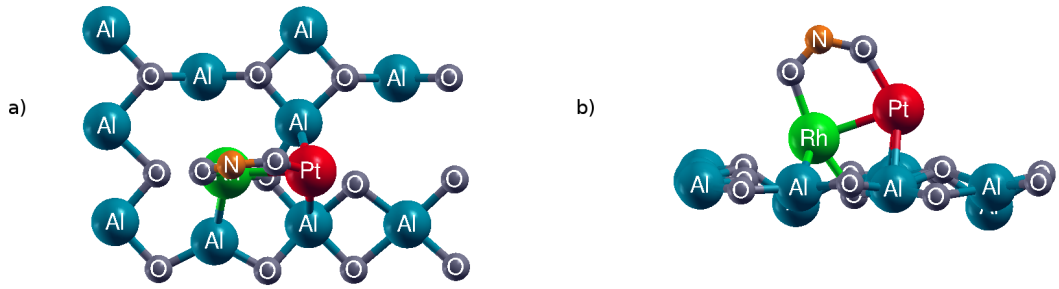

Figure 4.121: The B1 type bridging adsorption of the NO_2 molecule in the NO_2-Pt+Rh-Al(4)-E(2)-(1) configuration, (a) top and (b) side views of the final geometry

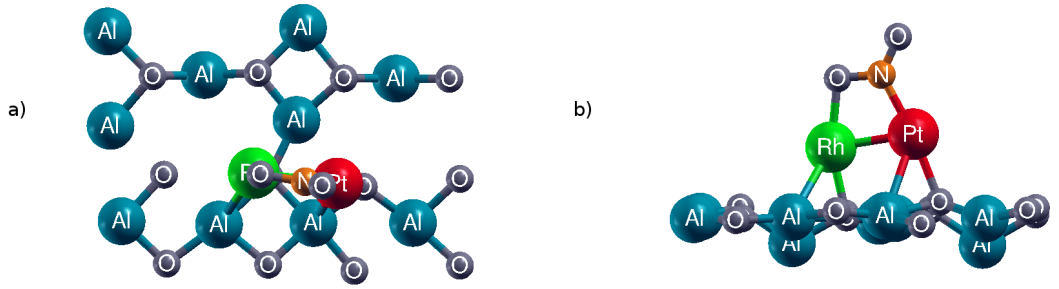

Figure 4.122: The B2 type bridging adsorption of the NO_2 molecule in the NO_2-Pt+Rh-Al(4)-E(2)-(2) configuration, (a) top and (b) side views of the final geometry

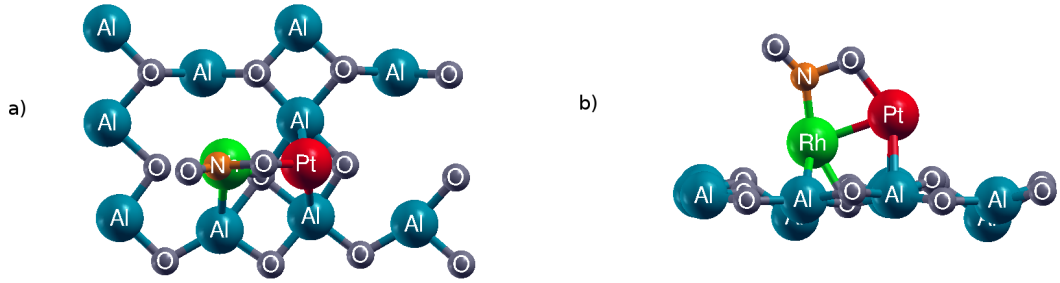

Figure 4.123: The B2 type bridging adsorption of the NO_2 molecule in the NO_2-Pt+Rh-Al(4)-E(2)-(3) configuration, (a) top and (b) side views of the final geometry

Finally, there were two common observation for the NO_2 adsorption on the Rh+Pt/γ-Al_2O_3(100) and Pt+Rh/γ-Al_2O_3(100) configurations. The first one was that the bond distance between the N atom and O_{NO_2} atom which was also bonded to Rh or Pt atom was larger than the distance of the N-O_{NO_2} for B2 type bridging geometries. Moreover, it was clearly seen that the bond distances between the N atom and the O_{NO_2} atom, which was also bonded to the Pt atom were larger than the bond distances of the N atom and O_{NO_2} atom which also bonded to the Rh atom.

Table 4.22: The final geometries and the adsorption energies of the relaxed NO_2+Pt-Rh/γ-Al_2O_3(100) configurations

Configuration	Description	Angle of NO_2	E_{ads}
NO_2-Pt+Rh-Al(1)-B1(1)-(1)	Bridged to Pt and Rh	119^o	-3.09
NO_2-Pt+Rh-Al(1)-B1(1)-(2)	Bridged to Pt and Rh	119^o	-3.49
NO_2-Pt+Rh-Al(1)-B1(1)-(3)	Bridged to Pt and Rh	115^o	-3.12
NO_2-Pt+Rh-Al(1)-B1(2)-(1)	Bridged to Pt and Rh	118^o	-2.78
NO_2-Pt+Rh-Al(1)-B1(2)-(2)	Bridged to Pt and Rh	115^o	-2.89
NO_2-Pt+Rh-Al(1)-B1(2)-(3)	Bridged to Pt and Rh	122^o	-3.10
NO_2-Pt+Rh-Al(2)-E	Bridged to Pt and Rh	116^o	-2.91
NO_2-Pt+Rh-Al(3)-B-(1)	Bridged to Pt and Rh	119^o	-3.61
NO_2-Pt+Rh-Al(3)-B-(2)	Bridged to Pt and Rh	120^o	-3.54
NO_2-Pt+Rh-Al(4)-E(1)-(1)	Monodentate on Rh	121^o	-1.66
NO_2-Pt+Rh-Al(4)-E(1)-(2)	Bridged to Pt and Rh	117^o	-1.83
NO_2-Pt+Rh-Al(4)-E(2)-(1)	Bridged to Pt and Rh	119^o	-2.78
NO_2-Pt+Rh-Al(4)-E(2)-(2)	Bridged to Pt and Rh	120^o	-3.01
NO_2-Pt+Rh-Al(4)-E(2)-(3)	Bridged to Pt and Rh	115^o	-3.03

Table 4.23: The bond distances (Å) of the relaxed NO_2+Pt-Rh/γ-Al_2O_3(100) configurations

Configuration	N-Pt	N-Rh	N-O_{NO_2}
NO_2-Pt+Rh-Al(1)-B1(1)-(1)	-	-	1.27 and 1.31
NO_2-Pt+Rh-Al(1)-B1(1)-(2)	1.94	-	1.22 and 1.32
NO_2-Pt+Rh-Al(1)-B1(1)-(3)	-	1.93	1.21 and 1.42
NO_2-Pt+Rh-Al(1)-B1(2)-(1)	-	-	1.28 and 1.32
NO_2-Pt+Rh-Al(1)-B1(2)-(2)*	-	1.88	1.28 and 1.34
NO_2-Pt+Rh-Al(1)-B1(2)-(3)	1.92	-	1.22 and 1.31
NO_2-Pt+Rh-Al(2)-E	-	1.94	1.21 and 1.42
NO_2-Pt+Rh-Al(3)-B-(1)	-	1.90	1.22 and 1.35
NO_2-Pt+Rh-Al(3)-B-(2)	1.94	-	1.22 and 1.33
NO_2-Pt+Rh-Al(4)-E(1)-(1)*	-	-	1.26 and 1.29
NO_2-Pt+Rh-Al(4)-E(1)-(2)*	1.96	-	1.22 and 1.34
NO_2-Pt+Rh-Al(4)-E(2)-(1)	-	-	1.27 and 1.32
NO_2-Pt+Rh-Al(4)-E(2)-(2)	1.97	-	1.22 and 1.33
NO_2-Pt+Rh-Al(4)-E(2)-(3)	-	1.94	1.21 and 1.43
Configuration	Pt-O_{NO_2}	Rh-O_{NO_2}	Rh-Pt
NO_2-Pt+Rh-Al(1)-B1(1)-(1)	Pt-O_{NO_2} 2.03	Rh-O_{NO_2} 2.03	2.56
NO_2-Pt+Rh-Al(1)-B1(1)-(2)	-	Rh-O_{NO_2} 1.99	2.51
NO_2-Pt+Rh-Al(1)-B1(1)-(3)	Pt-O_{NO_2} 2.02	-	2.50
NO_2-Pt+Rh-Al(1)-B1(2)-(1)	Pt-O_{NO_2} 2.00	Rh-O_{NO_2} 2.03	2.53
NO_2-Pt+Rh-Al(1)-B1(2)-(2)*	-	Rh-O_{NO_2} 2.04	2.55
NO_2-Pt+Rh-Al(1)-B1(2)-(3)	-	Rh-O_{NO_2} 2.04	2.55
NO_2-Pt+Rh-Al(2)-E	Pt-O_{NO_2} 2.03	-	2.49
NO_2-Pt+Rh-Al(3)-B-(1)	Pt-O_{NO_2} 2.00	-	2.60
NO_2-Pt+Rh-Al(3)-B-(2)	-	Rh-O_{NO_2} 1.99	2.60
NO_2-Pt+Rh-Al(4)-E(1)-(1)*	Pt-O_{NO_2} 2.01	Rh-O_{NO_2} 2.06	-
NO_2-Pt+Rh-Al(4)-E(1)-(2)*	-	Rh-O_{NO_2} 2.02	-
NO_2-Pt+Rh-Al(4)-E(2)-(1)	Pt-O_{NO_2} 2.02	Rh-O_{NO_2} 2.04	2.60
NO_2-Pt+Rh-Al(4)-E(2)-(2)	-	Rh-O_{NO_2} 2.03	2.50
NO_2-Pt+Rh-Al(4)-E(2)-(3)	Pt-O_{NO_2} 2.01	-	2.49

CHAPTER 5

CONCLUSION

Although transportation and industrial engines are indispensable necessities for our life, their harmfull effects to the environment can not be disregarded. Harmfull gases produced by combustion engines such as NO_x, should be reduced to protect environment. Because of this reason, governments have regulated laws to decrase the level of emissions of harmfull gases and researchers have studied on developing the catalysts which provide optimum level emission of CO, CO_2,NO_x and unburned or partially burned hydrocarbons. The NSR catalyst is one the most promising candidates to reduce the NO_x emission produced by combustion engines. For the NSR catalysts, the investigation of the noble metal and supported material have been carried on over twenty years both theoretically and experimentally. Rhodium, Platinium and γ-Al_2O_3 are the most capable components for the NSR catalysts to reduce NO_x emission. In this thesis, we investigated the effects of the noble metals as a single metal and diatomic clusters for adsorption of the NO_2 molecule on the γ-Al_2O_3 using DFT.

The γ-Al_2O_3 was chosen as a support material and Pt and Rh were adsorbed as a single atom and small clusters on the γ-Al_2O_3(100) surface. We studied on the γ-Al_2O_3(100) surface since this surface had the large number of penta-coordinated Al atoms (Al_{penta}) known as an active sides for the adsorption of Pt atom. The 4-layer and 8-layer slab models of the γ-Al_2O_3(100) surface were constructed and their surface energies were calculated. Their surface energies were close to each other and they agreed the surface energies reported before in the literature. For all calculations 4-layer structure extended to 2x1x1 cell was used and all configurations were relaxed fully.

The adsorption of the Pt and Rh atoms on the γ-Al_2O_3(100) surface was investigated as both a single atom and diatomic clusters. A single atom calculations were performed based on the surface Al_{penta} atoms and the bond distances and the adsorption energies of the noble metals were calculated. The adsorption behaviours of Pt and Rh atoms and the interaction between the noble metals and the surface were explained. Our results agreeded with the results in the literature. In addition, it was observed that the Pt atoms were adsorbed by the surface more strongly than the Rh atoms except only around of the Al(3) atom. For the adsorptions of the diatomic clusters, we studied on 2Pt, 2Rh and Pt+Rh small clusters. The second atoms (Pt or Rh) were added to the configurations obtained from the single metal adsorptions on the surface. The adsorption behaviours of the second atoms and their interaction with the surface and the previously adsorbed noble metal atoms were examined. The bond distance analysis were also done and differences between the diatomic geometries were explained. The stability of the adsorptions was discussed. It was seen that the interaction between Rh-Rh atoms was dominant than Pt-Pt and Pt-Rh interactions on the surface.

The adsorption of the NO_2 molecule on the γ-Al_2O_3(100) surface was studied in details. All configurations obtained from the Pt and Rh atom adsorptions on the surface were used for the adsorption of the NO_2 molecule. The NO_2 molecule was replaced on the surface both in bridging and monodentate configurations. We used only one bridging configuration for the system in which a single noble metal was adsorbed and two different bridging configuration for the systems in which diatomic clusters were adsorbed. It was observed that monodentate configurations of the NO_2 molecule exhibited a tendency to construct bridging geometries on the surface in the configurations in which a single noble metal was adsorbed. In addition, bridging type adsorptions usually gave higher adsorption energies than monodentate configurations. For the adsorption of the NO_2 molecule on the diatomic small clusters, the results of the configurations that exhibited remarkable changes in their geometries were discussed in details. The adsorption energies of the NO_2 molecule were calculated and it was found that the second type bridging (B2 type) configurations were more stable than other type bridging (B1 type) and monodentate configurations. In other words, the bond between the noble metals and the N atom was stronger than the bond between the O_{NO_2} atom and the noble metals. The bond distance analysis also proved that the bonds between the Rh-O_{NO_2} atoms were stronger than Pt-O_{NO_2} atoms.

REFERENCES

[1] Z. Hu, K. Sun, W. Li, B. Xu, Catal. Today, 158 , 432, (2010)

[2] J. Xu, M. P. Harold, V. Balakotaiah, Appl. Catal. B: Environmental, 305, (2011)

[3] Y. Liu, M. Meng, X. Li, L. Guo, Y. Zha, Chem. Eng. Research Hand Design, 86, 932 (2008)

[4] J. H. Kwak, D. H. Kim, T. Szailer, C. H. F. Peden, and J. Szanyi, Catal. Lett., 111, 3 (2006)

[5] W. S. Epling, J. E. Parks, G. C. Campbell, A. Yezerets, N. W. Currier, L. E. Campbell, Catal. Today, 96, 21 (2004)

[6] P. Kočí, F. Plát, J. Štěpánek, Š. Bártová M. Marek, M. Kubíček, V. Schmeißer, D.l Chatterjee, M. Weibel, Catal. Today, 147S, 257 (2009)

[7] A. Lindholm, H. Sjövall, L. Olsson, Appl. Catal B: Environmental, 98, 112 (2010)

[8] W. Turek, A. Plis, P. Da Costa, A. Krzton, Appl. Surf. Sci., 256, 5572 (2010)

[9] M. Born, R. Oppenheimer, Ann. Phys., 84, 457 (1927).

[10] K. Burke, ABC of DFT, Avaible at http://dft.uci.edu/materials/bookABCDFT/gamma/g1.pdf, (2007).

[11] J. Kohanoff, Electronic Structure Calculations for Solids and Molecules: Theory and Computational Methods, Cambridge University Press, (2006).

[12] W. Kohn, L. J. Sham, Phys. Rev., 140, A1133 (1965).

[13] P. Hohenberg and W. Kohn; âInhomogeneous electron gasâ, Phys. Rev. 136, B864, (1964)

[14] R. M. Martin, Electronic Structure Basic Theory and Practical Methods, Cambridge University Press, (2004).

[15] J. P. Perdew, K. Burke, M. Ernzerhof, Phys. Rev. Lett., 77 (1996).

[16] C. Kittel, Introduction to the Solid State Physics, Jhon Wiley Press, (2005).

[17] A.J. McMichael, D.H. Campbell-Lendrum, C.F. Corvalan, K.L. Ebi, A. Githeko, J.D. Scheraga, Climate Change and Human Health: Risks and Responses, p. 1-17, Geneva, Switzerland: World Health Organization (2003).

[18] J. Yu, J. Cheng, C. Yan Ma, H. Lin Wang, L. D. Li , Z. P. Hao , Z. P. Xu, Journal of Colloid and Interface Science, 333, 423 (2009)

[19] J. P.Breen, R. Burch, C. Fontaine-Gautrelet, C. Hardacre, C. Rioche, Appl. Catal B: Environmental, 81, 150 (2008)

[20] I. Atribak, A. Bueno-López, A. Garc´ıa-Garc´ıa, J. Catal., 259, 123 (2008)

[21] N. Takahashi, A. Suda, I. Hachisuka, M. Sugiura, H. Sobukawa, H. Shinjoh, Appl. Catal B: Environmental, 72, 123 (2007)

[22] L. Olsson and E. Fridell , J. Catal. 210, 340 (2002)

[23] N. A. Deskins , D. Mei, M. Dupuis, Surf. Sci., 603, 2793 (2009)

[24] J. Jelic, R.l J. Meyer ,Catal. Today, 136, 76 (2008)

[25] M. C. Valero, P. Raybaud, and P. Saute, Phys. Rev. B, 75, 045427 (Í2007Í)

[26] H. Imagawa , N. Takahashi, T. Tanaka, S. Matsunaga, H. Shinjoh, Appl. Catal B: Environmental, 92, 23 (2009)

[27] N. W. Cant , I. O.Y. Liu, M. J. Patterson, J. Catal., 243, 309 (2006)

[28] Y. Su, M.D. Amiridis / Catal. Today, 96, 31 (2004)

[29] C. Verrier, J. H. Kwak, D. H. Kim, C. H. F. Peden, J. Szanyi, Catal. Today, 136, 121 (2008)

[30] N. Macleod, R. M. Lambert, Catal. Comm., 3, 61 (2002)

[31] Y. W. Lee, E. Gulari, Catal. Comm. 5, 499 (2004)

[32] M. C. Valero, P. Raybaud, P. Sautet, J. Phys. Chem. B, 110, 1759 (2006)

[33] J., J. Hu, D. Mei, C. W. Yi, D. H. Kim, C. H. F. Peden, L. F. Allard, J. Szanyi1, Science ,325 (2009)

[34] M. Digne, P. Sautet, P. Raybaud, P. Euzen, H. Toulhoat, J. Catal., 226, 54 (2004)

[35] H.P. Pinto, R.M. Nieminen, S.D. Elliott, Phys. Rev. B, 70 (2004)

[36] S. Suarez, C. Saiz, M. Yates, J.A. Martin, P. Avila, J. Blanco, Appl. Catal. B: Environmental, 55, 57 (2005)

[37] S. Suarez, M. Yates, A.L. Petre, J.A. Martın, P. Avila, J. Blanco, Appl. Catal. B: Environmental, 64, 302 (2006)

[38] J. Haber, M. Nattich, T. Machej, Appl. Catal. B: Environmental, 77, 278 (2008)

[39] C. D. Zeinalipour-Yazdi, A. L. Cooksy, and A. M. Efstathiou, J. Phys.,36, 145 (2002)

[40] S. Salasc, M. Skoglundh, E. Fridell, Applied Catalysis B: Environmental 36, 145 (2002)

[41] Y. Su, K. S. Kabin, M. P. Harold, M. D. Amiridis, Appl. Catal. B: Environmental, 71, 207 (2007)

[42] P. S. Dimick, J. L. Kross, E. G. Roberts, R. G. Herman, H. G. Stenger, C. E. Lyman , Appl. Catal. B: Environmental, 89, 1 (2009)

[43] Z. Hu, F. M. Allen, C. Z. Wan, R. M. Heck, J. J. Steger, R. E. Lakis and C. E. Lyman, J. Catal., 174, 13 (1998)

[44] K. Yuge, T. Ichikawa and J. Kawai, Materials Transactions, 51, 321 (2010)

[45] K. Yuge, J. Phys.: Condens. Matter, 22, 6 (2010)

[46] Y. Han, C. Liu, Q. Ge, J. Phys. Chem. B, 110, 7463 (2006)

[47] L. Li, Q. Shen, J. Cheng, Z. Hao, Catal. Today, 158, 361 (2010)

[48] C. Lee, E. Cho, H. Lee, K. S. Seol and S. Han, Phys. Rev. B, 76, 245110 (Í2007Í).

[49] W.Y.Ching, L. Ouyang, P. Rulis, H. Yao, Phys. Rev.B, 78, 014106 (2008).

[50] C. Wolverton, K. C. Hass, Phys. Rev.B, 63, 024102 (2000).

[51] G. Paglia, C. E. Buckley,A. L. Rohl,B. A. Hunter,R. D. Hart,1 J. V. Hanna,and L. T. Byrne, Phys. Rev. B, 68, 144110 (Í2003Í)

[52] G. Gutierrez, A. Taga,and B. Johansson, Phys. Rev. B, 65, 012101 (2001)

[53] X. Krokidis, P. Raybaud, A. E. Gobichon, B.e Rebours, P. Euzen,and H. Toulhoat, J. Phys. Chem. B,105, 5121 (2001)

[54] M. Sun, A. E. Nelson and J. Adjaye, J. Phys. Chem. B, 110, 2310 (2006)

[55] G. Paglia, A. L. Rohl, C. E. Buckley, and J. D. Gale, Phys. Rev. B, 71, 224115Í (2005Í)

[56] Avaible at http://www.quantum-espresso.org/, with General Public Licence (2010).

[57] D. Mei, Q. Ge, J. H. Kwak, D. H. Kim, C. Verrier, J. Szanyia and C. H. F. Pedena, J. Phys. Chem. Chem. Phys., 11, 3380 (2009)